CHALMERS
UNIVERSITY OF TECHNOLOGY

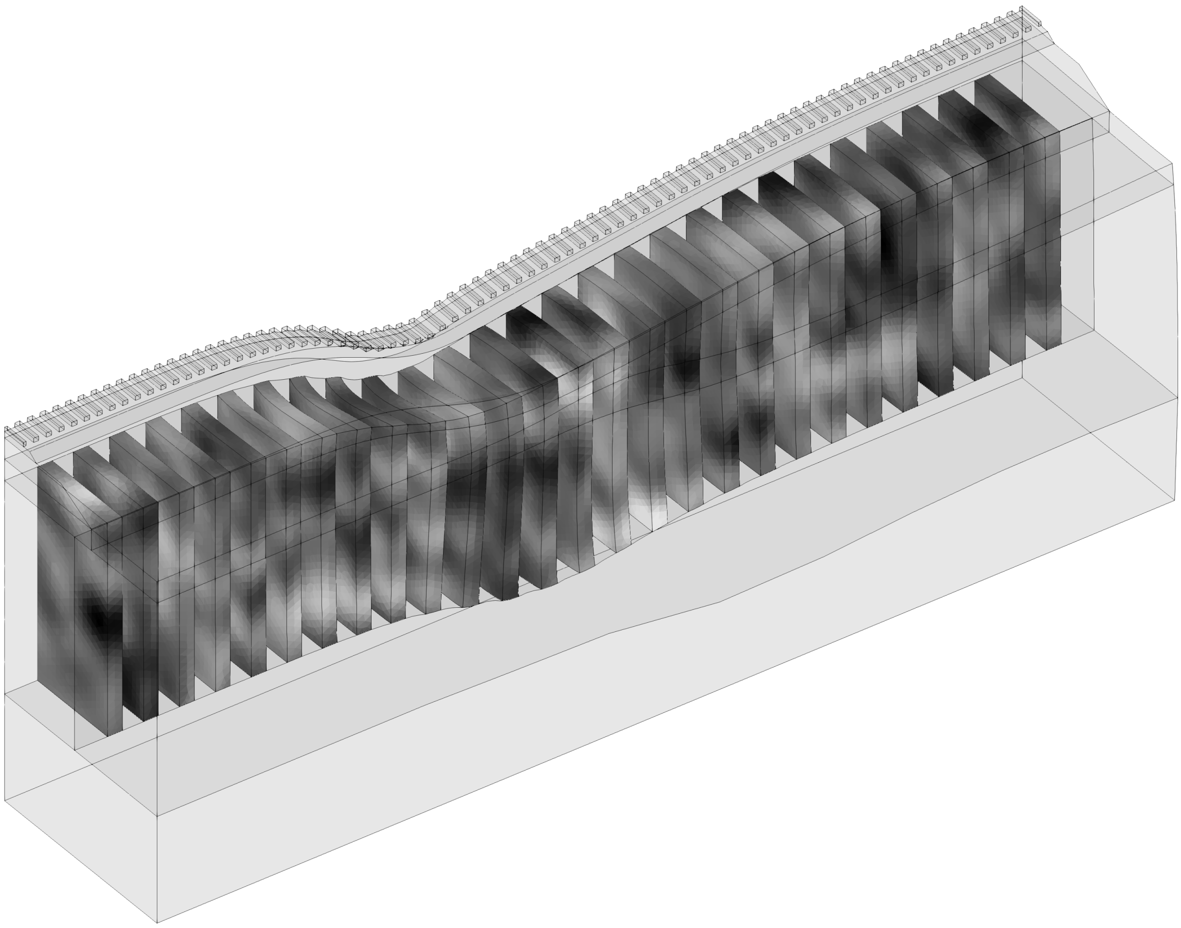

Impact of heterogeneity in stabilised clay on the settlement of ballasted track

Master's thesis in Master Programme Infrastructure and Environmental Engineering

Albin Alenius

Alfred Nilsson

DEPARTMENT OF ARCHITECTURE AND CIVIL ENGINEERING

CHALMERS UNIVERSITY OF TECHNOLOGY
Gothenburg, Sweden 2026
www.chalmers.se

Master's thesis 2026

Impact of heterogeneity in stabilised clay on the settlement of ballasted track

Albin Alenius

Alfred Nilsson

Department of Architecture and Civil Engineering
Chalmers University of Technology
Gothenburg, Sweden 2026

Impact of heterogeneity in stabilised clay on the settlement of ballasted track
Albin Alenius and Alfred Nilsson

Examiner: Jelke Dijkstra, Division of Geology and Geotechnics
Supervisor: Kourosh Nasrollahi, Division of Structural Engineering

Master's Thesis 2026
Department of Architecture and Civil Engineering
Division of Geology and Geotechnics
Chalmers University of Technology
SE-412 96 Gothenburg
Telephone +46 31 772 1000

Cover: Instantaneous track response during a bogie passage, considering the spatial variability in lime-cement column stiffness within homogenised walls.

Typeset in LaTeX
Printed by Chalmers Reproservice
Gothenburg, Sweden 2026

Impact of heterogeneity in stabilised clay on the settlement of ballasted track
Albin Alenius
Alfred Nilsson

Department of Architecture and Civil Engineering
Chalmers University of Technology

Abstract

Accurately predicting accumulated track settlement and the resulting deterioration of vertical track geometry is a major challenge in railway infrastructure maintenance. This issue is particularly critical for railways constructed on soft clay soils, where repeated train loading can lead to excessive and differential settlements, increased maintenance demand, reduced ride comfort, and decreased operational reliability. An additional complexity arises from the spatial variability of soil conditions and ground improvement measures, which can strongly influence track response and long-term performance. This thesis investigates the dynamic vehicle–track–soil interaction and long-term settlement behaviour of ballasted railway tracks founded on soft clay, with particular focus on the influence of spatial variability in lime-cement column (LCC) improved ground. A numerical modelling framework is employed by coupling dynamic finite-element simulations with empirical settlement models for ballast and subgrade layers. Spatial variability in LCC properties is incorporated through random field modelling. Different LCC reinforcement configurations are evaluated to investigate their influence on track stiffness, stress distribution, and accumulated settlements. In addition, sensitivity analyses are performed to identify the most influential parameters governing settlement development and track response. The results indicate that spatial variability significantly affects the distribution of track stiffness and the development of differential settlements, while LCC reinforcement effectively reduces long-term settlements and improves overall track performance. The developed framework also enables systematic evaluation of mitigation strategies for railway infrastructure subjected to spatially varying soft ground conditions over time. The findings contribute to a better understanding of railway behaviour on soft soils and provide a basis for more reliable prediction of long-term track performance and maintenance planning.

Keywords: vehicle–track–soil interaction, soft clay, long-term settlement, spatial variability, lime-cement columns, finite-element modelling, random fields

Acknowledgements

We would like to express gratitude to our examiner, Professor Jelke Dijkstra, for his valuable input, critiques and unmatched brainstorming. He should also be thanked for introducing us to Post-doctoral researcher Kourosh Nasrollahi, our supervisor and now friend. Without whom, this thesis would not be possible. His continued guidance, expertise and unwavering support was instrumental in the development and completion of this work. Any future students would consider themselves lucky having him as a supervisor.

Albin Alenius & Alfred Nilsson, Gothenburg, June 2026

Contents

List of Figures

List of Tables

1 Introduction

This chapter discusses the background and motivation behind the study. It explains the significance of the work and outlines the approach and methods used to carry out the research.

1.1 Background

The demand for railway transportation has increased significantly due to its high transport efficiency, lower environmental impact, and ability to support high operating speeds compared to other modes. This development is driven by factors such as population growth, increasing environmental awareness, and global climate policies that promote sustainable transport systems. In Sweden, the railway system represents an important mode of transport for both passengers and freight of goods, resulting in an increase in railway traffic load of approximately 30% between 2000 and 2024 (Trafikanalys, 2024). The growing recognition of rail transport as a sustainable transportation alternative has consequently led to higher axle loads and increased traffic intensity, thereby increasing the need for improved network capacity and more reliable infrastructure capable of maintaining long-term performance.

In areas where the railway infrastructure is constructed on soft soils, such as the soft clay deposits commonly found in the Gothenburg region, these increased loading demands may contribute to excessive and differential settlements. Such settlements can lead to deterioration of track geometry, increased maintenance demand, reduced ride comfort, poor punctuality and in severe cases, compromised operational safety. Consequently, improving the long-term deformation resistance and performance of railway infrastructure has become increasingly important for ensuring reliable operation, reduced maintenance requirements, and sustainable railway systems.

Railway tracks are continuously subjected to cyclic dynamic loading due to repeated vehicle passages. These loads are transferred from the wheel to the rail and further through the components of the track to the soil. Over time, repeated loading may contribute to permanent settlements. In soft ground conditions, especially soft clays, which generally exhibit relatively low stiffness and strength, these repeated dynamic loads can lead to uneven track support and excessive deformations. In addition to the load magnitudes, the long-term response also depends on mechanical behaviour, and natural spatial variability of the supporting soil layers with depth and along the track. Various mitigating measures can be applied to improve the dynamic response of railways on soft soil, for example, lime-cement columns (LCCs) are a commonly used measure to improve the stiffness and strength of the soil, thus reducing deformations and improving stability, and long-term performance. However, LCCs can exhibit spatial variability due to the quality of the mixing and the natural variations of the mixed soil, which may affect the track performance and lead to differential settlements. These uncertainties pose a major challenge and remain insufficiently understood, limiting the development of reliable prediction models and resilient design of railway infrastructure.

Within the Postdoctoral project at the Department of Architecture and Civil Engineering, Divisions of Structural Engineering and Geotechnical Engineering, at Chalmers University of Technology in Gothenburg, Sweden, the overall aim is to investigate the influence of different superstructure and substructure layers (components) and their interaction on the long-term performance of railway tracks at the system level. Therefore, the present study focuses specifically on the influence of spatial variations in soft soil stabilised by lime-cement, and on the design of LCCs as a ground improvement method to mitigate the effects of soft soil layers and reduce long-term railway settlements due to dynamic railway loading.

1.2 Aim and objectives

The objective of this study is to develop a railway track model on soft soil, with particular emphasis on soft clay, by incorporating the vehicle, track, and layered soil system while accounting for uncertainties in soil properties at different spatial scales. Lime-cement column (LCC) designs are included to mitigate long-term track settlements. In addition, a computational framework is developed to couple the STEM software, which contains an extensive substructure for simulating dynamic vehicle–track interaction and ground-borne vibrations, with the existing two-dimensional Chalmers in-house developed software DIFF for the simulation of long-term differential settlements by incorporating variations in the static stiffness of the substructure calculated from the STEM model along the track. The study further investigates the influence of longitudinal, transverse, and depth-wise variations in LCC properties on the track response and long-term settlements. Moreover, different approaches for modelling LCCs, together with the effects of their positioning, are evaluated to assess their effectiveness in improving track performance and reducing settlements.

In collaboration between the authors of this thesis, its supervisor and examiner, this thesis is further summarised in a conference paper titled “Influence of Spatial Variability in Soft Soil and Deep-Mixed Columns on Long-Term Settlement in Railways” by A. Alenius, A. Nilsson, J. Dijkstra, and K. Nasrollahi. The paper has been accepted to the Railways 2026 Conference, to be held in Budapest, Hungary, from 23-–26 August 2026, and will be published in the conference proceedings as a 15-page contribution.

1.3 Limitations

The software used in this study is limited to MATLAB and Python. Model parameters, material properties, geometrical configurations, and levels of spatial variability are collected from previous studies Aggestam and Nielsen (2019), Bozkurt et al.

(2025), Nasrollahi (2025) and Wong et al. (2024) as well as from literature related to the selected case study in Sweden. The geometry and stratigraphy of the model is theoretical, limiting the ability to validate the results against measured data. The soil layers are modelled as single phase linear elastic materials, and the effects from groundwater flow are not considered in the analyses.

1.4 Societal, ethical and ecological impacts

Railway transport belongs to the more sustainable side of the spectrum of transport systems that have less environmental impact than other high-speed transport modalities. Sustainability not only includes environmental sustainability but societal and economical sustainability as well. This includes reliability, safety and comfort. Excessive differential settlements can generate ground-borne vibrations that propagate to nearby structures transmitting to the structures themselves causing damaging, perceivable, and audible vibrations. These differential settlements have to be remedied through maintenance or replacement, both causing major adverse economic effects and service disruption. Assessing discontinuities in support stiffness and settlements along railway tracks is therefore a significant part in railway sustainability.

1.5 Thesis layout

The report is organised into six chapters. Chapter 2 provides the theoretical background related to dynamic simulations, finite-element modelling, and the modelling of uncertainties in soil. Chapter 3 contains the modelling methodology, simulation procedures and the assumptions considered, along with a short case study conducted of the Gothenburg region. The numerical findings are presented in Chapter 4. Chapter 5 summarises the overall study and discusses the conclusions drawn from the work. Finally, Chapter 6 outlines recommendations and possible directions for future research.

2 Theory and literature review

The following chapter presents the theoretical background that forms the basis of the developed finite-element (FE) models and the conducted dynamic simulations. The chapter introduces fundamental concepts related to dynamic vehicle-track-soil interaction, soft soil behaviour, long-term settlement mechanisms, and spatial variability in soil properties. In addition, an overview of ground improvement techniques for railway infrastructure is provided, with particular focus on deep-mixing, together with a brief literature review on the development of numerical models for railway dynamics and long-term track performance on soft soils.

2.1 Track models — literature review

Modelling of railway dynamic problems has developed from simple analytical approaches towards more advanced numerical simulations which better capture the complex interaction between vehicle, track and soil systems. These numerical models with higher complexity are often solved using dedicated software or through custom-developed numerical implementations.

Beam on elastic foundation (BOEF) based on Winkler foundation theory is a common modelling approach to study the dynamic behaviour of railway tracks. In this approach the rail is represented as a beam element supported in two dimensions (2D) by springs and dashpots representing the track and soil systems. Due to the simplicity of these models, the computational cost is low, which historically has made the approach favoured for preliminary analyses and investigations of fundamental track behaviour. However, for more complex problems, such as varying geometries, layered substructure, non-linear material behaviour, and detailed component interactions, these BOEF models are often insufficient due to their limited ability to accurately represent conditions of higher complexity (Lamprea-Pineda et al., 2022).

To better capture the complexities and interactions of the railway system, numerical models such as the finite-element method (FEM) have become increasingly utilised. FEM enables a more detailed modelling of track and soil components in two or three dimensions (3D), allowing for a better representation of the geometry and material properties in the computational domain. Compared to simplified analytical models, FEM models may more accurately represent moving vehicle loads, wave propagation in the soil domain, vibration amplification and attenuation, as well as stress and strain distribution. Modern railway simulations are frequently performed using 2D or 3D FEM models to investigate problems related to ground vibrations, ballasted track, slab track, transition zones, and vehicle-track interaction. In railway engineering, the higher computational capabilities of today have allowed for the widespread use of dynamic FEM simulations, both at a larger scale and in terms of model size.

FEM models follow a continuum-based approach which is useful for modelling continuous soil layers. However, for ballast layers composed of coarse granular aggregates with particle interaction, the approach does not allow for studying of ballast degradation, particle rearrangement, and contact mechanics. Alternatively, discrete modelling techniques such as the discrete element method (DEM) can be used to study dynamic responses under cyclic loading. Coupling between DEM and FEM is therefore an option to increase the understanding of the mechanisms that govern how granular ballast layers settle (compaction, particle rearrangement, and ballast spreading) when soil layers are modelled as a continuum. Although this type of approach have been applied in studies by Nishiura et al. (2018), Ahmadi et al. (2026) and provides a more detailed particle response, these types of simulations are generally computationally costly at a larger scale.

3D FE modelling is thereby often a reasonable approach compared to a coupled DEM-FEM methodology, as it reduces the computational cost while retaining the computational stability and accuracy of the simulation. However, these models are still computationally demanding and cannot efficiently simulate a large number of load cycles or train passages. Therefore, equivalent reduced-order 2D models are introduced for simulating the vertical dynamic vehicle-track-soil interaction integrated with empirical settlement models. Dynamic railway problems simulated in FEM models are solved in the time or frequency domain, depending on the formulation of the problem. Frequently applied solution strategies are modal superposition techniques and direct time integration (Nasrollahi et al., 2023).

Linear elastic constitutive models are often adopted in finite-element modelling due to their simplicity, while being a reasonable approach for ballast and soil materials as stated in a review by Setiawan and Kim (2025). Paixão et al. (2016) conclude that linear elastic material models may provide reasonable rail displacement results when compared to non-linear models, but caution is recommended when assessing stress and strain with linear elastic constitutive models due to possible underestimation of internal stresses at the particle interface. Additionally, drained behaviour is frequently assumed in railway dynamics as a result of the short time frame of a train passage compared to pore water pressure dissipation.

Various mitigation measures have been investigated and proposed in the literature to retain the performance of railway tracks under repeated vehicle loading. Measures may be implemented at either the superstructure level, substructure level, or as a combination of both. For example, Thompson et al. (2015) investigates mitigation effects when implementing a stiffer layer in the substructure such as a slab or a reinforced soil layer. Additional measures applicable at the substructure level are deep mixing techniques, piles , and geotextiles (Ouakka et al., 2022). Aggestam and Nielsen (2019) study the effects of softer or stiffer rail pads at the superstructure level and the corresponding dynamic response. Other measures in the superstructure include wider sleeper base areas, shorter spacing between sleepers, auxiliary rail, or under sleeper pads implemented at the sleeper-ballast interface (Esveld, 2014; Nasrollahi & Nielsen, 2024; Nasrollahi, 2025; Nasrollahi et al., 2023).

Railways are built on soil and bedrock that was deposited and formed through natural geological processes, and as a result, properties such as density, strength and stiffness parameters may exhibit significant spatial variability. This may lead to uneven support conditions followed by differential long-term settlement. Traditional geotechnical design often follows a deterministic approach, where material properties are assumed to be uniform, leading to an inadequate representation of inherent uncertainties in natural geomaterials. To address this limitation, stochastic approaches can be implemented to model spatial variability (Griffiths & Fenton, 2007). A study by Zuada Coelho et al. (2023), investigates the dynamic response when spatial soil variability is considered by introducing random variables in an FE model and concluded that the results are heavily influenced by stochastic analysis and therefore of great importance to consider when investigating the dynamic response.

2.2 Typical components of a ballasted track

Ballasted railway tracks typically consist of a superstructure and a substructure. The superstructure comprises track components such as rails, rail pads, and sleepers, while the substructure consists of coarse granular ballast and sub-ballast layers and subgrade (Esveld, 2014). As the vehicle moves along the rail, the vehicle loads are transferred through the superstructure to the underlying strata, where the coarse grained layers redistribute the loads, limit dynamic loading effects, and contribute to pore water drainage. The subgrade is site-specific based on the geological history and often constitutes one of the most critical components, especially in regions with predominant soft soil deposits such as silt and clay, which may significantly affect the long-term performance of the track due to permanent differential deformations. Figure 2.1 presents a typical ballasted railway track configuration with both the superstructure and the substructure.

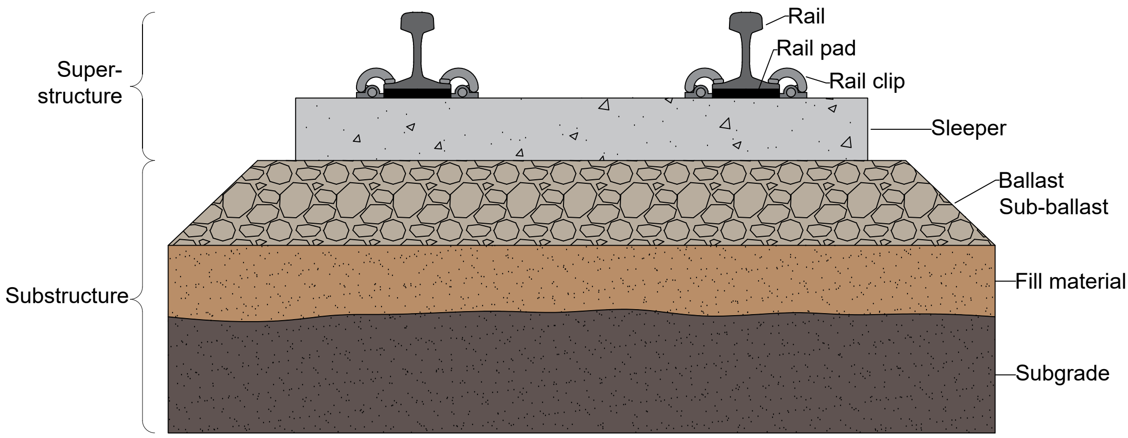

Figure 2.1: Typical components of a conventional ballasted railway track, including the superstructure (rails, rail pads, fastening systems, and sleepers) and the substructure (ballast, sub-ballast, fill material, and subgrade).

2.3 Dynamic vehicle-track-soil interaction in the time domain

The dynamic vehicle-track-soil interaction (VTSI) governs the response of the vehicle, track superstructure, and substructure, when subjected to moving vehicle loads. The interaction is dynamic as a result of the time dependence of the wheel-rail contact forces and the inertia of the components (Esveld, 2014). The loads generate vibrations that propagate as stress waves through the track and underlying soil. The dynamic response subsequently depends on the mass, stiffness, and damping characteristics of the system, governed by the FE equation of motion defined as in Equation 2.1, where $\mathbf{M}$ denotes the mass matrix, while $\mathbf{C}$, and $\mathbf{K}$ represent damping and stiffness matrices, respectively. $\mathbf{F}_{\text{ext}}(t)$ is the external force vector, $\mathbf{F}_g$ is the gravity load, while $\ddot{\mathbf{u}}(t)$, $\dot{\mathbf{u}}(t)$, and $\mathbf{u}(t)$ denote the nodal acceleration, velocity, and displacement vectors of the system (Esveld, 2014).

$$\mathbf{M}\ddot{\mathbf{u}}(t) + \mathbf{C}\dot{\mathbf{u}}(t) + \mathbf{K}\mathbf{u}(t) = \mathbf{F}_{\text{ext}}(t) + \mathbf{F}_g \tag{2.1}$$

Direct time integration methods solve the equation of motion in the time domain by incremental integration. The methods can be formulated using either implicit or explicit integration schemes depending on the application. The Newmark method is a commonly applied time integration approach in structural dynamics. By introducing the Newmark approximations into the equation of motion, the system of equations may be expressed according to Equation 2.2. $\tilde{\mathbf{K}}$ denotes the effective stiffness, $\tilde{\ddot{\mathbf{u}}}$ the effective acceleration, and $\tilde{\dot{\mathbf{u}}}$ the effective velocity. For linear systems with constant matrices, the formulation may be solved efficiently since the effective stiffness matrix only requires a single factorisation (STEM team, 2026).

$$\tilde{\mathbf{K}}\Delta\mathbf{u}_{t+\Delta t} = \mathbf{F}_{\text{ext}}(t+\Delta t) - \mathbf{M}\tilde{\ddot{\mathbf{u}}} - \mathbf{C}\tilde{\dot{\mathbf{u}}} \tag{2.2}$$

The external forces $\mathbf{F}_{\text{ext}}(t)$ generated by the moving vehicle are imposed on the track through coupling of the vehicle and the track systems. The contact forces may be obtained through the implementation of a contact formulation based on Hertzian contact stiffness theory. When solving the equation of motion in the time domain, the contact forces are provided at each time-step and are positioned according to Equation 2.3, which is governed by the initial position $\mathbf{x}_0$, the velocity $\mathbf{v}$, and the time t.

$$\mathbf{x}(t) = \mathbf{x}_0 + \mathbf{v}t \tag{2.3}$$

As these point loads move along the rail, excitation of the track occurs, and as the loads are transferred through the track components to the ballast and subgrade, a dynamic response arises.

2.3.1 Propagated waves into soil from train passes

In the track and soil subsystems, vibrations propagate as different types of stress waves generated by the dynamic excitation of the rail due to moving vehicle loads. The material properties of the track and soil characterise the propagation of waves through the continuous medium (Knappert & Craig, 2012). The compression and shear wave velocities are given by Equation 2.4, where the velocity of the compression wave V_p is calculated from the constrained modulus M' and the material density ρ, while the shear wave velocity V_S is determined from the shear modulus G and the material density ρ.

$$V_p = \sqrt{\frac{M'}{\rho}}, \qquad V_S = \sqrt{\frac{G}{\rho}} \tag{2.4}$$

The propagation of vibrations and the distribution and attenuation of energy are determined by the wave velocities. This is especially significant with respect to the interaction between adjacent sleepers and the extent of the dynamic response. Due to the influence of material properties on the wave velocities, it is important to accurately obtain these parameter values. Additionally, the damping properties of the system, i.e., the spring-damper elements at the rail-sleeper interface contribute to the attenuation of energy.

2.4 Equivalent track and subgrade stiffness

Modelling dynamic vehicle-track-soil interaction in railways using FEM and constitutive models may result in high computational cost and complexity, especially when analysing long-term responses that require multiple iterations or certain number of vehicle passages (Shan et al., 2020). Instead of full-scale finite-element simulations, a common approach is to idealise the embankment and the underlying soil layers as an equivalent spring system, as demonstrated in several studies (Nasrollahi, Ramos et al., 2024; Nasrollahi et al., 2023). This type of approach can significantly reduce the computational demand while still providing a realistic representation of the track-soil interaction. The approach is conceptually related to Beam on Elasic Foundation (BOEF) models and Winkler foundation theory, in which the track support is idealised using springs and damping elements.

The equivalent spring stiffness, k_{eq} for elastic springs in a series is classically obtained through reciprocal summation of the stiffness k of each layer i in a soil profile with N number of layers, as in Equation 2.5 (Gatti, 2014).The equation follows the assumption that the force is equal for each spring and the total displacement is the sum of the individual deformations.

$$\frac{1}{k_{eq}} = \sum_{i=1}^{N} \frac{1}{k_i} \tag{2.5}$$

For continuous linear elastic soil layers, the stiffness contribution of each layer may be related to the material and geometric properties according to Equation 2.7, where E is the elastic modulus, A is the cross-sectional area and L is the thickness of the layer. The equivalent stiffness therefore depends on the stiffness properties and the geometry of the individual substructure layers.

$$k_i = \frac{EA}{L} \tag{2.6}$$

Equivalent support stiffness may also be determined numerically from finite-element analyses through the ratio between the applied load and the resulting displacement. Assuming linear elasticity, the equivalent stiffness may be expressed according to Hooke's law, by dividing the applied vertical load F with the vertical displacement u it produces (see Equation 2.7). The formulation is consistent with Winkler foundation theory, where static support stiffness is represented by linear elastic springs.

$$k_{eq} = \frac{F}{u} \tag{2.7}$$

The equivalent stiffness may vary spatially due to changes in soil stratigraphy, embankment geometry, or through ground improvements such as with lime-cement columns, and variations in support may subsequently contribute to differential settlements.

2.5 Track receptance under harmonic loading

The dynamic behaviour of railway tracks may be characterised in the frequency domain through the concept of receptance. The receptance is defined as the displacement-to-force ratio when subjected to a harmonic excitation. The formulation is commonly used to evaluate the dynamic stiffness and vibration characteristics of railway infrastructure. The receptance formulation can be expressed according to Equation 2.8.

$$H(\omega) = \frac{u}{F(\omega)} \tag{2.8}$$

u denotes the displacement response at a specific degree of freedom (DOF) in the track model, while $F(\omega)$ is the applied harmonic load, and ω the excitation frequency. For a linear dynamic system, the displacement response in the frequency domain can be obtained from the equation of motion, as seen in Equation 2.9 (Gatti, 2014).

$$\mathbf{u}(\omega) = \frac{\mathbf{F}(\omega)}{\mathbf{K} + i\omega\mathbf{C} - \omega^2\mathbf{M}} \tag{2.9}$$

In the equation above, $\mathbf{u}(\omega)$ is the displacement vector, while $\mathbf{M}$, $\mathbf{C}$ and $\mathbf{K}$ denote the mass, damping, and stiffness matrices, respectively. The external load vector in the frequency domain is expressed as $\mathbf{F}(\omega)$, and i is the imaginary part.

2.6 Empirical settlement models

Long-term railway settlements caused by cyclical repetition of vehicle passages is a frequently investigated topic in the literature (Abadi et al., 2016). Empirical settlement models are a commonly applied approach due to the possibility of calibrating against laboratory tests or field measurements, thus validating the estimated deformations with measured data. Additionally, the models enable modelling of multiple vehicle passages within reasonable computational time. In this thesis, two settlement models are employed: one for the ballast layer and one for the subgrade. These models are described in the following sections.

2.6.1 Empirical ballast settlements — Visco-plastic threshold model

The empirical long-term settlement model is a visco-plastic threshold model previously used in studies conducted by Nasrollahi, Ramos et al. (2024) and Nasrollahi et al. (2023, 2026). The formulation is typically evaluated iteratively, where each iteration represents a set number of load cycles. For a given iteration step j and sleeper i, the incremental settlement $\delta_{i,j}$ may be expressed according to Equation 2.10.

$$\delta_{i,j} = \sum_{n=1}^{N_\mathrm{w}} \left\{ \sum_{k=1}^{N_\mathrm{k}} \alpha_k \left[\frac{\max(F_{\mathrm{s/b},i})_n - F_{\mathrm{th},i}}{F_0} \right]^{\beta_k} \right\} \tag{2.10}$$

In the equation above, the number of wheels in the vehicle model is denoted N_w, $\max(F_{\mathrm{s/b},i})_n$ is the maximum sleeper-ballast contact force induced at each wheel passage n and $F_{\mathrm{th},i}$ is a threshold load value, and permanent deformation is assumed to occur when $\max(F_{\mathrm{s/b},i})_n > F_{\mathrm{th},i}$. The denominator F_0 is a reference load, set to

1 kN which ensures non-dimensionality. Furthermore, α_k and β_k are empirical model parameters and $\mathrm{N_k}$ is the empirical polynomial degree of the settlement formulation.

The total accumulated ballast settlements $\Delta_i(n_s)$, beneath a sleeper i after iteration n_s is obtained by summing the incremental settlements $\delta_{i,j}$ according to Equation 2.11.

$$\Delta_i(n_s) = \sum_{j=1}^{n_\mathrm{s}} \delta_{i,j} \tag{2.11}$$

Repetition of vehicle passages results in gradual densification and stabilisation of the ballast track. To account for this phenomenon, the threshold load that governs the deformation is updated based on the accumulated settlements according to Equation 2.12.

$$F_{th,i}(\Delta_i) = F_{th,\infty} - (F_{th,\infty} - F_{th,0})e^{-\gamma\Delta_i} \tag{2.12}$$

The initial threshold value before any traffic loads is denoted $F_{th,0}$, while $F_{th,\infty}$ is a threshold value that corresponds to a stabilised track in the long-term. The hardening parameter γ represents the hardness of the ballast due to compaction. As the accumulated settlements increase for each iteration step, the threshold value $F_{th,i}(\Delta_i)$ approaches the stabilised threshold value $F_{th,\infty}$, which represents the densification and stabilisation of the ballast layers during repeated vehicle passages.

The visco-plastic threshold model estimates the permanent ballast deformations, however, it does not account for the subgrade settlements, which are primarily driven by creep and consolidation effects.

2.6.2 Subgrade settlement — Li-Selig model

A commonly applied empirical approach for predicting the permanent long-term subgrade settlements was proposed by Li and Selig (Li & Selig, 1996). The formulation relates the permanent vertical strains to the stress state of individual soil layers in a given soil stratigraphy. The stress acting at the surface q may be expressed as the maximum sleeper-ballast contact force $F_{s/b}$, divided by the base area of a sleeper A, as in Equation 2.13.

$$q = \frac{F_{s/b}}{A} \tag{2.13}$$

The initial vertical stress at depth z may be expressed according to Equation 2.14, following the general linear stress theory, where γ denotes the unit weight of the overlying material and q_0 is the initial surface stress.

$$\sigma_{v_0} = q_0 + \gamma z \tag{2.14}$$

Following conventional soil mechanics assumptions, the compressive strength may be expressed according to the Mohr-Coulomb failure criterion as presented in Equation 2.15. Here, ϕ denotes the internal friction angle and c represents the cohesive strength of the soil.

$$\sigma_s = \sigma_{v_0} \tan \phi + c \tag{2.15}$$

The deviatoric stress is obtained from the major and minor principal stresses σ_1 and σ_3, respectively, as defined in Equation 2.16.

$$\sigma_d = \frac{\sigma_1 - \sigma_3}{2} \tag{2.16}$$

As shown in Equation 2.17, the Li-Selig formulation relates the accumulated plastic strain in soil layer k after N loading cycles.a, b and m are empirical material parameters that are experimentally determined for various soil types. Furthermore, $\sigma_{d,k}$ and $\sigma_{s,k}$ denote the deviatoric stress and the compressive strength in layer k, respectively. Typical parameter value ranges for the empirical soil parameters are presented in Table 2.1 (Li & Selig, 1996).

$$\varepsilon_{p,k} = a \left(\frac{\sigma_{d,k}}{\sigma_{s,k}} \right)^m N^b \tag{2.17}$$

Table 2.1: Typical parameters a, b, and m for common subgrade soils (Li & Selig, 1996)

Subgrade soil type	a	b	m
ML (silt)	0.64	0.06–0.17	1.4–2.0
MH (silt, high plasticity)	0.84	0.08–0.19	1.3–4.2
CL (clay, low plasticity)	0.30–3.5	0.08–0.34	1.0–2.6
CH (clay, high plasticity)	0.82–1.5	0.12–0.27	1.3–3.9

The individual permanent settlement contribution associated with each soil layer k may subsequently be expressed according to Equation 2.18.

$$s_k = \varepsilon_{p,k} h_k \tag{2.18}$$

Through the summation of all K permanent deformation contributions s_k, the total permanent subgrade settlements may be obtained, as shown in Equation 2.19.

$$\Delta_{\text{subgrade}} = \sum_{k=1}^{K} s_k \tag{2.19}$$

The total permanent settlements due to repeated vehicle passages is expressed as the sum of the contributions: permanent ballast/sub-ballast deformations and permanent subgrade deformations as shown in Equation 2.20.

$$\Delta_{\text{total}} = \Delta_{\text{subgrade}} + \Delta_{\text{ballast}} \tag{2.20}$$

2.7 Dry deep mixing as mitigation technique

Dry Deep Mixing (DDM) is a soil stabilisation technique in which soil and binders are mixed, creating columns with increased strength and stiffness properties. Lime and cement are the most common binders with the DDM method and are the reasons why the columns are known as Lime-Cement Columns (LCCs). In Sweden, the stabilisation method is primarily used to reduce settlements, mitigate vibrations, and ensure stability for both road and railway embankments on soft soil. The method is applicable for various types of soils, but preferably soils with high moisture content such as cohesive soils and peat. The high moisture content is essential due to the reaction that occurs between the water in the soil and the binders that initiate the solidification and hardening process of the mixture (R. Larsson, 2006).

LCCs are cylindrical in shape and in the Nordic countries typically installed with diameters ranging between 0.5 and 0.8 m and to a depth of 7.5-15 m, although it is possible to use DDM to a depth of 25 m (R. Larsson, 2006). The maximum depth of 25 m is governed by technical constraints of the mixing equipment, such as torque and penetration capacity, which affect the mixing quality. LCCs can be installed as floating or end-bearing, which means that floating columns are fully surrounded by soft soil and transfer loads primarily through shaft resistance at the soil-column interface. For end-bearing installation, the columns instead extend to an underlying stratum with better strength and stiffness properties, and the load is transferred at the column tip through base resistance. Depending on the aim of the stabilisation, the columns can be configured in various patterns, although, for settlement reduction, the columns are generally installed as single columns in a triangular or square pattern with a centre to centre spacing (ctc). The columns can also be installed as overlapping with various block type patterns (European Committee for Standardization, 2005).

Since LCCs are a product of mechanical mixing of cementitious binders and naturally formed geomaterials, the layering and the spatial variability of the natural soil will affect the quality and homogeneity of the columns. Several studies have been conducted to investigate the spatial variability of lime cement columns (S. Larsson et al., 2005; Wong et al., 2024). In addition, installation processes such as the number of mixing blades have significant influence on the strength and stiffness properties of the columns, findings also indicate that high variability may be observed despite a thorough and consistent installation process (S. Larsson & Nilsson, 2005).

2.8 Random variables and random fields

A random variable X is a function defined in a sample space S that assigns a real number $X(s_i)$ to each outcome $s_i \in S$. Random variables are characterised by an associated probability distribution, often expressed in the form of a probability density function (PDF), which defines the likelihood of different outcomes. The distribution is governed by statistical descriptors such as the mean $\bar{\delta}$ and the standard deviation s. The mean represents the average value while the standard deviation quantifies the dispersion of values around the mean. These descriptors are useful to describe the uncertainties and variation of geomaterial properties (Griffiths & Fenton, 2007).

Random fields are an extension of the concept of random variables, where random variables are assigned to every location in a spatial domain (Hristopulos, 2020). This formulation allows material properties to vary spatially in a statistically consistent manner while accounting for inherent uncertainty.

Random fields are mathematically constructed by marginal probability distribution and a spatial dependence structure, typically described by a covariance (or correlation) function. The probability distribution determines the sample space and the probability of different outcomes. The spatial covariance function describes the relationship between variables at different locations. Together, the marginal distribution and the covariance structure fully define the stochastic model of the random field. This results in fields that exhibit both local correlation and spatial variability. Various probability distributions may be used depending on the application, with Gaussian (normal) distribution being the most common. Normal distribution is characterised by its symmetric bell shape, where both mean and median is located at the central symmetry line. Other commonly used distribution functions are lognormal and gamma distributions both of which are used to model right-skewed data.

Common covariance (or correlation) models include exponential and Gaussian functions. These functions describe how the correlation between two points decreases with increasing separation distance. The exponential model is characterised by its rapid growth or decay with distance, while Gaussian correlation is smooth resulting in less aggressive transitions between variables with distance. The spatial correlation structure is often quantified by the scale of fluctuation, which represents the distance over which the random field remains significantly correlated.

2.9 Analysis of sensitivity and spatial variation

The response or outcome of a model is a product of its inputs. In trying to model a specific scenario, one would like these inputs to have a specific known value, making the response of the model deterministic. In geotechnical engineering however, this is a rare occurence due to uncertainty in mechanical soil properties (Griffiths & Fenton, 2007). With uncertain inputs, the model response will inherently be uncertain as well. Through Global Sensitivity Analysis (GSA), uncertainties in model input parameters and how they impact the response of the model is quantified. This allows for a comparison in importance between input parameters. The response of the model may be greatly sensitive to some parameters, while the impact from others is negligible. One common technique is One-Factor-At-a-Time (OFAT), where one input parameter over a set of multiple is varied over a range while the others are kept constant (Montgomery, 2013). OFAT is applicable if the input parameters have a completely independent effect on the response compared to each other, but this is seldom the case (Montgomery, 2013). Since only one variable is varied at a time, any possible interaction effects between variables is not evaluated with this technique. To overcome these limitations, a technique that varies all parameters simultaneously is required. One such technique is factorial design.

2.9.1 Fractional factorial design

Factorial design is a systematically structured experiment design for estimating the main effects and interaction effects of a set of factors on the response of a model, or experiment. A main effect is the change in response due to a level change in one of the factors, while an interaction effect is the change in response caused by simultaneous level changes in multiple factors. To obtain these effects, all possible combinations of factor levels are analysed as separate analyses. The number of required analyses, or runs, is determined by the number of factors and the number of levels each factor adopts. A two-level full factorial design with k factors, the number of required runs is 2^k. In a two-level design, the effects are estimated as the difference between the average response of a factor at its low and high level. This means that the estimated effects are only valid within the level range of a factor, and the response is assumed to be linear across that range (Wu & Hamada, 2021). As an example, in a 2^2 factorial, with the two factors being A and B at a low ($-$) and high ($+$) level, every possible combination of factor levels is stored in its contrast matrix $\mathbf{C}$. Each row in the contrast matrix represents a run while each column contains the contrast coefficient of each main factor. The contrast matrix can also be extended to include the interaction effects by multiplying the signs of the respective factors the interaction consists of (Box et al., 2005). An example of a table of contrast for the 2^2 factorial is presented in table 2.2 for the two factors A and B and their interaction is AB. The last column in the table consists of the response y_i of every run.

Table 2.2: Contrast table of the 2^2 full factorial.

Run	A	B	AB	Response
1	$-$	$-$	$+$	y_1
2	$+$	$-$	$-$	y_2
3	$-$	$+$	$-$	y_3
4	$+$	$+$	$+$	y_4

All main and interaction effects of the response is calculated as in Equation 2.21.

$$\mathbf{e} = \frac{2}{n}\mathbf{C}^{\mathrm{T}}\mathbf{r} \tag{2.21}$$

Where $\mathbf{r}$ is a column vector composed of each response y_i of n number of runs. $\mathbf{C}$ is the extended contrast matrix containing the main and interaction contrast coefficients levels of each run. As previously stated, an estimated effect is the difference between the average response of a factor at its low and high level. So, the main effect of factor A using Table 2.2 can be calculated with Equation 2.22 (Wu & Hamada, 2021).

$$\mathbf{e}_A = ME(A) = \bar{y}(A+) - \bar{y}(A-) = \frac{y_2 + y_4}{2} - \frac{y_1 + y_3}{2} \tag{2.22}$$

In order to cover every possible combination of factor levels and therefore accurately predict all interaction effects, the number of runs required in full factorial design can quickly become too many with a higher number of factors k. It is possible to reduce the number of runs required while still being able to estimate main effects and low-order interactions (Montgomery, 2013; Wu & Hamada, 2021). This is done using only a fraction of the full factorial design called fractional factorial design using 2^{k-p} runs with a $(\frac{1}{2})^p$ fraction of a 2^k full factorial design (Box et al., 2005). In fractional factorial design, high-order interactions are intentionally confounded with low-order interactions. It is assumed that high-order interactions will be negligible, making it possible to differentiate low-order interactions from the higher-order interactions without requiring a larger number of runs. By assigning one factor (or more) as the product of contrasts for multiple others, that factor no longer varies independently, thus fewer runs are required.

The contrast table in Table 2.2 depicts a 2^2 full factorial and can be used for three factors fractional by assigning the third factor C as C = AB. This last relation is called the generator of the fractional factorial design and in this case reduces the number of required runs from 2^3 in a full factorial to 2^{3-1} since factor C does not employ different levels separately from the other factors. This alias relationship is also used for the defining relation **I** of the fractional factorial design which is the equation that forms a column of +'s through the multiplication of all columns in the contrast table. With this example, the defining relation, also called identity, is $\mathbf{I} = \mathrm{ABC}$. By multiplying the defining relation by the factors of the contrast table the aliasing structure of the design is provided, as shown in Derivation 2.23 (Box et al., 2005; Montgomery, 2013).

$$\begin{aligned} \mathrm{A} \times \mathbf{I} &= \mathrm{A} \times \mathrm{ABC} = \mathrm{A}^2\mathrm{BC} \to \mathrm{A} = \mathrm{BC} \\ \mathrm{B} \times \mathbf{I} &= \mathrm{B} \times \mathrm{ABC} = \mathrm{B}^2\mathrm{AC} \to \mathrm{B} = \mathrm{AC} \\ \mathrm{C} \times \mathbf{I} &= \mathrm{C} \times \mathrm{ABC} = \mathrm{C}^2\mathrm{AB} \to \mathrm{C} = \mathrm{AB} \end{aligned} \tag{2.23}$$

Since the identity governs the aliasing structure, it also prescribes the resolution (R) of the fractional factorial design as being the length of the shortest word in the identity. With just one generator consisting of three letters, $\mathbf{I} = \mathrm{ABC}$, the example above is said to have a resolution of III and the design is described as 2^{3-1}_{III} (Montgomery, 2013). Higher resolution designs are in most scenarios preferred since low-order interactions become aliased with fewer other low-order interactions (Box et al., 2005). Montgomery (2013) and Wu and Hamada (2021) list the following general properties of fractional factorial designs with different resolutions.

- **Resolution III**
  - Main effects: Not aliased with each other. Aliased with two-factor interactions.
  - Two-factor interactions: Some are aliased with other two-factor interactions.
- **Resolution IV**
  - Main effects: Not aliased with each other. Some aliased with three-factor interactions.
  - Two-factor effects: Aliased with each other.
- **Resolution V**
  - Main effects: Not aliased with each other. Some aliased with four-factor interactions.
  - Two-factor effects: Aliased with three-factor interactions.

If the effect of a factor proves to be negligible compared to the effects of the other factors in the same response, it may be excluded from consideration allowing de-aliasing of interactions (Wu & Hamada, 2021). For example, if factor B in the 2^{3-1}_{III} factorial design is negligible all interactions consisting of that factor can be considered negligible as well and the alias structure in Derivation 2.23 transforms into the de-aliased effects in Derivation 2.24.

$$\begin{aligned} \mathrm{A} &= \mathrm{BC} \to \mathrm{A} \\ \mathrm{B} &= \mathrm{AC} \to \mathrm{AC} \\ \mathrm{C} &= \mathrm{AB} \to \mathrm{C} \end{aligned} \tag{2.24}$$

2.9.2 Spatial variation analysis

In order to quantify variation in data, the use of the coefficient of variation, CV, is common in engineering practises (Fenton & Griffiths, 2008). It is expressed as the ratio between the standard deviation s and the sample mean $\bar{\delta}$, as in Equation 2.25.

$$CV = \frac{\sqrt{s^2}}{\bar{\delta}} \tag{2.25}$$

Where s^2 is the variance with a sample size of n according to Equation 2.26. $\bar{\delta}$ is the average of n observations δ_i according to Equation 2.27.

$$s^2 = \frac{1}{n-1} \sum_{i=1}^{n} \left(\delta_i - \bar{\delta}\right)^2 \tag{2.26}$$

$$\bar{\delta} = \frac{1}{n} \sum_{i=1}^{n} \delta_i \tag{2.27}$$

CV is a good metric for how much data varies in itself but variation in any dimensional property the data might have is not captured. The spatial correlation in the data can be obtained through the use of semivariograms. The semivariogram consists of the semivariance function $\gamma(h)$ which represents the disparity in value between two points separated by distance h, called lag (S. Larsson et al., 2005)(Pyrcz & Deutsch, 2003). The semivariance function is defined as in Equation 2.28, where x_i and $x_i + h$ are the locations of the two points (Bachmaier & Backes, 2011).

$$\gamma(h) = \frac{1}{2n} \sum_{i=1}^{n} \left[\delta(x_i) - \delta(x_i + h)\right]^2 \tag{2.28}$$

As the lag h, increases it is expected for the semivariance to increase with it, i. e. with greater lag the correlation diminishes (Pyrcz & Deutsch, 2003). S. Larsson et al. (2005) used semivariograms to estimate the horizontal scale of fluctuation in lime-cement columns. This was possible since the semivariance proved to be monotic increasing up until a certain lag where the semivariance flattened out representing the scale of fluctuation. A monotonically increasing semivariance is not always present and can instead exhibit cyclical behaviour called the hole-effect (Pyrcz & Deutsch, 2003). With a cyclical semivariogram, the correlation between points diminishes with an increase in lag at first up to a local peak and thereafter displays an increase in correlation followed by a trough. The correlation diminishes again and the cycle continues. This cyclicity can be periodic so that $\gamma(h)$ is equal to $\gamma(h+2a_n)$ for a half period a_n as defined by an analytical hole-effect semivariance model by Pyrcz and Deutsch (2003) in Equation 2.29.

$$\gamma(h) = c_n \times \left[1.0 - \cos\left(\frac{h}{a_n}\pi\right)\right] \tag{2.29}$$

Where c_n is the variance contribution (amplitude of semivariance). a_n, called the range, is the half period of the data taken as the distance to the first peak. If the oscillatory component of the experimental variogram deteriorates with distance, a damping term as in Equation 2.30 can be added, where d represents the distance at which 95% of the oscillations have deteriorated (Pyrcz & Deutsch, 2003).

$$\gamma\left(h\right) = c_n \times \left[1.0 - \exp\left(\frac{-3h}{d}\right)\cos\left(\frac{h}{a_n}\pi\right)\right] \tag{2.30}$$

Another metric similar to that of the semivariance that instead captures the difference of each consecutive pair of observations is the mean squared successive difference (MSSD) calculated as in Equation 2.31.

$$\mathrm{MSSD} = \frac{1}{n-1}\sum_{i=1}^{n}\left[\delta\left(x_{i+1}\right) - \delta\left(x_i\right)\right]^2 \tag{2.31}$$

3 Numerical model

This chapter presents the numerical modelling framework adopted in this study for analysing the short and long-term behaviour of railway tracks on soft soil caused by dynamic loading. The modelling approach is implemented in the open-source Python-based numerical model STEM based on the finite-element method to analyse the dynamic vehicle-track-soil interaction. The chapter first introduces the case study on the Gothenburg region, including both traffic and soil conditions. The vehicle model, track model and substructure model are subsequently described along with the component properties, adopted material models, geometry and discretisation.

Furthermore, the implementation of lime-cement columns as ground improvement measures are presented, including the adopted homogenisation modelling approaches and the random field implementation to account for the spatial variability in lime cement columns (LCCs). The methodology for the long-term empirical settlement models are described along with associated assumptions. Finally, the model verification procedures, sensitivity analyses framework and a summary of the investigated scenarios are presented.

3.1 Case study in Gothenburg: soil and traffic conditions

The soil conditions in the Gothenburg region are predominantly characterised by thick deposits of soft marine clay (Bergström et al., 2022). These deposits were formed both during and after the last glacial period and are therefore commonly referred to as glacial and postglacial clay, respectively. According to studies by Tornborg et al. (2021) and Wood and Karstunen (2022), the clay layers in the Gothenburg region may extend to depths of over 100 m before reaching frictional soil or bedrock. Typically, a thin dry crust is present near the surface, underlain by very soft clay with low undrained shear strength and high natural water content. These clay deposits are, in general, normally consolidated to lightly overconsolidated, characterised by high compressibility and sensitivity to remoulding and disturbance. These geotechnical characteristics are closely related to the marine origin of the clay deposits, as freshwater infiltration over time has caused salts in the pore water to leach out, weakening the soil structure. In certain areas, this process has resulted in quick clay behaviour. These conditions make the design and construction of infrastructure, such as railway embankments, challenging due to the risk of excessive settlements, long-term deformations and stability problems (Tornborg et al., 2021).

Due to the challenging ground conditions, mitigation measures are often required to ensure adequate performance. Deep mixing methods, particularly lime-cement column (LCC) stabilisation, are widely used in Gothenburg to increase the strength and stiffness of the soft soils underlying railway infrastructure. Previous studies by Holm et al. (2002) and Bozkurt et al. (2025) have shown that LCCs can significantly reduce settlements and vibrations in combination with improving stability, and enhancing load transfer within the soil. Depending on the design requirements, the columns can function as floating columns within the clay deposit or as end-bearing columns extending to firmer soil layers. However, floating columns are often implemented due to the limited installation depth compared to the thickness of the clay layers. Deep mixing stabilisation is especially important for railway infrastructure in Gothenburg, as soft clay deposits are prone to creep and long-term deformation under repeated cyclic loading from railway traffic.

Gothenburg constitutes one of Sweden's most important railway hubs for both passenger and freight transportation, resulting in a mixed-traffic railway network with high traffic intensity. Several major railway corridors, including Kust till kust-banan, Västkustbanan and Västra stambanan, connect Gothenburg to other major urban and industrial regions in Sweden. The railway infrastructure along these corridors primarily consists of conventional ballasted tracks with the Swedish standard gauge of 1435 mm, continuously welded rails, and concrete sleepers.

In the greater Gothenburg area, railway lines are often located on thick clay deposits as previously described. Much of the infrastructure is more than 100 years old and was not originally designed for the increased traffic demand, higher axle loads and train velocities expected at present day. As a consequence many of the track components are approaching, or have exceeded, the end of their design life and require frequent maintenance or replacement to ensure operational performance.

Passenger traffic in the region mainly consists of commuter and regional trains with operating velocities up to 200 km/h. Typical passenger train axle loads range between 15-19 tonnes at full operational capacity (Aggestam & Nielsen, 2019).

3.2 Vehicle model

In STEM the vehicle model is implemented as a 2D multibody system (MBS), due to the symmetry conditions at the centreline, only half of the vehicle is modelled (StemVibrations, 2026). The vehicle model is user defined, therefore, it is possible to represent the vehicle with specific degrees of freedom (DOF) and numbers of car bodies, bogies and wheelsets. Mass properties are assigned to all vehicle components, with the carbody and bogies also including pitch moment of inertia. The vehicle components are interconnected through primary and secondary suspensions, modelled as linear spring dampers with both stiffness and viscous damping coefficients. In this study, the vehicle model was chosen to be representative of an X2000 train, since it is a common train model operating in Sweden. The X2000 train is shown in Figure 3.1 and is a tilting high-speed train with operational speeds up to 200 km/h and the axle loads typically vary between 15–19 tonnes based on the loading conditions. The vehicle interacts with the track through contact forces which are applied to the track as time-dependent external forces $\mathbf{F}_{\text{ext}}(t)$, corresponding to the external force vector presented in the equation of motion in Section 2.3

Figure 3.1: X2000 train (Hofres, 2008)

To determine the wheel-rail contact forces, a nonlinear Hertzian contact formulation was used. The contact force at each wheel position F_j is computed as a nonlinear function of the relative displacement between the wheel and the rail δ_j, governed by a Hertzian contact stiffness coefficient k_c (see eq.3.1). The computed contact forces were applied to the track model as moving point loads with a user-defined velocity, direction, and initial position.

$$F_j = k_c \times \delta_j^{1.5} \tag{3.1}$$

In this work, a vehicle model consisting of a single bogie with two wheelsets was employed. Studies with a single bogie vehicle model have previously been conducted by Aggestam and Nielsen (2019), Varandas et al. (2020) and Zuada Coelho et al. (2021). A single bogie vehicle model was deemed appropriate for this study as no transition zones or track discontinuities are considered which would be significantly influenced by the low frequency pitching motion of the carbody. Therefore, the vehicle model is represented by a 4-DOF multibody system, where the DOFs correspond to the vertical displacement and pitch rotation of the bogie and the vertical displacement of each wheel. In figure 3.2 the vehicle model is presented with the DOFs denoted u_i. A vehicle velocity of 200 km/h was chosen, representing an X2000 train at full operational speed.

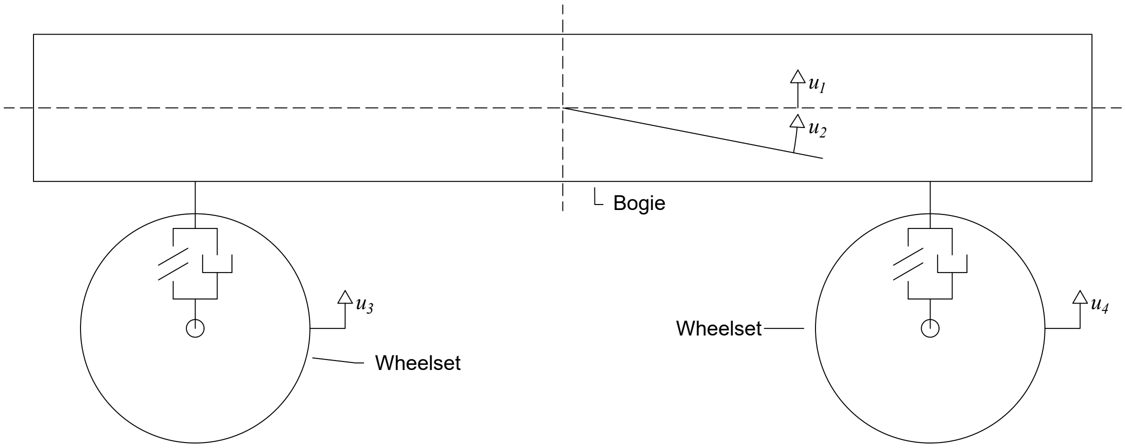

Figure 3.2: Vehicle model with 4 DOFs, consisting of a single bogie. Adapted from Zuada Coelho et al. (2021)

The vehicle parameters for the single bogie vehicle model are summarised in Table 3.1. The parameters were collected from *Benchmark Vehicle 1* by Iwnick (1998), and are representative of a typical passenger train. In the absence of a carbody, the mass of the bogie was modified to account for the carbody and to correspond to an axle load of 17.1 tonnes, which falls within the previously presented range for an X2000 train model. The default Hertzian contact coefficient, 9.1e^{-7} and contact power 1.0 were used to compute the contact forces.

Table 3.1: Vehicle parameters of a single bogie model.

Component		Symbol		Unit
Bogie	Mass	M_b	15 300	kg
	Pitch inertia	J_b	1.476×10^3	kgm^2
Primary suspension	Stiffness	k_p	1200	kN/m
	Damping	c_p	4	kNs/m
Wheelset	Mass	M_w	900	kg
-	Wheel - wheel distance	Δ_w	2.5	m

3.3 Track model

The track model was implemented as a straight track comprising one rail discretely supported by rail pads and sleepers on an extensive substructure consisting of different soil layers. The individual track components are not modelled separately, but their respective properties are instead defined in the default track generation implemented in STEM. The modelling and properties of each track component are described in the following sections. The vehicle model and the track model are shown in Figure 3.3

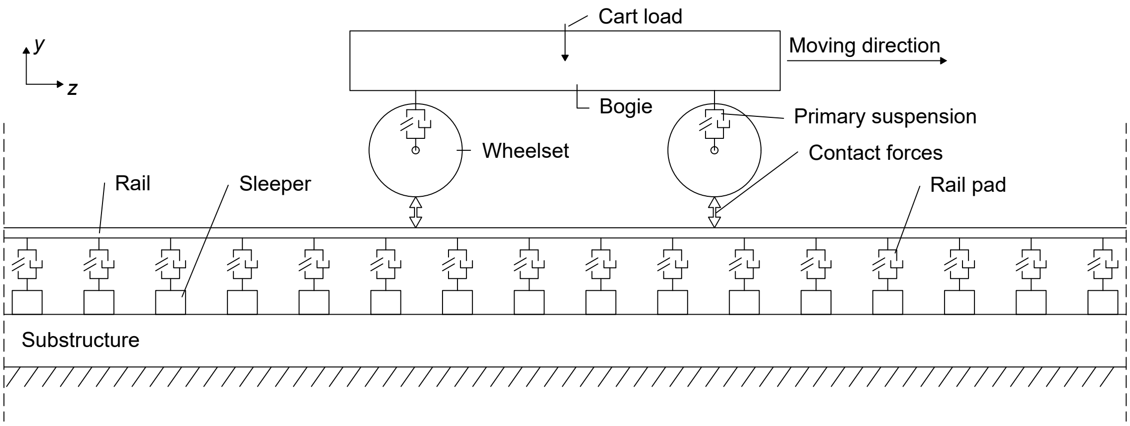

Figure 3.3: A sketch of the complete vehicle and track model with associated track components

3.3.1 Rail

The rail is represented by a 3D beam element, according to the Euler-Bernoulli beam theory, and is supported by the sleepers. The beam is defined by its material properties (density, Young's modulus, and Poisson's ratio) and cross-sectional properties (area, second moments of inertia, and torsional inertia).

In this study, the 60E1 rail profile was used in the track model as it is the most common profile in Sweden along with a track gauge of 1435 mm (Trafikverket, 2026). The rail profile was adopted from the predefined implementation in the STEM framework (STEM team, 2026), where the rail properties are implemented according to the European Standard EN 13674-1:2011+A1:2017 (European Committee for Standardization (CEN), 2017). The rail parameter values are presented in table 3.2. The cross-sectional area of the rail is denoted A_c, moments of inertia as I and subscripts denote the axis. The torsional inertia is expressed as J.

Table 3.2: Rail parameters for rail profile 60E1

ρ [kg/m^3]	A_c [m^2]	E [GPa]	ν [m^4]	I_{zz} [m^4]	I_{yy} [m^4]	J [m^4]
7850	0.00767	210	0.3	3.038e^{-5}	5.123e^{-6}	3.55e^{-5}

3.3.2 Rail Pads

Rail pads are located between the rail and each sleeper and serve to connect the rail to the supporting structure while providing vibration attenuation and load distribution (Esveld, 2014). In the track model, the rail pads are represented as elastic spring-damper elements defined by their thickness, stiffness and damping properties, in accordance with the track generation in STEM (StemVibrations, 2026).

In this study, The thickness of the rail pads in the track model was set to 10 mm, retrieved from Nasrollahi, Dijkstra and Nielsen (2024) and Nasrollahi et al. (2023).

The stiffness and damping of the rail pads were $k_{r/s}$ = 120 kN/mm and $c_{r/s}$ = 25 kNs/m, respectively, and are typical values for Swedish track design (Aggestam & Nielsen, 2019; Nasrollahi et al., 2023).

3.3.3 Sleepers

The sleepers were modelled as half sleeper linear elastic concrete elements, idealised with a rectangular prism geometry. In reality, sleepers are characterised by a more complex, non cuboid geometry, but to reduce computational complexity the sleeper dimensions were approximated from the conceptual sleeper design by Trafikverket (2012). The dimensions and material parameters of the sleepers are presented in table 3.3. The sleeper parameters correspond to a sleeper mass of 300 kg, which is the mass reported for sleeper model A28 (Abetong AB, 2023).

Table 3.3: Dimensions and material properties of the concrete sleeper

Length [mm]	Width [mm]	Height [mm]	ρ [kg/m^3]	n [-]	E [GPa]	ν [-]
2500	250	200	2400	0	30	0.2

3.4 Substructure model

This section describes the modelling approach adopted for the railway substructure and the underlying soft soil within the finite-element (FE) model. The substructure includes the embankment layers, soft soil deposit, boundary conditions, and discretisation strategy used in the computational domain. The geometry and material properties of the individual layers are presented along with chosen constitutive material model and the associated behaviour assumptions. In addition, the methodology used to determine the equivalent static stiffness at both the rail level and the sleeper-ballast interface is described. The equivalent substructure stiffness obtained from the FE model are subsequently used to evaluate the dynamic long-term response of the railway track system.

3.4.1 Subgrade soil layers with a soft soil layer

The soil can be modelled either as linear elastic or non-linear, both of which are supported by the STEM software. However, the latter requires integration through the commercial softwares Abaqus or Plaxis (STEM team, 2026). In this study, the predefined linear elastic material model in STEM was used with the assumption of drained behaviour. The linear-elastic material parameters consist of a mass part and a stiffness part. The mass is represented by the bulk density ρ according to Equation 3.2 where the porosity n was set to 0 allowing direct implementation of the bulk density as ρ_s.

$$\rho = (1 - n)\rho_s \tag{3.2}$$

The stiffness parameters are Young's modulus E, and Poisson's ratio ν, which together define the stress-strain relationship expressed as the shear modulus G in Equation 3.3.

$$G = \frac{E}{2(1+\nu)} \tag{3.3}$$

The geometry of the model was defined independently of the material model, allowing the representation of individual layers with specific geometric properties, such as layer thickness, spatial extent, and variations, including inclinations. The computational domain was constructed by defining volumes that represent soil layers and structural components. Subsequently, the material models were assigned to these volumes, resulting in distinct regions with different soil conditions.

In the FE model, the domain is represented by a finite computational region. The finite region requires boundary constraints at the outer limits of the model to ensure numerical stability and to reflect realistic behaviour as the model otherwise will be regarded as infinite. In STEM it is possible to implement Dirichlet boundary conditions such as displacement and rotation constraints. The displacement constraints are fixed in all directions and the displacements are zero. The rotation boundaries differ from displacement constraints as the boundaries can be both fixed or free depending on direction. Absorbing boundaries are also supported in STEM and are modelled with absorption factors and a virtual thickness to remove reflections from waves propagating towards the outer limit. The absorption factors are scaling factors of Lysmer type where 1.0 is optimal absorption and 0 is no absorption. Displacement constraints was applied to the base boundary of the 3D model, while a rotation constraint was implemented at the symmetry line of the model (along x=0), allowing displacement in the vertical direction, y, while fixed in the x and z directions. Absorbing boundaries are implemented at the outer limits of the model in the direction of travel and the limiting plane opposite the embankment centerline. They are modelled with 40 m virtual thickness and absorption factors corresponding to optimal absorption.

The computational domain was discretised by assigning element sizes to the defined volumes, resulting in a finite number of elements. The accuracy and computational efficiency of the simulation depend on the mesh resolution, which is specified as element sizes with a maximum characteristic length in metres. The element size were chosen to be smaller than the characteristic dimensions of the assigned volumes to ensure adequate geometric representation. Regions of particular interest, such as areas near the train load application, were modelled with a finer mesh resolution, i.e., in the ballast layer, where higher stress and displacements gradients are expected.

The geometry of the 3D-model considered in this study is theoretical and does not represent any specific existing embankment or soil stratigraphy. Instead, the embankment geometry was based on a standard design for a ballasted, single straight track on soil, as specified in TDOK 2015:0198 by Trafikverket (2015). The standard design incorporates concrete sleepers, 60E1 rail and 1435mm track gauge, and allows a maximum axle load of 25 tonnes and train velocities below 250 km/h. The height of sub-ballast was determined by the standard RA DCH.1/1 for frost protection in Gothenburg, from RA Anläggning 20 (Svensk Byggtjänst, 2020). The resulting embankment geometry and layering is illustrated in figure 3.4.

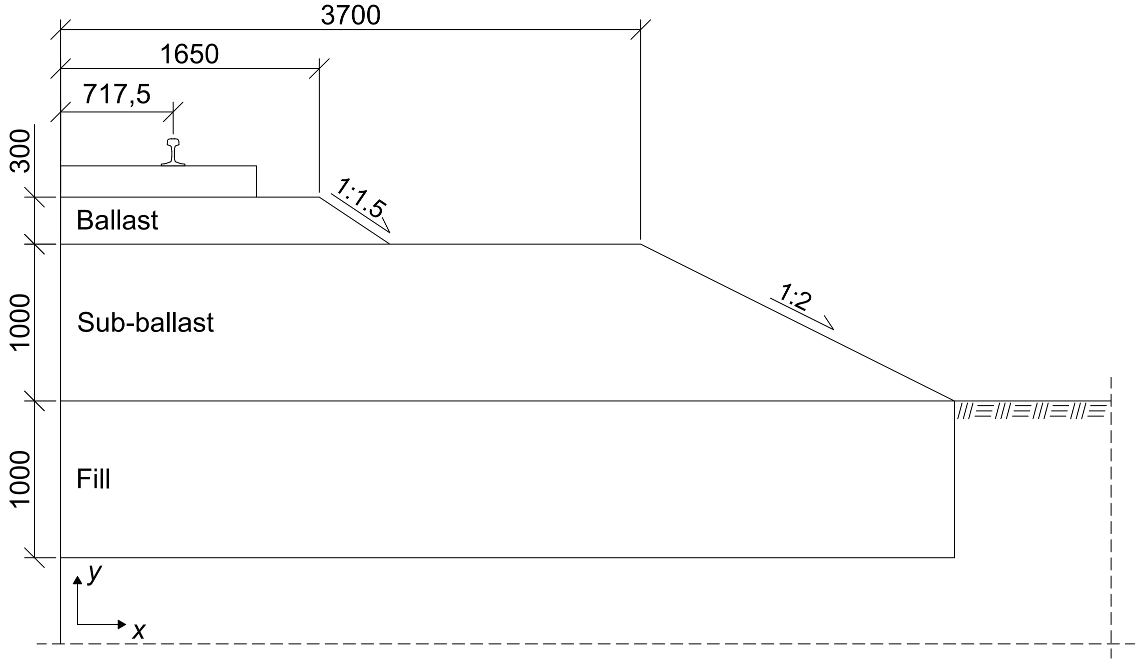

Figure 3.4: The embankment geometry and dimensions expressed in millimeters

The complete geometry and stratigraphy, consists of the embankment and an underlying natural clay, and is presented in Figure 3.5. The profile represents the natural ground conditions adopted in this study and forms the basis for all subsequent analyses. The height of the soil domain is 17.3 m while the total width is 10 m. The FE model is 48 m long and comprises a total of 81 sleepers, with 0.6 m sleeper spacing.

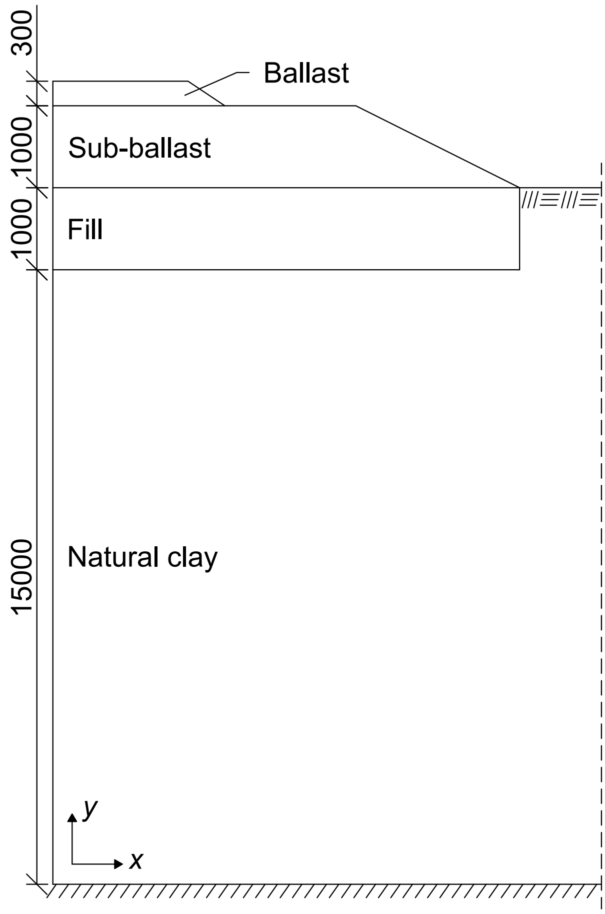

Figure 3.5: The model stratigraphy, with dimensions expressed in millimeters. Vertical dimensions are not to scale.

The properties of the embankment materials and the soft soil layer are presented in Table 3.4. The values of the ballast and sub-ballast parameters were adopted from previous studies by Nasrollahi, Dijkstra and Nielsen (2024) and Nasrollahi et al. (2023) conducted under Swedish conditions, and are considered representative of typical ballasted railway tracks. The elasticity modulus of the ballast layer was adjusted to represent improved ballast quality, based on correspondence with the main author. Furthermore, mineral soil was assumed for the embankment fill based on TDOK 2015:0198 by Trafikverket (2015) and the material parameters were obtained from TDOK 2013:0667 (Karlsson & Moritz, 2016) and represent standard geotechnical design values. The density of the clay layer was collected from TDOK 2013:0667, whereas an elasticity modulus of 5 MPa was assumed, reflecting a conservative consideration based on the results of laboratory tests of Gothenburg clay reported by Jonefjäll and Sabattini (2022).

Table 3.4: Material parameters of the individual soil layers in the model stratigraphy

Layer	Thickness [m]	Density ρ [kg/m^3]	Poisson's ratio ν [-]	Elasticity modulus E [MPa]
Ballast	0.3	1800	0.2	120
Sub-ballast	1	2200	0.3	175
Fill	1	2000	0.2	30
Clay	15	1600	0.2	5

3.4.2 Equivalent static substructure stiffness

In this work, the equivalent stiffness was determined numerically in STEM using the developed FE model. The equivalent substructure stiffness was evaluated at the sleeper-ballast interface. The approach is based on the Winkler stiffness model in combination with Hooke's law, which together describes the relationship between applied pressure and the resulting displacement through a linear elastic foundation response according to the theory presented in Section 2.4. Quasi-static vertical point loads were applied on top of the sleepers at the rail seat position. Since all materials were modelled as linear-elastic and the response satisfied elastic superposition, the load was applied in a single load step. The resulting response was verified against an incrementally ramped loading approach, which produced identical deformations. The vertical displacements under the sleepers were determined for the individual load cases. The equivalent stiffness response was calculated according to Equation 3.4.

$$k_{eq} = \frac{F}{u_y} \tag{3.4}$$

The methodology yields an equivalent stiffness consistent with a series spring formulation since the FE model incorporates the material and geometry parameters of each layer in a manner consistent with the analytical definition of the stiffness of a bar (soil layer) element with a given length and cross-section, i.e., $k_i = EA/L$.

3.5 Lime-cement columns as mitigation measures in soft soil layers

In finite-element modelling, it is a frequent practice to model lime cement columns as a homogenised material since it often proves effective without compromising the validity of the results. In section 3.5.1, the modelling approaches for the lime-cement columns (LCCs) are explained in detail. The implementation is performed with homogenised materials, while the incorporation of random fields is covered in 3.5.2, these modelling approaches allow the evaluation of the impact of spatial variability in LCCs as a result of dynamic railway loading.

3.5.1 Modelling LCCs with volume averaging

In this study, the LCCs were primarily modelled as a homogenised material to reduce the number of nodes and elements compared to explicit modelling of individual columns, which would require significantly finer mesh refinement. This approach reduces computational cost. However, a single analysis with individual square columns was performed to compare and verify the validity of the homogenised modelling approaches. LCCs are circular by nature, but this was highly complicated and time consuming to implement in STEM, which is why a square column face was implemented instead.

The two alternative modelling approaches considered for homogenised LCCs were a homogenised block and homogenised walls oriented perpendicular to the track. The implementations of these approaches are presented in Figures 3.6b and 3.6c respectively together with individually modelled columns in Figure 3.6a for comparison.

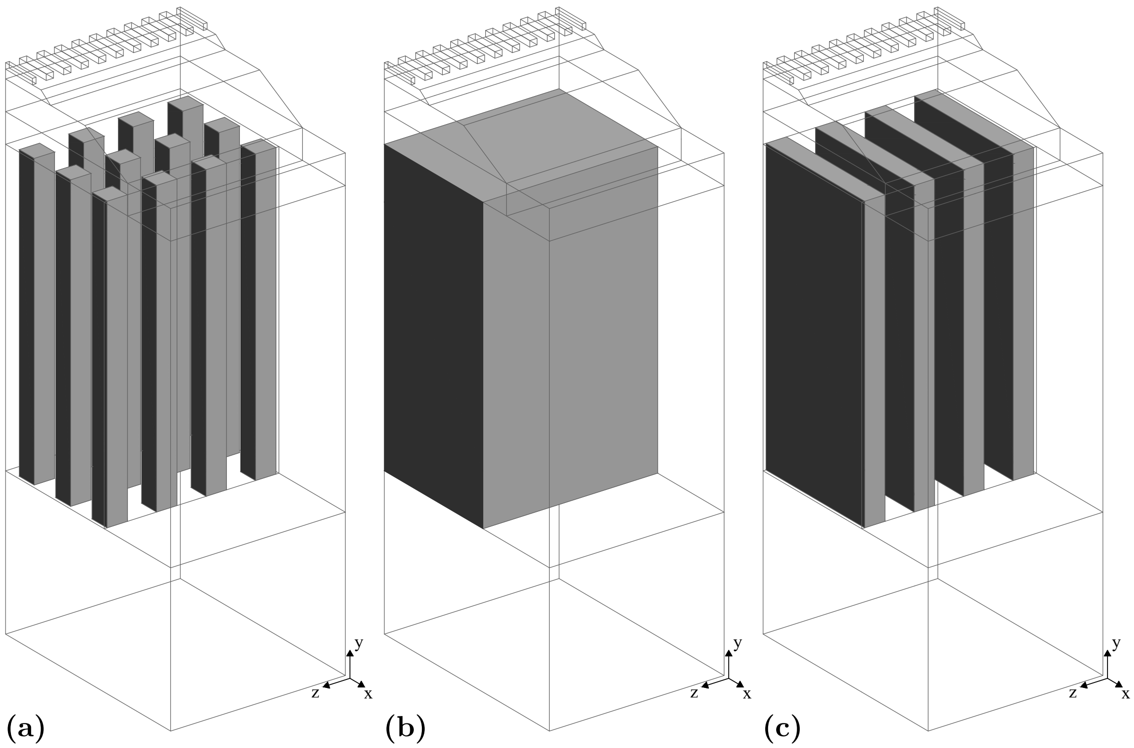

Figure 3.6: Alternative modelling approaches for LCC models. **(a)** Individual square LC columns, **(b)** LC columns as a block, **(c)** LC columns as walls

The stabilisation approaches were modelled in the soil domain by replacing the clay volume with a reinforced volume for the block and multiple wall volumes for the second approach. Subsequently, these volumes were assigned homogenised material models, where material properties were obtained through basic volume averaging, following a methodology adapted from Bozkurt et al. (2023), in which lime cement columns are represented as a stabilised block in finite-element analysis using Plaxis 2D. In the present study, the approach is extended to three dimensions by performing averaging based on volume fractions rather than area fractions. The soil stabilisation was limited to the natural clay, and the stabilisation zone in the context of the full geometry is presented in Figure 3.7.

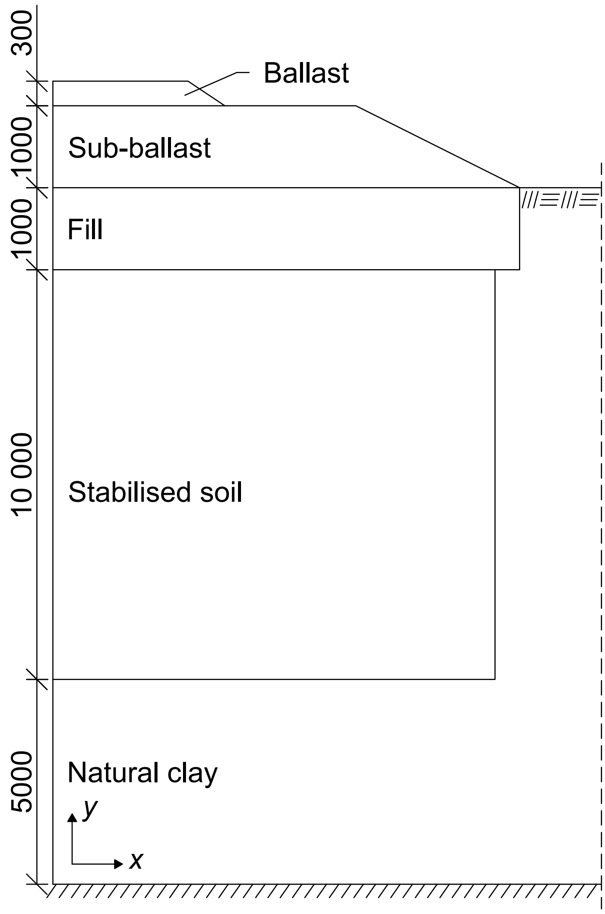

Figure 3.7: The model stratigraphy with soil stabilisation by lime-cement columns. Dimensions are expressed in millimeters. Vertical dimensions are not to scale.

In the first approach, the columns and surrounding soil were homogenised as a single stabilised block using volume averaging, as defined in Equation 3.5. The parameter $\Omega_{columns}$ denotes the volume fraction of the columns, defined as the total column volume divided by the bulk volume, while the soil volume fraction, Ω_{soil}, follows as $\Omega_{soil} = 1 - \Omega_{columns}$.

$$E_{block} = \Omega_{columns} \times E_{columns} + \Omega_{soil} \times E_{soil} \tag{3.5}$$

In the second approach, where the lime cement columns are modelled as stabilised walls, the same volume averaging principle was applied, as shown in Equation 3.6, with the distinction that $\Omega_{columns}$ is defined locally for each wall. The wall width correspond to the column side, while the soil volume fraction is defined in the same manner as the block approach.

$$E_{wall} = \Omega_{columns} \times E_{columns} + \Omega_{soil} \times E_{soil} \tag{3.6}$$

The volume averaged stiffness, E_{block} and E_{wall} was calculated based on the assumptions that the height and width of the reinforcement zone are 10 m and 4.6 m, respectively. Furthermore, the individual columns have a square interface with 0.7 m sides and were assumed to be installed in a square pattern with 1.7 m centre-to-centre distance. In Figure 3.8, the installation pattern is visualised with ctc denoting the centre-to-centre distance and b_p the sides of the column. The modulus of elasticity of the columns was chosen as 75 MPa, based on Bozkurt et al. (2023).

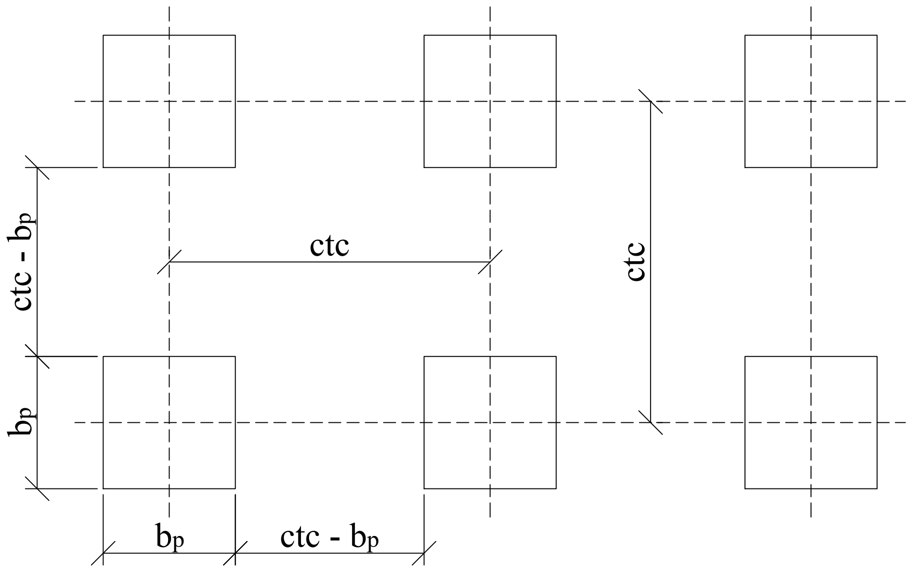

Figure 3.8: Installation pattern schematic of the LCCs

The homogenised material was implemented in STEM as linear-elastic materials as described in Section 3.4.1. The mass properties and the Poisson's ratio of the homogenised volumes were assumed to be equal to the values of the surrounding soft soil in accordance with Swedish design guidelines (Svenska Geotekniska Föreningen, 2000), while the elastic modulus parameter was defined by the volume averaged stiffness, E_{block} and E_{wall}, the material properties of the stabilisation domains and the individual columns are presented in Table 3.5.

Table 3.5: Lime cement properties

Reinforcement	Ω_{column}	Density ρ [kg/m^3]	Poisson's ratio ν [-]	Elasticity modulus E [MPa]
Column	1.0	1600	0.2	75
Block	0.18	1600	0.2	17.6
Wall	0.46	1600	0.2	37

3.5.2 Modelling LCCs with random field

In this study, random fields were implemented in combination with homogenised stabilisation (described in Section 3.5.1) to model and analyse how the spatial variability of lime cement columns affects the dynamic response of the vehicle-track-soil interaction.

The predefined random field generator in STEM was used, where each element in a defined volume is assigned a random variable value. The random field generator requires a probability density function and parameter values for the coefficient of variation CV, vertical scale of fluctuation θ_y, anisotropy A and mean value μ. The distribution of values is controlled by the coefficient of variation, defined as the ratio between the standard deviation s, and the mean value $\bar{\delta}$ (as in Equation 2.25), while the spatial correlation is dictated by the scale of fluctuation and anisotropy. The anisotropy parameter were implemented as a two element list, where the first element defines the anisotropy in the x direction, perpendicular to the track, while the second element corresponds to the z direction, i.e,. direction of travel. The anisotropy was defined as the ratio between the horizontal scale of fluctuation $\theta_{x,z}$ and the vertical scale of fluctuation as in Equation 3.7.

$$A_x = A_z = \frac{\theta_{x,z}}{\theta_y} \tag{3.7}$$

The random field parameters: coefficient of variation and both vertical and horizontal scale of fluctuations were collected from Wong et al. (2024) and represent individual columns in Gothenburg clay. The mean value was taken as the elasticity modulus of the LCC defined in Section 3.5.1 and a Gaussian covariance function was chosen. The coefficient of variation was kept constant, whereas the scale of fluctuations was varied within the reported range, including minimum, average, and maximum values. These parameters are presented in Table 3.6 and define the distribution and spatial correlation structure of the random fields.

Table 3.6: Scale of fluctuation and coefficient of variation from Wong et al. (2024)

Type	θ_y [m]	$\theta_{x,z}$ [m]	CV [-]
Average	1.4	1.6	0.26
Min	0.4	0.4	0.26
Max	3.5	4.3	0.26

Five different random fields were modelled to account for the uncertainty in spatial variability. The random fields were generated using combinations of the scale of fluctuation values presented above, enabling a parametric study and the assessment of bounding cases. A summary of the random fields labeled I-V is presented in table 3.7, with the corresponding coefficient of variation, scale of fluctuations and mean values. Visualisations of these random fields in the xy-plane at x = 0 are presented in Appendices A.1 and A.2 for the Block and Wall configuration respectively.

Table 3.7: Implemented random field realisations, with corresponding parameter values

Name	Type	CV [-]	θ_y [m]	$\theta_{x,z}$ [m]	$\bar{\delta}$ [MPa]
I	Average	0.26	1.4	1.6	75
II	Max	0.26	3.5	4.3	75
III	Min	0.26	0.4	0.4	75
IV	Min/Max	0.26	0.4	4.3	75
V	Max/Min	0.26	3.5	0.4	75

The variability parameters adopted in this study are defined on individual columns, whereas the LCCs in the numerical model are represented by homogenised stabilised volumes. This mismatch implies that the random field cannot be directly assigned to the finite elements in the homogenised domains. Instead, a two-step procedure was used. First, a random field was generated over the homogenised volumes using the statistical properties corresponding to the individual columns. Consequently, the generated realisations are centred around the column-scale mean value of 75 MPa, rather than the homogenised stiffness obtained from volume averaging. To ensure consistency with the homogenised representation, the generated field was subsequently transformed using the volume-averaging relationship defined in equations 3.5 and 3.6. Through this transformation, the stochastic realisations are mapped from individual column properties to equivalent homogenised properties, such that the resulting field simultaneously reflects the prescribed variability of individual columns while remaining representative of the averaged stiffness of the stabilised volumes. An example of distribution for column and subsequent transformation to block and wall is visualised in figure 3.9.

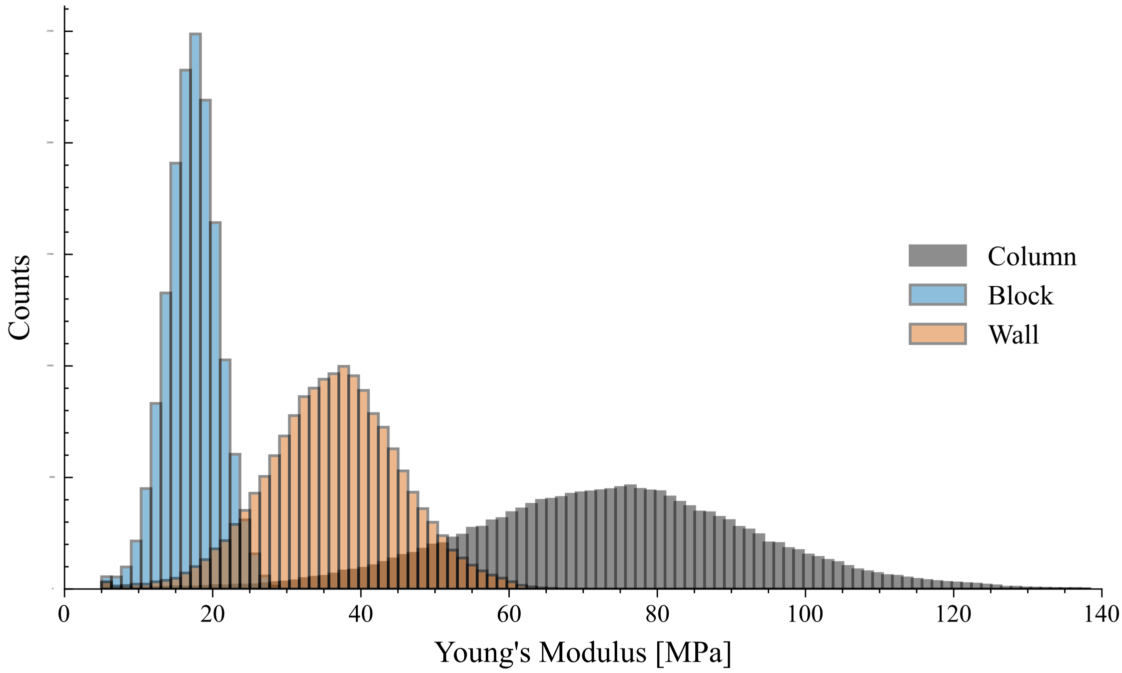

Figure 3.9: Example of distribution of one random field realisation with transformation.

3.6 Short-term dynamic vehicle-track-soil interaction in STEM

In this study, the short-term analyses were performed in STEM, where the dynamic response is captured for a single vehicle passage, in this work the vehicle model comprises a single bogie, detailed in Section 3.2. The dynamic equilibrium equation presented in section 2.3 was solved in the time domain with stepwise integration using the built in Linear Newton-Raphson strategy based on the Newmark method. The solution strategy yields a system of linear equations which was solved numerically with a linear conjugate gradient (Cg) solver. The time-step was 0.001 s for all analyses, and the convergence criterion for the solver consisting of relative displacement tolerance and absolute displacement tolerance were 10^{-4} and 10^{-9}, respectively.

The vehicle-track-soil interaction (VTSI) analysis generates a set of responses for each element in the discretised domain. The responses are for example rail node and sleeper displacement, as well as stress and strain distribution in different layers and elements. These metrics are used to evaluate the performance of the system and to examine the dynamic response as a result of material properties, LCCs implementations, and spatial variability.

3.7 Long-term settlement using an iterative framework

In this study, long-term track settlement was estimated using the empirical models presented in Section 2.6. The visco-plastic threshold model was used to estimate the permanent settlements in the ballast and sub-ballast layers, while the subgrade deformations were predicted according to Li and Selig (1996), specified in Section 2.6.2. This approach was adopted since settlements may develop in either the granular layers or the subgrade, depending on the local site conditions. In addition, spatial variability in soil properties may result in non-uniform settlement along the track. Therefore, an iterative procedure is used to predict the long-term accumulated differential settlement under a given traffic load (Nasrollahi et al., 2026).

3.7.1 Settlement in ballast and sub-ballast layer— visco-plastic threshold model

The ballast and sub-ballast deformations were estimated based on the theory described in Section 2.6.1. In this study, the maximum number of load cycles for each iteration was set to 10^5. However, as the number of load cycles depends on the maximum amount of settlement prescribed for a single iteration $\max(\delta_{i,j})$, the maximum allowable settlement was taken as $\max(\delta_{i,j}) = 0.2$ mm, following the recommendation of Nasrollahi et al. (2023) and Nielsen and Li (2018). This value is deemed to offer a reasonable balance between computational efficiency and numerical accuracy. The threshold force $F_{\text{th},i}$ was assumed to be 25 kN, and the empirical model parameters α_k, β_k and γ were assumed to be 0.0002 mm per 1000 load cycle, 2.8, and 0.11, respectively. The simulation was performed to represent a year's worth of vehicle passages while the same vehicle and track parameters from the short-term analyses were implemented. The obtained equivalent substructure stiffness for each investigated scenario was applied to the corresponding scenario in the visco-plastic threshold model, to estimate the long-term deformations.

3.7.2 Subgrade settlement

The permanent subgrade settlements were predicted with the Li-Selig model (detailed in Section 2.6.2) through the use of the empirical material parameters a, b and m. These parameter values are determined experimentally, thus, values for each layer were assumed from the collection of ranges presented in Table 2.1 from Li and Selig (1996). The empirical parameter values for the ballast and sub-ballast layers were assumed to be 0, as the permanent deformation contribution of these layers were estimated according to the methodology in Section 3.7.1 above.

The base area of the sleeper, $A = 1.25 \times 0.25$ only half the sleeper due to symmetry conditions. The maximum sleeper-ballast contact forces applied in the Li-Selig formulation was obtained from the first vehicle passage in the visco-plastic threshold model. The stratigraphy was divided into a total of 11 layers, following the layering in the chosen geometry with additional layers in the 10 m thick stabilised region and the underlaying natural clay corresponding to maximum layer interval of 2 m. Parameter values for the mass parameter unit weight γ, and the strength parameters friction angle ϕ, and cohesion c for each layer, were chosen based on engineering judgment and typical values as no specific measurements or data was available. The initial stress, the compressive strength and the deviatoric stress was calculated at the middle of each layer, subsequently the plastic strains could be obtained based on the Li-Selig formulation. The layer height and the corresponding plastic strains were used to calculate the permanent deformation contribution of each layer.

3.8 Model verification

In finite-element modelling, ensuring results and behaviour are independent from mesh discretisation and model boundaries is an integral part. In this study, the length of the model perpendicular to the track was extended until the vertical displacement at the sleeper-ballast interface converged. The longitudinal length of the model was resolved by increasing the number of preceding and subsequent sleepers around the location of interest in each analysis. Mesh convergence analysis was performed similarily by varying the assigned element sizes of each component in the FE model. Furthermore, the vertical stress distribution was verified against Boussinesq's formulation for linear elasticity.

3.8.1 FE model mesh convergence

A mesh convergence study was performed on the FE model to ensure that the calculated results of the model were independent of the mesh of the model. Since the model consists of multiple bodies with varying geometry, setting a global element size would be inefficient. This prompted the use of three initial screening runs in which the element size of each material layer was set based on the thickness of that layer. In the first run, the element sizes of each layer were set equal to the layer thicknesses but with a maximum element size of 5 m. For the second run, all element sizes were halved to allow at least two elements in height for each layer. For the third run, the sizes were changed to allow each layer to vertically consist of at least three elements. The main control parameter was the vertical displacement at the sleeper-ballast interface of the central sleeper the moment in time the first wheel of the bogie is directly above. The results of this screening are presented in figure 3.10 with triangular markers. From the second screening run to the third, the number of elements increased by a factor of 2.86, while the vertical displacement changed by 2%. To further evaluate the impact of the mesh design, especially what the response is in the gap between screening runs 2 and 3, additional runs were required.

Since higher stress and displacement gradients are expected closer to the load application, element sizes strictly based on component dimensions might not be optimal in the perspective of computational time. Components and elements will with distance from the load application have a diminishing impact on the response of the model near the load application. Further scenarios were explored with this assumption with the objective of finding an acceptable mesh design with the least amount of elements and consequently the least amount of run time. These runs are represented by circular markers in figure 3.10 where the embankment and adjacent layers were assigned smaller elements relative to those assigned for soil layers further away.

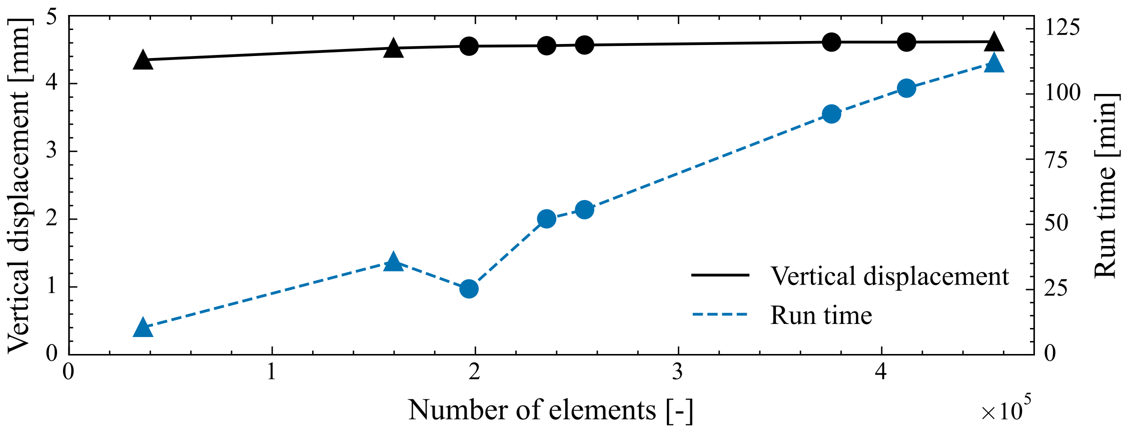

Figure 3.10: Vertical displacement at sleeper-ballast interface and runtime as a function of number of elements. Triangle markers indicate the three initial screening runs.

In subsequent runs after the first circular marker in figure 3.10, with around 200 000 elements, there is a minimal change in vertical displacement compared to the increase in number of elements signifying that the response has converged. Therefore, the mesh scenario with around 200 000 elements was selected as the finalised mesh design ensuring low run times with minimal impact on the response. The sudden decrease in run time for this design (see figure 3.10) is due to the use of a different PC compared to the rest of the runs.

3.8.2 Boussinesq and FE model comparison

In order to verify the stress distribution of the finite-element (FE) model, a comparison with Boussinesq's formulation for linear elasticity was performed. The solution of vertical stress for this formulation assumes soil as homogeneous isotropic half space. The vertical stress σ_{zz} at depth z below the load centre of a surface load p on a rigid plate with load radius a is calculated as equation 3.8 (Verruijt, 2018).

$$\sigma_{zz} = p\left(1 - \frac{z^3}{\sqrt{z^2 + a^2}^3}\right) \tag{3.8}$$

In addition to not covering multi-layered soil, Equation 3.8 also assumes vertical stress distribution to be independent of material stiffness. Thus, any stiffness variation with depth and the impact on the stress distribution this has is not captured by Boussinesq's formulation. According to Verruijt (2018) the vertical stress distribution is not susceptible to changes in stiffness unless the difference in stiffness between materials is large.

The vertical stress distribution according to Boussinesq's formulation (see equation 3.8) was calculated with a surface load equivalent to a 100 kN point load and a sleeper equivalent load radius. The same surface load configuration was used in the STEM FE model and was applied on top of the embankment. The results of these analyses are presented in Figure 3.11. Initially, within the embankment structure the difference in vertical stress and the rate at which it dissipates with depth is negligible between the two approaches. Around the depth at which the material changes from sub-ballast to fill (1.3 m) the lines diverge. Boussinesq's solution displays a smooth dissipation of vertical stress with depth at this depth, while the FE model exhibits a more drastic vertical stress change. Both approaches converge again at further depth. The discrepancy in vertical stiffness around the transition between sub-ballast and fill can be attributed to the sudden sudden change in elastic modulus from 175 MPa to 30 MPa which Boussinesq's formulation does not capture (Verruijt, 2018).

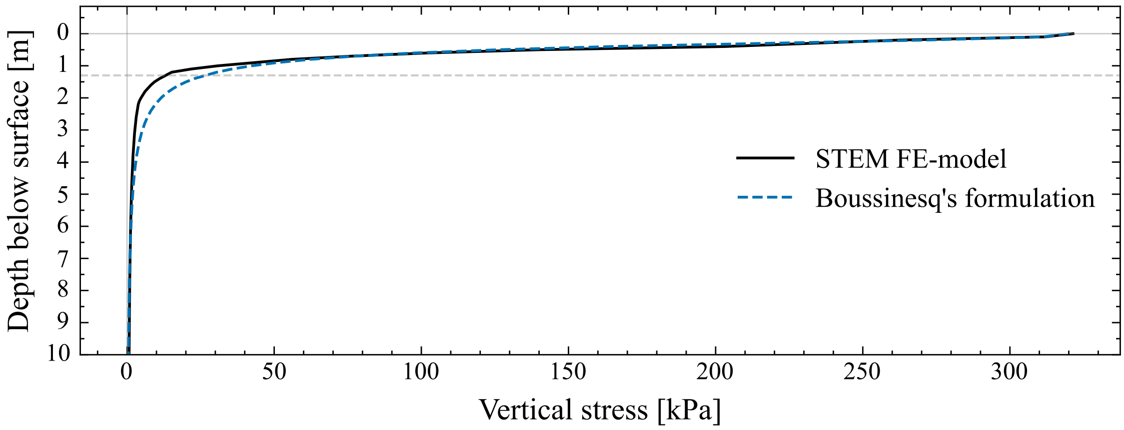

Figure 3.11: Vertical stress as a function of depth below embankment surface

3.9 Methodology for assessing parameter influence

To gauge the impact of lime-cement column input parameters on the spatial variation along the track and response of the model, multiple analyses were performed. First, the influence of material stiffness on the short-term vertical displacement was estimated with fractional factorial design. This was followed by an investigation into how horizontal and vertical scale of fluctuation of lime-cement column (LCC) stiffness affects the spatial variability in substructure stiffness along the track. Finally, by using fractional factorial design, LCC input parameters that were deemed to influence the spatial variation in settlements along the track was evaluated. Fractional factorial design was implemented with the Python library `PyDOE`.

Using a 2^{5-1}_{V} fractional factorial design, the effect that material stiffness has on the short-term vertical displacement at the sleeper-ballast interface was investigated. The parameter levels and table of contrast used are presented in Table 3.8 and

3.9 respectively. Since the design is of resolution V, main effects are aliased with four-factor interactions, while two-factor interactions are aliased with three-factor interactions. The defining relation was $\mathbf{I}$ = ABCDE and the analyses were performed in the Block configuration. The material stiffness $E_{reinforcement}$ represents the volume averaged material stiffness and does not correspond to any specific LCC geometry. The geometry of the homogenised block was kept constant across all runs with dimensions as described in Section 3.5.1. The alias structure is presented in Table 3.10

Table 3.8: Parameter levels used in the 2_{V}^{5-1} factorial design. Level values are expressed in MPa

		Levels		
Factor	Reference	−	+	Relative range [%]
$E_{ballast}$	120	108	132	20
$E_{sub-ballast}$	175	157.5	192.5	20
E_{fill}	30	27	33	20
$E_{reinforcement}$	18	16.2	19.8	20
E_{clay}	5	4.5	5.5	20

.

Table 3.9: Contrast table of the 2_{V}^{5-1} factorial design.

	A	B	C	D	E = ABCD
Run	$E_{ballast}$	$E_{sub-ballast}$	E_{fill}	$E_{reinforcement}$	E_{clay}
1	−	−	−	−	+
2	−	−	−	+	−
3	−	−	+	−	−
4	−	−	+	+	+
5	−	+	−	−	−
6	−	+	−	+	+
7	−	+	+	−	+
8	−	+	+	+	−
9	+	−	−	−	−
10	+	−	−	+	+
11	+	−	+	−	+
12	+	−	+	+	−
13	+	+	−	−	+
14	+	+	−	+	−
15	+	+	+	−	−
16	+	+	+	+	+

Table 3.10: Alias structure for the 2^{5-1}_{V} factorial design with $\mathbf{I}$ = ABCDE

A = BCDE	AB = CDE
B = ACDE	AC = BDE
C = ABDE	AD = BCE
D = ABCE	AE = BCD
E = ABCD	BC = ADE
	BD = ACE
	BE = ACD
	CD = ABE
	CE = ABD
	DE = ABC

In order to assess how the scale of fluctuation within a larger range influences the substructure stiffness distribution along the track, nine different scales of fluctuation between 0.5 – 6 m was applied in the horizontal and vertical direction respectively with the Block configuration. The geometry of the homogenised block was kept constant for all analyses with dimensions as described in Section 3.5.1. While one scale of fluctuation was varied, the other one was kept constant at 1.5 m. The coefficient of variation, wavelength and normalised mean squared successive difference of equivalent substructure stiffness along the track were acquired for each analysis. The coefficient of variation was calculated according to Equation 2.25. The normalised mean squared successive difference in stiffness was calculated by dividing MSSD (Equation 2.31) by the variance s^2 (Equation 2.26). Wavelengths in substructure stiffness was estimated by utilising experimental semivariograms where the semivariance was calculated according to Equation 2.28. Since fluctuations is of interest, the values of stiffness were detrended before calculating the semivariance. The experimental semivariance was fitted with a function based on the dampened hole-effect model (see Equation 2.30), but with the addition of a second hole-effect component. This function was fitted using the `curve_fit` function from the Python library `SciPy` and was defined as in Equation 3.9. The estimated wavelengths were interpreted as the lag distance h at which the first trough in the fitted curve occurs.

$$\begin{aligned}\gamma(h) = c_0 + c_{n,1} \times &\left[1 - \exp\left(\frac{-3h}{d_1}\right)\cos\left(\frac{h}{a_{n,1}}\pi\right)\right] \\ +c_{n,2} \times &\left[1 - \exp\left(\frac{-3h}{d_2}\right)\cos\left(\frac{h}{a_{n,2}}\pi\right)\right]\end{aligned} \tag{3.9}$$

Furthermore, LCC properties that could affect spatial variability stiffness, and their influence on long-term vertical settlements, were estimated with a 2^{4-1}_{IV} fractional factorial design. The parameters investigated, related to the random field generation, were the horizontal scale of fluctuation ($\theta_{x,z}$), the vertical scale of fluctuation (θ_y), and the coefficient of variation (CV_{LCC}). The coefficient of variation used for the random field generation will from here on be denoted as CV_{LCC} to avoid confusion with the coefficient of variation of settlement along the track. Furthermore, the longitudinal centre-to-centre spacing of lime-cement columns (ctc_z) was also investigated. The same fractional factorial design with the same parameters and levels was applied to the Block and Wall configuration. The parameter levels are presented in Table 3.11 and the responses were three variation metrics for the accumulated settlement along the track; coefficient of variation (CV), estimated wavelength and normalised successive mean squared successive difference ($MSSD/s^2$). These three metrics were retrieved in the same way as described in the paragraph above.

Table 3.11: Parameter levels used in the 2^{4-1}_{IV} factorial designs.

		Levels		
Factor	Unit	$-$	$+$	Relative range [%]
$\theta_{x,z}$	m	2.25	3.75	50
CV_{LCC}	-	0.2	0.3	40
ctc_z	m	1.36	2.04	40
θ_y	m	1.5	2.5	50

In the Block configuration, ctc_z does not alter any geometry but introduces a change in the share of volume consisting of LC-columns through $\Omega_{columns}$. Therefore, an adjustment of ctc_z in the Block configuration only establishes a change in the volume averaged elasticity modulus according to Equation 3.5 in Section 3.5.1. This elasticity modulus which was subsequently used in the generation of the random field and exclusively altered the magnitude of stiffness in the reinforcement volume. In contrast to this, in the Wall configuration, ctc_z does not affect the stiffness of the volume averaged walls. Here, the longitudinal centre-to-centre spacing of LC-columns constitutes a geometrical change in the reinforcement layer by altering the spacing between the walls without affecting material properties.

The 2^{4-1}_{IV} fractional factorial design used is of resolution IV meaning that main effects are aliased with three-factor interactions, and two-factor interactions are aliased with other two-factor interactions. Under the assumption that high-order interactions are negligible, the main effects are interpretable. The contrast table of the analyses in the Block and Wall configuration are presented in Table 3.12. The defining relation was $\mathbf{I}$ = ABCD, producing the alias structure in Table 3.13.

Table 3.12: Contrast table of the 2^{4-1}_{IV} factorial designs.

	A	B	C	D = ABC
Run	θ_{xz}	CV_{LCC}	ctc_z	θ_y
1	−	−	−	−
2	−	−	+	+
3	−	+	−	+
4	−	+	+	−
5	+	−	−	+
6	+	−	+	−
7	+	+	−	−
8	+	+	+	+

Table 3.13: Alias structure for the 2^{4-1}_{IV} factorial design with $\mathbf{I}$ = ABCD

A = BCD	AB = CD
B = ACD	AC = BD
C = ABD	AD = BC
D = ABC	

3.10 Overview of the investigated scenarios

Various scenarios were analysed using the FE model, which were solved in the time domain and capture the short-term response of a single vehicle passage. The scenarios consist of different settings regarding reinforcement type, random field and load type. The reinforcement scenarios are described in Section 3.5.1, while the random fields are defined in Table 3.7 described in Section 3.5.2. Two different loading scenarios were considered in the short-term analyses, either the single bogie vehicle (Section 3.2) or according to the methodology described in Section 3.4.2 where static point loads were applied to obtain the equivalent stiffness response of the soil model. The long-term analyses were subsequently performed using the obtained equivalent stiffness in the corresponding long-term scenario. A summary of the investigated scenarios is presented in Table 3.14, where the Reference consists of the embankment and stratigraphy without any implemented stabilisation. The Column scenario was exclusively analysed in the short-term for a single vehicle passage due to computational complexity and cost while allowing comparison between individual columns configuration and the alternative approaches of Block and Wall in the short-term response.

Table 3.14: Analysed short-term and long-term scenarios with correspond reinforcement type and random field

			Short-term		Long-term
Name	Reinforcement	Random field	Vehicle	Eq. Stiffness	Vehicle
Reference	None	None	Y	Y	Y
Column	Column	None	Y	N	N
Block	Block	None	Y	Y	Y
Wall	Wall	None	Y	Y	Y
Block I	Block	I	N	Y	Y
Block II	Block	II	N	Y	Y
Block III	Block	III	N	Y	Y
Block IV	Block	IV	N	Y	Y
Block V	Block	V	N	Y	Y
Wall I	Wall	I	N	Y	Y
Wall II	Wall	II	N	Y	Y
Wall III	Wall	III	N	Y	Y
Wall IV	Wall	IV	N	Y	Y
Wall V	Wall	V	N	Y	Y

The analyses used to assess the influence of parameters on the substructure stiffness and settlement response was previously presented in Section 3.9.

4 Numerical results

In this chapter, the numerical results corresponding to both short-term and long-term responses are presented and discussed. The performance of the developed numerical framework is evaluated under different scenarios, and the obtained results are analysed accordingly. Furthermore, the influence of varying key parameters is systematically investigated using a factorial design approach, allowing the significance of different parameters and their interaction effects to be assessed at multiple levels.

4.1 Short-term analysis

In this section, different short-term responses i.e., a single vehicle passage, are investigated, including track receptance, vertical track stiffness at the rail and ballast levels, wheel-rail contact forces, sleeper-ballast contact forces, sleeper displacements, displacements in the ballast and underlying soil layers, stress and strain distribution in depth.

4.1.1 Track receptance and frequency dependency

A vertical harmonic excitation covering the frequency range from 0 to 500 Hz is applied at the central rail seat (rail seat 41 of 81). The system response is quantified as the receptance, defined as the displacement-to-force ratio, and is evaluated at the same degree of freedom (DOF) where the load is introduced. Figure 4.1 shows the direct receptance obtained for the three analysed configurations: Reference, Block and Wall.

At 60–75 Hz a resonance frequency can be observed, this range is associated with the in-phase vibration of the rail and sleepers. A second resonance frequency appears near 315 Hz and corresponds to out-of-phase motion between these components. For reinforced configurations, the first peak is shifted towards higher frequencies with lower magnitude compared to the Reference case. The differences arise due to the increased stiffness of the supporting structure.

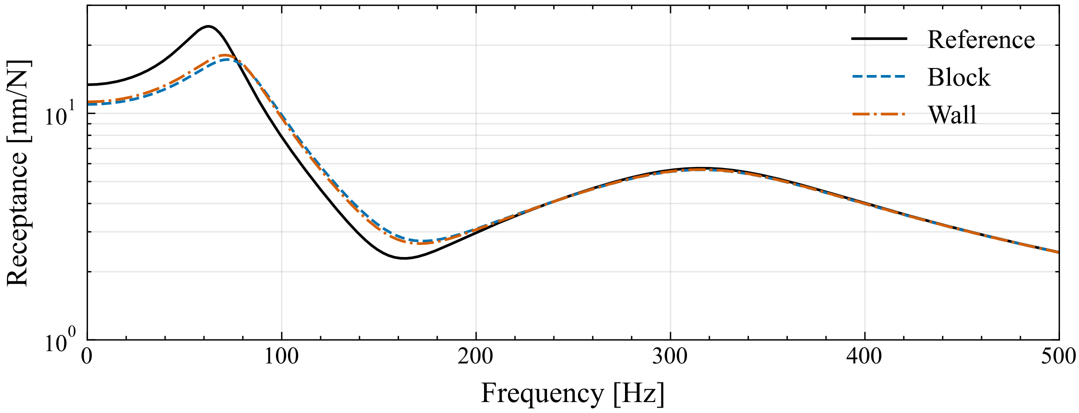

Figure 4.1: Magnitude of the direct receptance calculated for the 2D model. The excitation and the response are calculated at the middle rail seat.

4.1.2 Static track stiffness at the rail level and ballast level

The static stiffness of the track system is evaluated at both the rail level and the ballast level for the investigated base configurations. The presented stiffness values are derived from the global stiffness matrices of the numerical track model. Figure 4.2a presents the vertical track stiffness, while Figure 4.2b shows the equivalent static substructure stiffness.

The reinforced configurations exhibit higher stiffness than the Reference case at both evaluation levels. The Block configuration provides the highest stiffness, followed by the Wall configuration. In addition, the stiffness obtained at the ballast level is consistently lower than at the rail level for all configurations due to the comparatively compliant behaviour of the ballast and subgrade relative to the much stiffer rail and sleeper components. The stiffness remains nearly uniform along the rail seats and sleeper positions for the various cases, although some periodic pattern is observed at the rail level due to the discrete rail support.

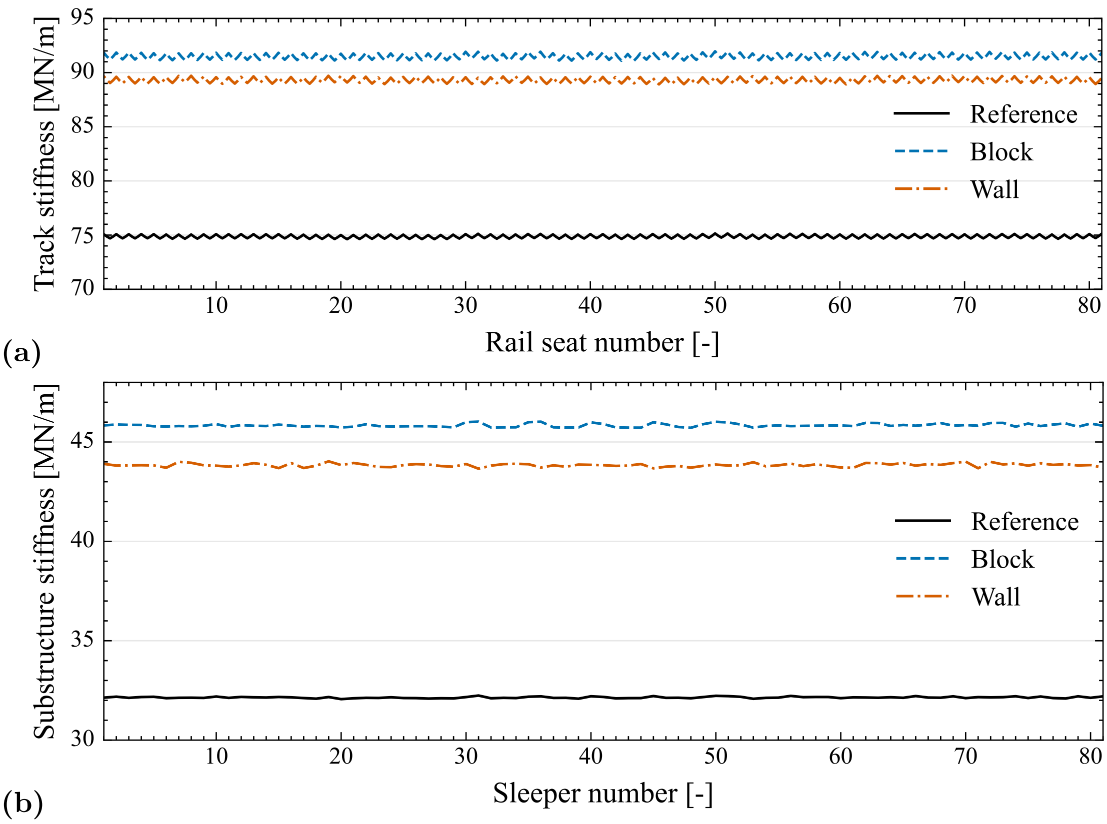

Figure 4.2: Comparison of (a) the static track stiffness at rail level and (b) the equivalent substructure stiffness for the investigated base scenarios.

4.1.3 Elastic deformation within different soil layers

In this section, the vertical elastic deformation response of the track and supporting soil layers is investigated for different scenarios. The results are presented as vertical displacement below the middle sleeper as a function of time, at different depths below the same sleeper, and perpendicular to the track centreline.

Figure 4.3 presents the vertical displacement at the sleeper-ballast interface below the middle sleeper (41st out of 81) during a single vehicle passage. The Reference scenario exhibits the largest vertical deformations, with peak displacements of approximately 4.8 mm, whereas the reinforced configurations show reduced deformation due to the increased stiffness of the soil system. The reinforced cases show a similar order of magnitude, with peak displacements ranging between approximately 3–3.4 mm. Furthermore, in all investigated cases, the individual wheel passages are not clearly distinguishable in the displacement response since the soft track system does not fully recover between consecutive wheel passages.

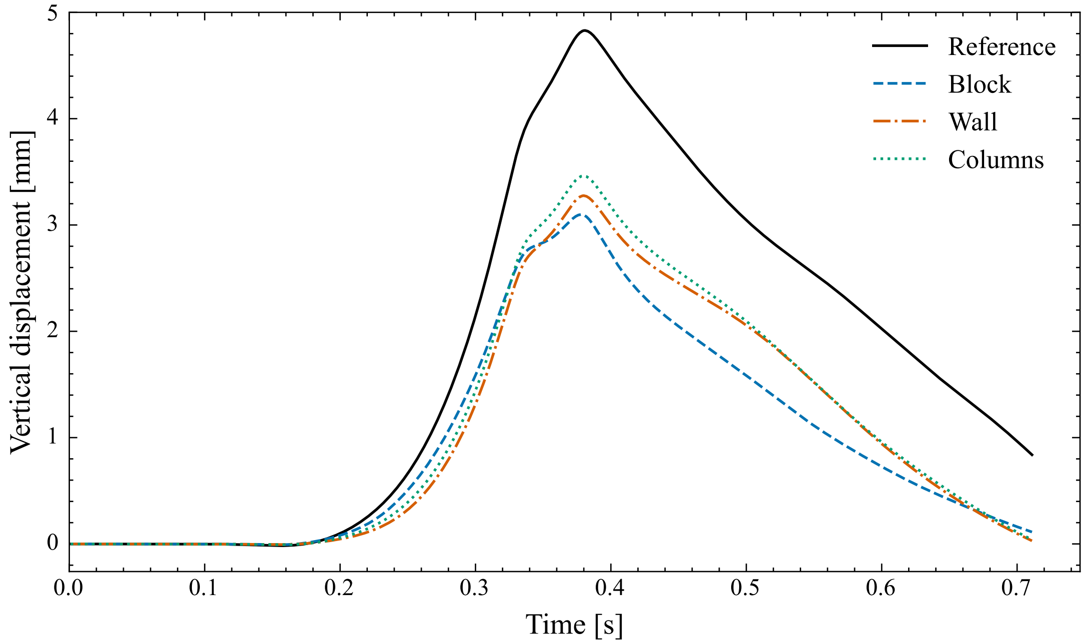

Figure 4.3: Vertical displacement at the sleeper-ballast interface as a function of driving distance for the Reference case without reinforcement and the three reinforcement modelling approaches: Column, Wall, and Block.

Figure 4.4 presents the time history of vertical displacements at different depths below the middle sleeper during a vehicle passage for the Reference configuration. Larger deformations are observed closer to the load application, while the displacement amplitudes decrease with increasing depth due to stress attenuation and the load distribution within the soil. In addition, the response become wider with depth because of increased flexibility and spread of stresses in the deeper soil layers.

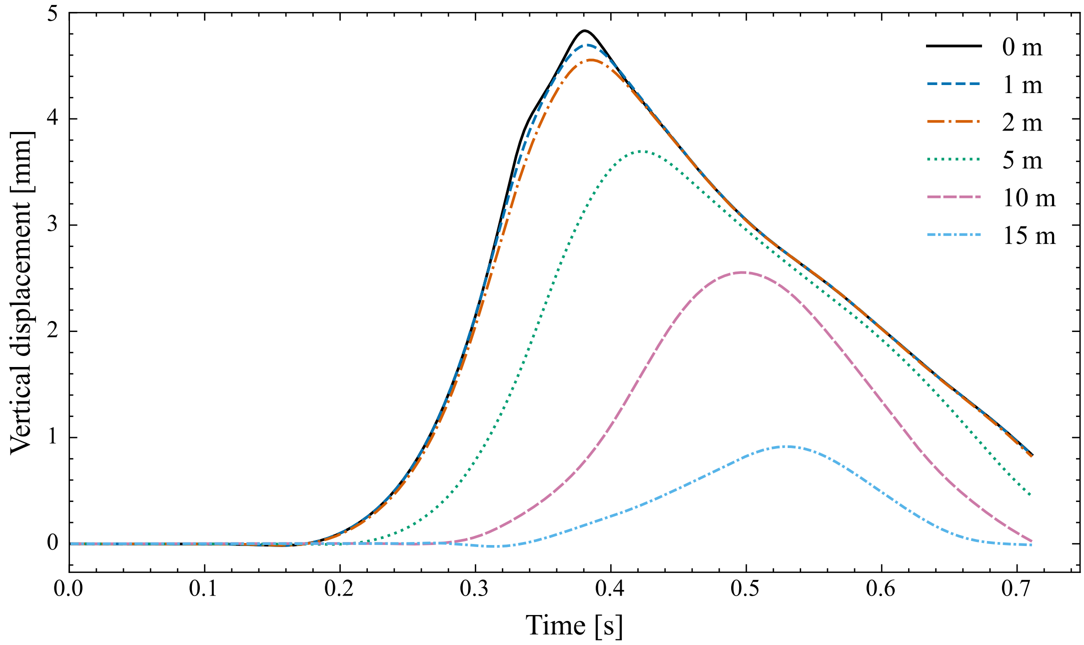

Figure 4.4: Vertical displacement within different depths below the middle sleeper

Figure 4.5 presents the vertical displacement along the fill-reinforcement interface, perpendicular to the track direction when the leading wheel is positioned above the middle sleeper. All scenarios exhibit the largest deformation below the track centreline, followed by a gradual reduction with increasing distance from the load application point. The reinforced configurations show reduced deformation levels compared to the Reference case due to the increased stiffness of the supporting system, additionally, the Column configuration displays a periodic pattern mirroring the individual columns and their spacing. At approximately 5.7 m from the symmetry line, all scenarios show a faster decrease in vertical displacement. This change in response corresponds to the edge of the embankment/fill, indicating that the deformations are mainly confined within the embankment region.

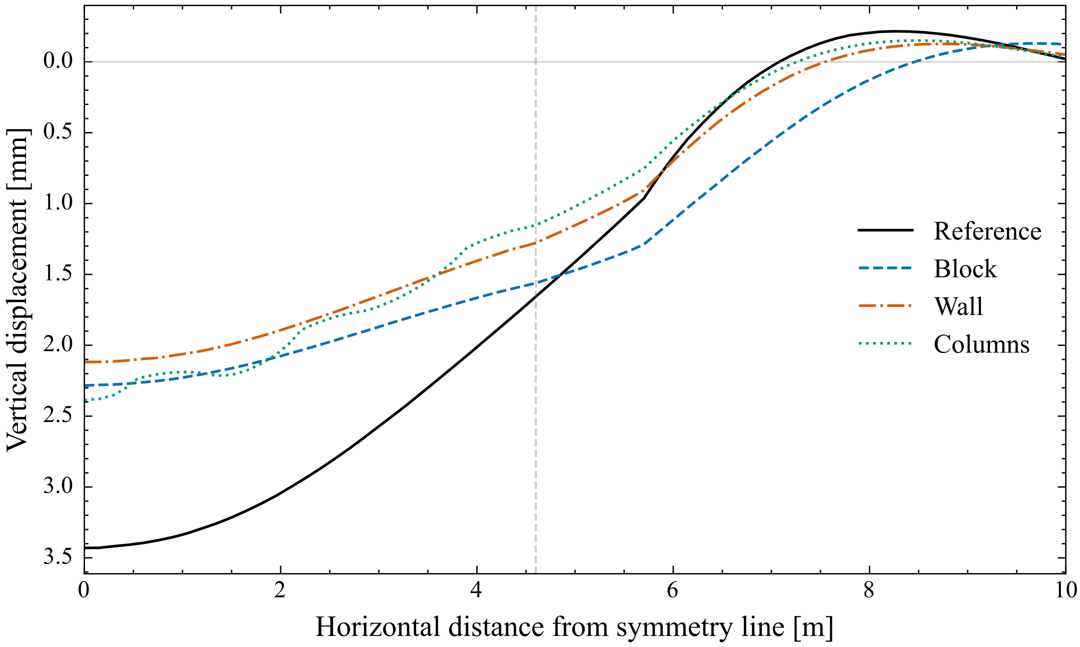

Figure 4.5: Vertical displacement along the top boundary of the reinforcement area, perpendicular to the track. The vertical dashed gray line represents the horizontal boundary of the reinforcement area.

4.1.4 Vertical contact forces at the wheel-rail and sleeper-ballast interface

The contact forces are evaluated at both the wheel-rail interface and the sleeper-ballast interface after a single vehicle passage for the three base scenarios: Reference, Block and Wall. Figure 4.6a shows the vertical wheel-rail contact forces, while Figure 4.6b presents the contact forces at the sleeper-ballast interface.

Periodic oscillations can be observed in the wheel-rail contact forces for the investigated configurations due to discretised sleeper support condition, although the responses are centred around approximately 84 kN, which is close to the static wheel load calculated from the vehicle axle load of 17.1 tonnes. These results indicate a relatively small dynamic contribution compared to the quasi-static response, since there are no large stiffness gradients along the track. The reinforced scenarios exhibit slightly higher peaks due to the increased stiffness of the substructure.

Larger differences among the calculated sleeper-ballast contact forces for different configurations are observed. The reinforced scenarios exhibit higher contact forces than the Reference case, with the Block configuration displaying slightly larger values compared to the Wall scenario. The behaviour is attributed to the increased stiffness response seen in section 4.1.2 and a larger load transfer to the ballast layer. The contact forces remain nearly uniform along the track for all configurations, indicating an even load distribution from the rail to the ballast despite the reinforcement implementation. Further, this means that when the flexibility of a structure increases, the load is distributed among more sleepers, and the sleeper–ballast contact forces are reduced.

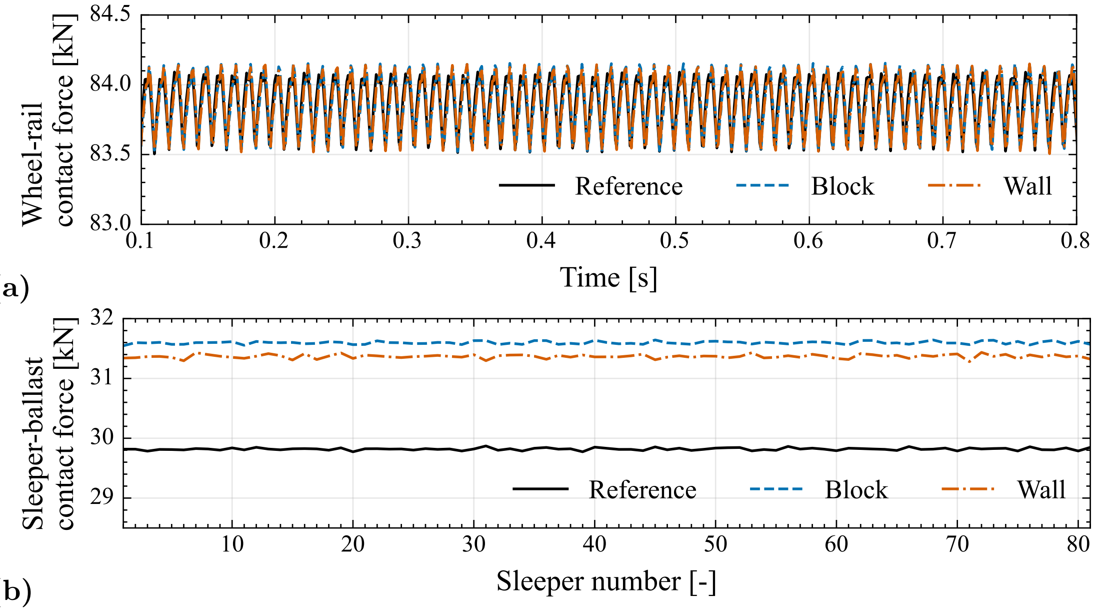

Figure 4.6: Comparison of **(a)** the vertical contact force at the wheel-rail interface and **(b)** the contact force at the sleeper-ballast interface for the investigated base scenarios.

4.1.5 Stress and strain in subsoil layers

In this section, the vertical stress and strain responses below the middle sleeper are evaluated for the investigated base scenarios. Figure 4.7 presents the vertical stress distribution with depth, while Figure 4.8 shows the corresponding vertical strain response. The results are evaluated for the time-step corresponding to when the leading wheel is positioned directly above the sleeper.

Figure 4.7 presents the vertical stress, the highest stresses are observed close to the ballast layer directly below the sleeper and subsequently decrease with depth due to load dissipation within the soil profile. The reinforced configurations exhibit slightly higher stresses within the upper reinforcement zone compared to the Reference case, indicating a stiffer response and more concentrated load transfer near the surface.

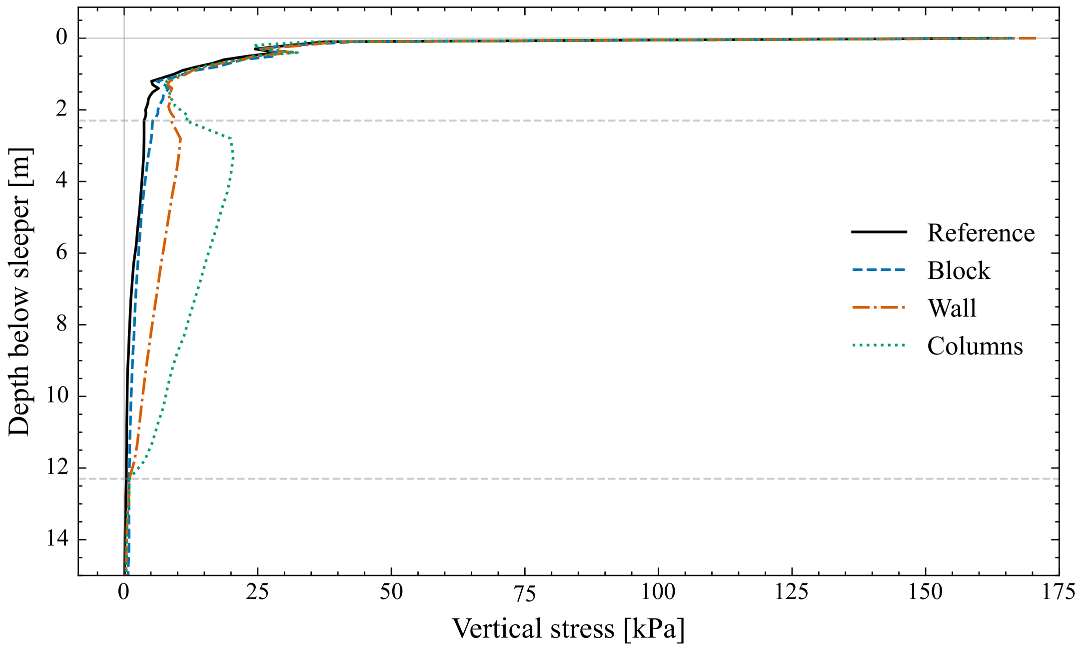

Figure 4.7: Vertical stress as a function of depth below sleeper for the four base scenarios. At the moment in time the leading wheel is directly above the sleeper. Area between two horizontal gray dashed lines represent the area where the soil has been reinforced using LCCs. It should be noted that the points for Wall and Columns pass through a reinforcement volume

Figure 4.8 shows that the Reference scenario exhibits the largest vertical strain magnitudes throughout most of the soil profile, whereas the reinforced configurations reduce the vertical strains within the reinforced region. This behaviour is consistent with the increased stiffness response observed in previous sections and indicates that the LCC reinforcement effectively limits compressive deformation in the shallow soil layers.

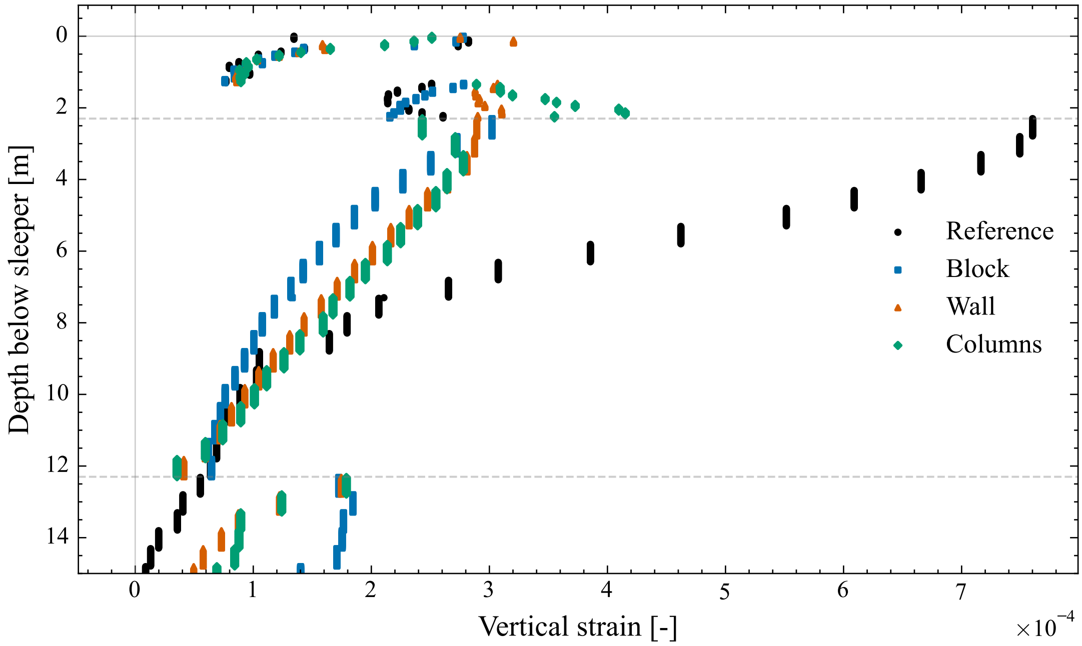

Figure 4.8: Vertical strain as a function of depth below sleeper for the four base scenarios. For the time step where the leading wheel in the bogie is positioned directly above the sleeper. Area between two horizontal gray dashed lines represent the area where the soil has been reinforced using LCCs.

4.1.6 Influence of spatial variation on vertical static track stiffness

This section investigates the influence of spatial variability in the LCC reinforcement on the vertical static track stiffness along the track alignment. The analyses include the Block and Wall base scenarios, presented in Section 4.1.2 and the random field realisations described in Section 3.5.2, with the scale of fluctuation values collected from Table 4.1. The same random-seed and coefficient of variation are adopted for all realisations such that the influence of the scale of fluctuation parameters can be evaluated independently of changes in the overall variability level or random field pattern. The objective is to evaluate the magnitude and spatial distribution of local stiffness variations caused by the stochastic LCC properties and their potential influence on differential track response.

Table 4.1: Horizontal and vertical scale of fluctuations of LCCs. collected from Wong et al. (2024)

	Ave	Min	Max	I	II	III	IV	V
θ_y [m]	1.4	0.4	3.5	Ave	Max	Min	Min	Max
$\theta_{x,z}$ [m]	1.6	0.4	4.3	Ave	Max	Min	Max	Min

Figure 4.9 presents the equivalent substructure stiffness for the Block base scenario and the five random field realisations. Compared to the base scenario, the random field cases exhibit larger stiffness variation along the track due to the spatial vari-

ability introduced in the LCC properties. Nevertheless, all configurations maintain similar overall stiffness levels, indicating that the reinforced block could provide a stable global response despite local variability.

Random field II exhibits the largest stiffness variation, with a characteristic wavelength of approximately 50 sleepers (30 m) along the track alignment. The behaviour is associated with the maximum horizontal scale of fluctuation adopted in the random field generation, resulting in extended regions of relatively stiff and soft support conditions. A similar but less pronounced trend can also be observed for random field IV, which also includes the maximum horizontal scale of fluctuation. In contrast, random fields III and V display shorter and smoother local variations due to the shorter horizontal correlation length.

Local heterogeneity ultimately affects the stiffness distribution along the track, which could contribute to differential track settlement.

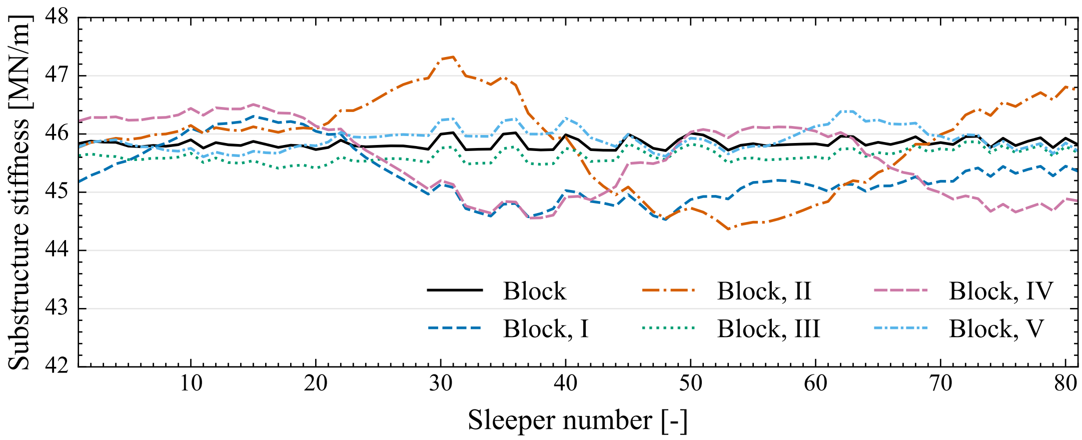

	No RF	I	II	III	IV	V
CV [%]	0.18	1.04	1.73	0.25	1.38	0.41
Range [MN/m]	0.31	1.77	2.95	0.46	1.95	0.78

Figure 4.9: Equivalent substructure stiffness for Block with base scenario and five different random field scenarios, at each sleeper in the 3D FE model

Figure 4.10 presents the equivalent substructure stiffness for the Wall base scenario and the five random field realisations. Similar to the Block configurations, the random field cases exhibit larger local stiffness variations along the track alignment compared to the base scenario. However, all configurations maintain similar overall stiffness levels, indicating that wall reinforcements provide a stable global response despite local variability caused by the implementation of walls with soft soil in between. Random field II again exhibits the largest stiffness fluctuations along the track, while random fields III and V display smoother local variations. Compared to the Block configurations, the Wall scenarios generally exhibit slightly smaller fluctuation amplitudes, suggesting a more uniform stiffness response despite stochastic variability in the LCC properties.
The equivalent vertical subgrade stiffness at the interface of sleeper and ballast

obtained in this section is used as input to an equivalent 2D model to estimate the long-term settlements of the various random field realisations, these results are presented in Section 4.2.1.

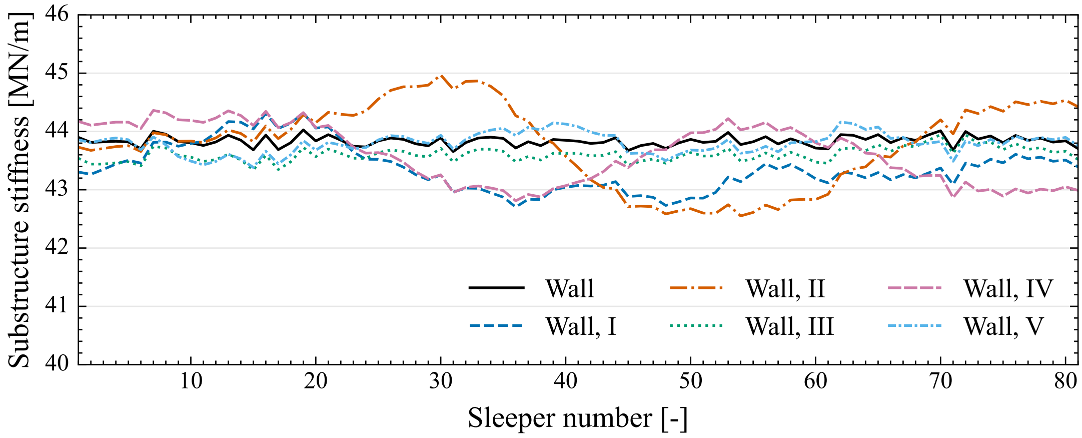

	No RF	I	II	III	IV	V
CV [%]	0.19	0.91	1.61	0.28	1.13	0.40
Range [MN/m]	0.37	1.61	2.42	0.60	1.56	0.78

Figure 4.10: Equivalent substructure stiffness for Wall with base scenario and five different random field scenarios, at each sleeper in the 3D FE model

4.2 Long-term analysis using empirical settlement model

This section presents calculated long-term settlements caused by repeated vehicle passages. The analysed scenarios are presented in Section 3.10 and correspond to the investigated base cases along with the five random field realisations for the reinforced configurations. The total accumulated settlements are evaluated as the sum of the ballast/sub-ballast deformation contribution using the visco-plastic threshold model and the subgrade deformation using the Li-Selig formulation.

4.2.1 Long-term settlements

Figure 4.11 presents the estimated long-term settlements of the ballast/sub-ballast in the upper panel, subgrade in the middle panel, and total accumulated settlements in the bottom panel for the base scenarios Reference, Block and Wall. The Block scenario exhibits the largest permanent ballast settlements followed by the Wall and Reference case. The results show relatively uniform settlements, reflecting the equivalent substructure stiffness presented in Section 4.1.2. The estimated long-term settlements are driven by the exceedance of contact force above a threshold value. The resulting contact forces presented in Section 4.1.4 show that the reinforced scenarios exhibit larger contact forces, thus moderate changes in peak force levels are shown to cause significant influence on the accumulated plastic deformation due to the nonlinearity of the formulation.

The estimated subgrade settlements follow the expected trend of increasing deformation with decreasing equivalent stiffness, where the Reference scenario retains the lowest stiffness and the largest subgrade deformation contribution. The behaviour does thereby reflect a more compliant system with reduced load transfer efficiency to deeper layers. The accumulated settlements show that the Reference scenario exhibits the largest permanent vertical displacement while the reinforced configurations obtain smaller values. The differences in the Li-Selig model for Block and Wall, which in this study does not emulate the Wall configuration properly, are due to the input parameters assigned. The results highlight the influence of the individual settlement components and suggest that the response is not governed by stiffness alone, but a combination of stiffness, dynamic amplification, and sleeper-ballast contact forces.

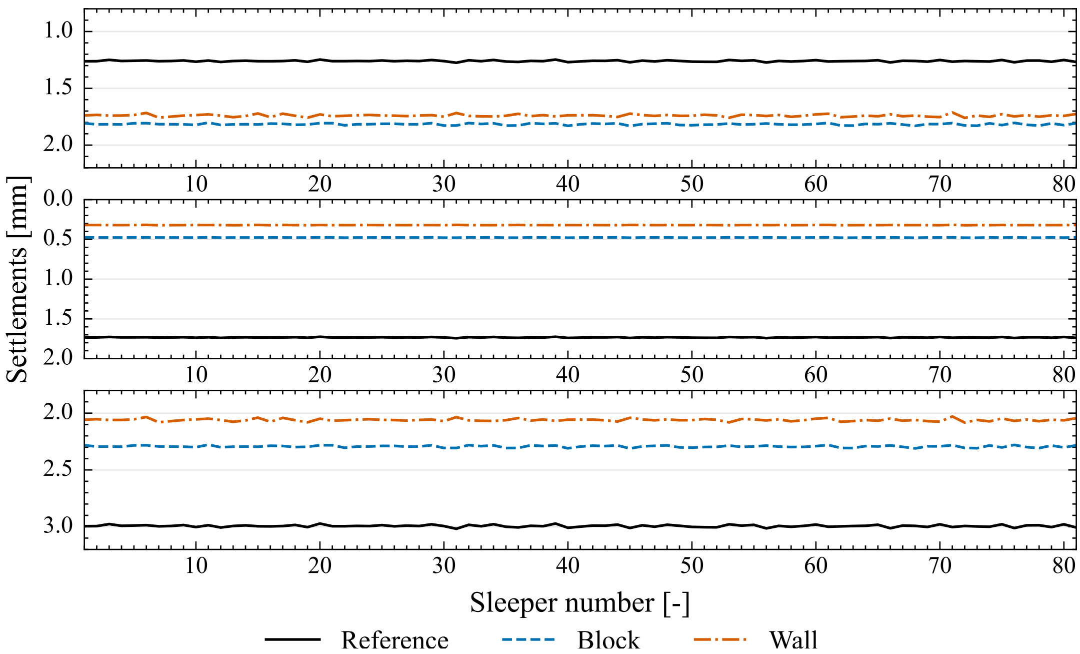

Figure 4.11: Long-term settlement of the three base scenarios without random field. Top: visco-plastic threshold model. Middle: Li-Selig model. Bottom: accumulated

Figure 4.12 presents the permanent long-term settlements estimated for the base Block scenario and the random field configurations. The upper figure shows the ballast/sub-ballast settlements obtained from the visco-plastic threshold model, the middle figure presents the subgrade settlement estimated using the Li-Selig formulation, and the lower figure illustrates the accumulated permanent settlements. Accumulated settlement variations can be observed for all random field configurations, although random field II and IV displays the largest fluctuations, which is consistent with the stiffness distribution obtained in prior results. As shown in the top and middle panels, the variation is primarily governed by the ballast settlements whereas the subgrade deformation fluctuates within a closer range. The results for substructure stiffness with the Block configuration in Figure 4.9, Section 4.1.6 in comparison with the accumulated settlements in Figure 4.12 suggests that a sleeper

with large support stiffness will settle more than one supported by a softer substructure within the same analysis. This can be attributed to the increased contact force that greater stiffness generates.
The results show that the spatial variability of LCC properties results in differential settlements, which may eventually require maintenance to retain fully operational track conditions.

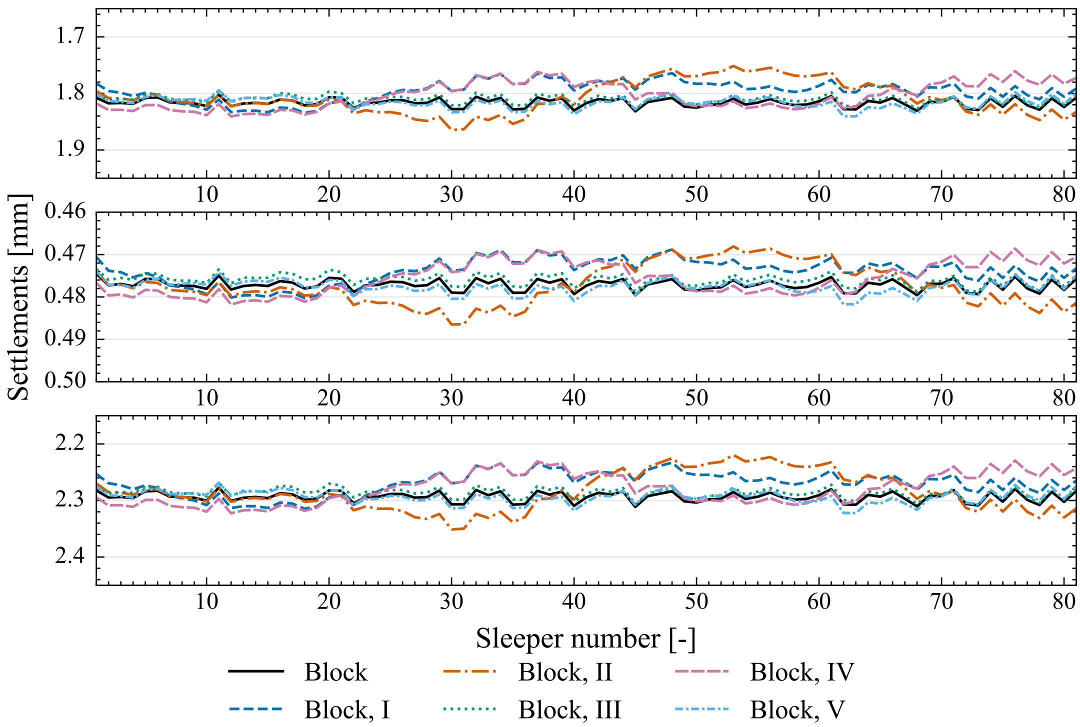

	No RF	I	II	III	IV	V
CV [%]	0.54	0.94	1.48	0.57	1.09	0.62
Range [mm]	0.054	0.092	0.115	0.059	0.099	0.065

Figure 4.12: Long-term settlement of the block scenario with different random field configurations. Top: visco-plastic threshold model. Middle: Li-Selig model, Bottom: accumulated

Figure 4.13 shows the long-term settlements for the investigated Wall configurations. Compared to the Block results the wall scenarios exhibits lower general magnitudes while also displaying marginally larger ranges. The random field realisations II and IV follow the same trend as the corresponding Block scenarios with higher fluctuations in accumulated stiffness compared to the other generations. Much like the results for the Block configurations, differential settlements are obtained and the primary contribution stem from the ballast settlements while the reinforcement significantly reduces the subgrade settlements as shown in Figure 4.11.

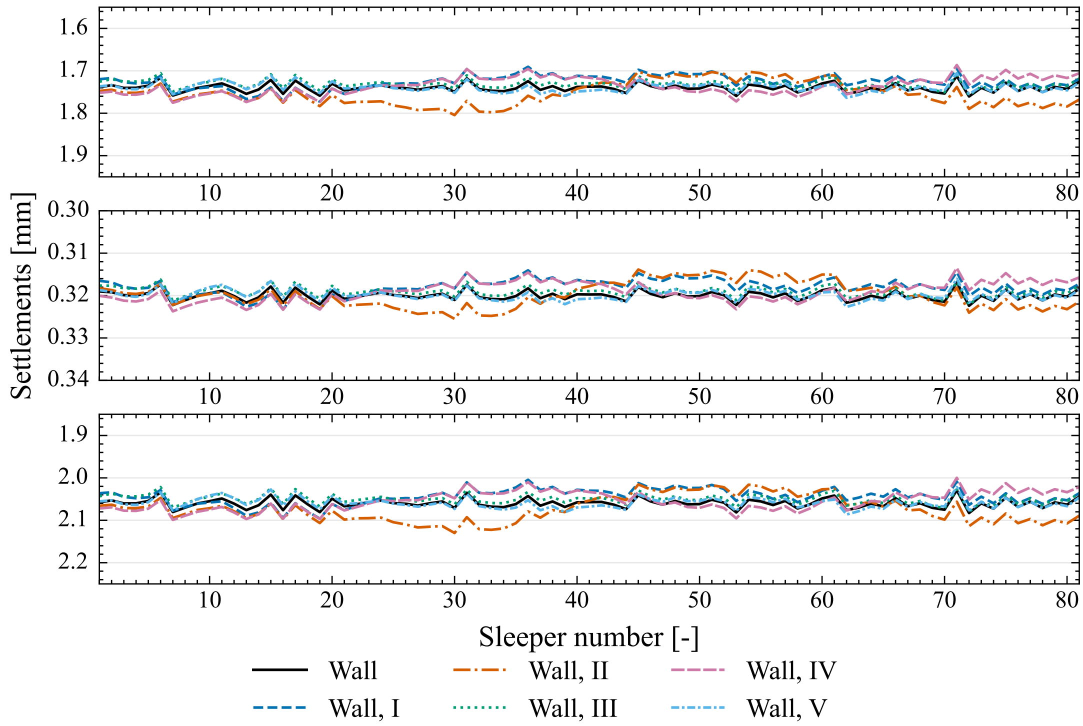

	No RF	I	II	III	IV	V
CV [%]	0.53	0.91	1.45	0.56	1.07	0.61
Range [mm]	0.056	0.096	0.120	0.061	0.104	0.068

Figure 4.13: Long-term settlement of the wall scenario with different random field configurations. Top: visco-plastic threshold model. Middle: Li-Selig model. Bottom: accumulated

4.3 Sensitivity analysis

This section presents the results of analyses that were performed to assess the influence of lime-cement column input parameters on the spatial variation in substructure stiffness and deformation along the track.

4.3.1 Temporal effects of stiffness of different layers on sleeper displacement

In Figure 4.14, the estimated main and two-factor interaction effects of material stiffnesses on the vertical displacement at the sleeper-ballast interface from the 2^{5-1}_{V} factorial design are presented. The factors and their levels assigned are presented in Table 4.2

Table 4.2: Parameter levels used in the 2_{V}^{5-1} factorial design. Level values are expressed in MPa

Factor		Reference	Levels		
			$-$	$+$	Relative range [%]
A	$E_{ballast}$	120	108	132	20
B	$E_{sub-ballast}$	175	157.5	192.5	20
C	E_{fill}	30	27	33	20
D	$E_{reinforcement}$	18	16.2	19.8	20
E	E_{clay}	5	4.5	5.5	20

In Figure 4.14, factor D ($E_{reinforcement}$) exhibits the largest estimated main effect on the vertical displacement response at the sleeper-ballast interface. Meanwhile, the stiffnesses of ballast (A), sub-ballast (B), fill (C) and subgrade (E) display less influence on the displacement response. By observing the stress distribution presented in Figure 4.7, a greater effect from material stiffness closer to the load application is expected, due to the high stress magnitude. This is not observed and is most likely related to the relative thicknesses of the materials analysed. The thickness of the reinforcement layer greatly exceeds those of the ballast, sub-ballast and fill, resulting in a greater cumulative contribution to displacement. Consequently, a relatively small difference in strain over a large thickness may produce larger total displacements than a greater difference in strain over a thinner layer. The effects should therefore only be interpreted as a result of the specific embankment and reinforcement design applied in this study.

The magnitude of the two-factor interaction effects in Figure 4.14 suggests that the vertical displacement response is primarily governed by independent main effects within the investigated factor ranges and behaves approximately additively. The two-factor interaction effects are negligible in comparison to their main counterparts. The negligible two-factor interactions and the dominant main effect of $E_{reinforcement}$ suggests that efforts related to reinforcement stiffness may have greater impact on the vertical displacement response than comparable efforts applied to any of the other stiffness parameters.

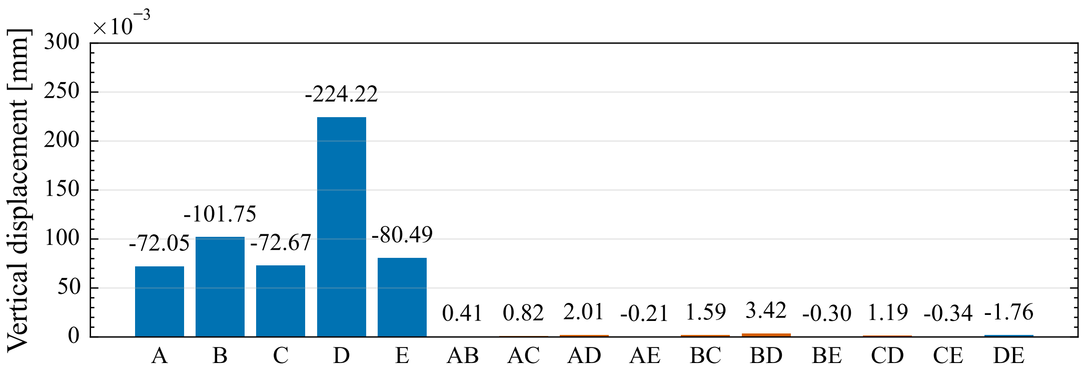

Figure 4.14: The effect on vertical displacement at the sleeper-ballast interface by different material stiffnesses. Positive and negative effects are indicated by orange and blue colour, respectively

4.3.2 Response of horizontal and vertical scale of fluctuation

Equivalent static vertical stiffness for each sleeper obtained for different scales of horizontal fluctuation ($\theta_{x,z}$) with θ_y kept at 1.5 m, is presented in Figure 4.15. With $\theta_{x,z}$ at 0.5 m, there are small fluctuations in the stiffness response. Every increase in $\theta_{x,z}$ causes an increase in fluctuations, both in amplitude and in longitudinal distance. This further strengthens the previous conclusion that higher horizontal scale of fluctuation results in larger fluctuations in the substructure stiffness along the track. Interestingly, sections of track with longer periods of close to static stiffness can be observed for the analyses with higher horizontal scale of fluctuation. In Figure 4.15, the 4.0 m, 5.0 m and 6.0 m curves exhibit such behaviour resembling trapezoidal waveforms, characterised by plateaus as extrema and near-linear ramps.

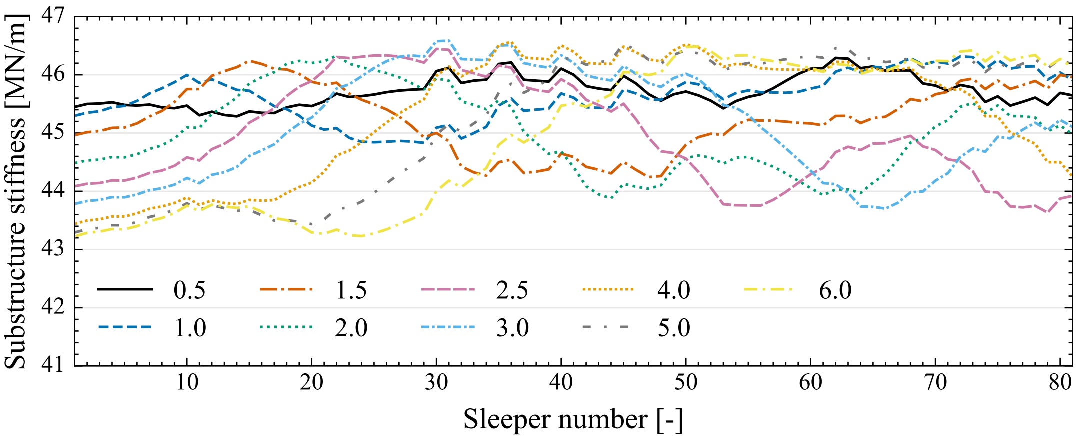

Figure 4.15: Equivalent substructure stiffness for different sizes of horizontal scale of fluctuation at each sleeper in the 3D FE model

Coefficient of variation (CV), wavelength (λ) and normalised mean squared successive difference (MSSD/s^2) of the substructure stiffness as a result of different horizontal scale of fluctuations are presented in Figure 4.16. From Figure 4.16a it can be concluded that with a vertical scale of fluctuation constant at 1.5 m, the CV of substructure stiffness changes approximately linearly within the analysed range of horizontal scale of fluctuation. Similarily the normalised mean squared successive difference in Figure 4.16c, although not linear, shows a trend with increasing $\theta_{x,z}$. MSSD/s^2 decreases with $\theta_{x,z}$ indicating that the relative difference in stiffness at each consecutive sleeper position compared to the total variation decreases as well and goes toward zero.

The semivariograms with fitted curves used to determine the wavelength in the substructure stiffness are presented in Appendix C.1. Some of the analyses proved to have multiple periods where the smallest period of these is represented by a square marker in Figure 4.16b. With the exception of $\theta_{x,z} \leq 1.0$ m, the determined wavelengths are dispersed in the range of 30 – 42 m. Furthermore, the second period of the analyses with multiple wavelengths (square markers) are also confined in this range (see Appendix C.1). Since the Block configuration is analysed, there are no geometrical periodicities that could impose this wavelength range.

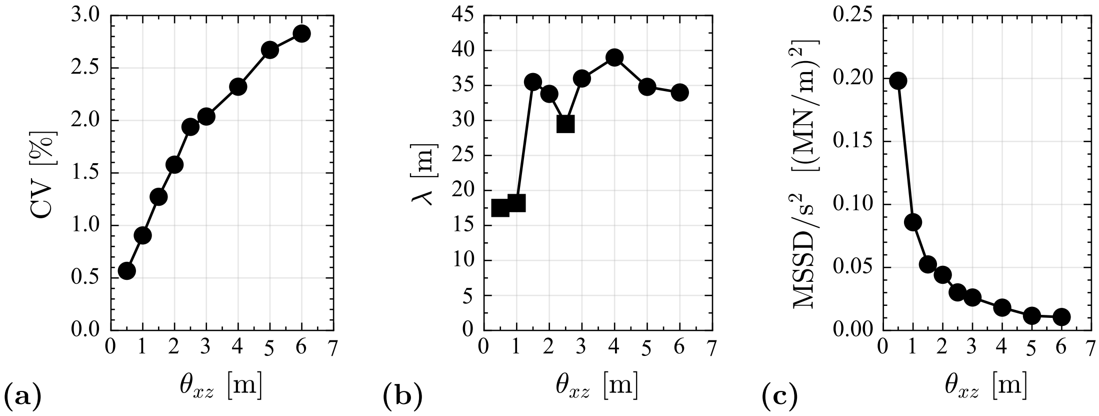

Figure 4.16: Metrics for the distribution of substructure stiffness for the different sizes of horizontal scale of fluctuation. **(a)** Coefficient of variation of substructure stiffness as a function of $\theta_{x,z}$ **(b)** Wavelength of substructure stiffness as a function of $\theta_{x,z}$, square markers represent shortest wavelength if there were multiple **(c)** Normalised mean squared successive difference of substructure stiffness as a function of $\theta_{x,z}$

Figure 4.17 shows the equivalent static vertical substructure stiffness for each sleeper obtained with different vertical scale of fluctuation (θ_y) while $\theta_{x,z} = 1.5$ m. Unlike $\theta_{x,z}$ in Figure 4.15, a change in θ_y does not introduce an easily observable periodicity in the vertical stiffness distribution along the track. The vertical stiffness for vertical scale of fluctuation 1.0 m , 2.5 m and 3.0 m all fluctuate within a similar magnitude of range. Furthermore, above sleeper number 30, vertical stiffness for $\theta_y = 0.5$ m and 2.0m are conjoined. The larger assigned values for θ_y exhibit larger ranges in vertical stiffness across the track extent but with no clear periodicity. For example for $\theta_y = 6.0$ m, from sleeper 1 to 50, the vertical stiffness follows a downwards trend with some fluctuations but then transitions into an approximately sinusoidal stiffness distribution above sleeper 50.

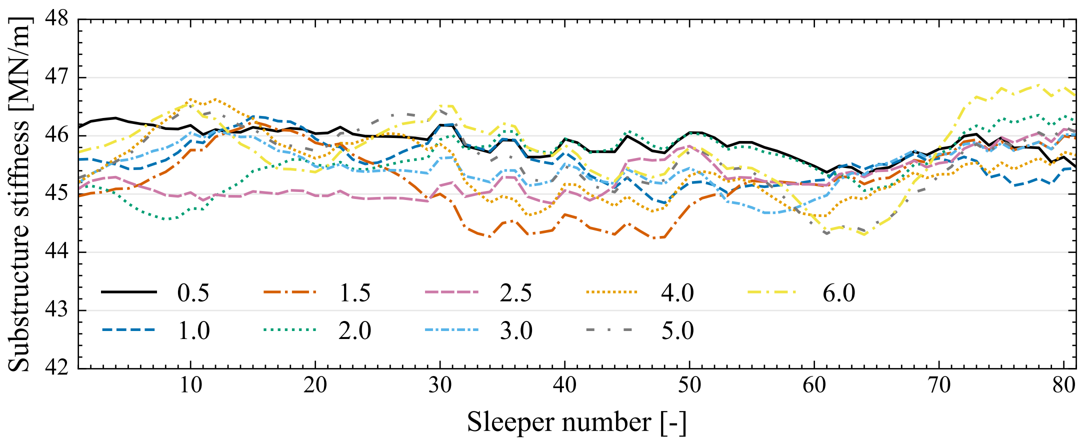

Figure 4.17: Equivalent substructure stiffness for different sizes of vertical scale of fluctuation at each sleeper in the 3D FE model

Coefficient of variation (CV), wavelength (λ) and normalised mean squared successive difference (MSSD/s^2) of the substructure stiffness as a result of different vertical scale of fluctuations are presented in Figure 4.18. In Figure 4.18a, showing the coefficient of variation in the substructure stiffness along the track for the analysed vertical scales of fluctuation, the approximately linear behaviour exhibited by different $\theta_{x,z}$ is not observed. Instead, CV increases rapidly until $\theta_y = 1.5$ m and then declines until the scale doubles, followed by a rapid gain again. One thing to note is that the maximum CV observed by varying θ_y is approximately half of the corresponding coefficient acquired by varying $\theta_{x,z}$ with the same set of values. The almost identical CV when $\theta_y = 1.0$ m, 2.5 m, and 3.0 m is in accordance with the previous observation that these share similar dispersion and fluctuation. This is also evident by the normalised mean squared successive difference of the substructure stiffness presented in Figure 4.18c where MSSD/s^2 for these three scenarios are similar. The resulting CV and MSSD/s^2, in Figure 4.18a and 4.18c respectively, show with vertical scale of fluctuation from 4 m and above some resemblance to the linear response as in the corresponding Figures 4.16a and 4.18c for θ_y, however, at quite different magnitudes. The variance, s^2, is used in the calculation of both metrics and the dispersion is generally smaller than for $\theta_{x,z}$, thus CV will be smaller while it will have the opposite effect on MSSD/s^2. A large MSSD/s^2 represents larger differences in stiffness from consecutive sleepers compared to the total variance.

The estimated substructure stiffness wavelengths for different θ_y are shown in Figure 4.18b. Some semivariograms displayed several periods across the analysed track length and this behaviour was more prevalent with θ_y than for $\theta_{x,z}$ (see Appendix C.2). The smallest estimated wavelengths out of these are represented by a square marker in Figure 4.18b. In contrast to the semivariograms obtained from varying $\theta_{x,z}$, the semivariance for different θ_y was substantially lower but with quite similar wavelengths. This suggests that the contrast in substructure stiffness is much smaller over the same spatial scale along the track.

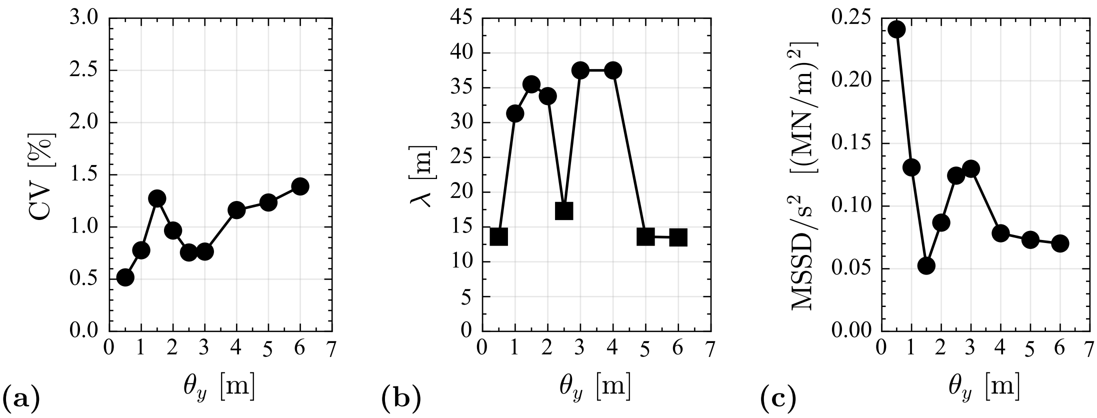

Figure 4.18: Metrics for the distribution of substructure stiffness for the different sizes of vertical scale of fluctuation. **(a)** Coefficient of variation of substructure stiffness as a function of θ_y **(b)** Wavelength of substructure stiffness as a function of θ_y, square markers represent shortest wavelength if there were multiple **(c)** Normalised mean squared successive difference of substructure stiffness as a function of θ_y

With increasing horizontal scale of fluctuation, the coefficient of variation and normalised mean squared successive difference of the substructure stiffness were linear increasing and monotically non-increasing respectively, within the analysed value range and track length. When varying the vertical scale of fluctuation, this was not observed. Furthermore, higher CV and lower MSSD/s^2 observed with increasing $\theta_{x,z}$ suggests larger fluctuations in substructure stiffness along the track compared to increasing θ_y. This was also corroborated by the magnitude difference in semivariance between the two scenarios. Within the analysed range, and by keeping the other direction at 1.5 m, the horizontal scale of fluctuation in the LCC material stiffness induces more severe fluctuations in the substructure stiffness.

4.3.3 Importance of parameters for spatial variability in accumulated permanent settlements

Using a 2^{4-1}_{IV} fractional factorial design, accumulated settlements of each sleeper and run configuration with the Block scenario are shown in Figure 4.19 together with a summary table of the variation metrics obtained for each run. The factors and their levels assigned are displayed in Table 4.3. The fitted curve semivariograms used to estimate the wavelengths of the settlement distributions are presented in Appendix D.1.

Table 4.3: Parameter levels used in the 2^{4-1}_{IV} factorial designs.

Factor		Unit	Levels		
			$-$	$+$	Relative range [%]
A	θ_{xz}	m	2.25	3.75	50
B	CV_{LCC}	[-]	0.2	0.3	40
C	ctc_z	m	1.36	2.04	40
D	θ_y	m	1.5	2.5	50

The graph in Figure 4.19 display a distinct difference in the level of settlement between even and odd run numbers. This corresponds to the contrasts of ctc_z in Table 3.12 where every even run number adopts the high level of ctc_z and the reverse for every odd run number. Furthermore, another direct observation is that CV are large for runs 1, 4, 6, 7 which coincides with the low level of θ_y.

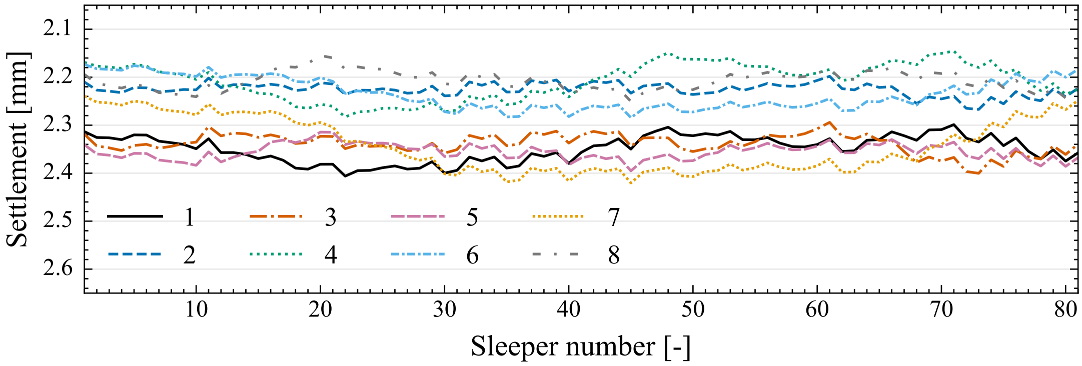

	1	2	3	4	5	6	7	8
CV [%]	1.17	0.61	0.88	1.71	0.70	1.47	2.43	0.91
λ [m]	38.49	13.28	13.60	37.38	21.53	43.56	43.24	22.48
MSSD/s^2 [mm^2]	0.28	0.89	0.51	0.12	0.76	0.15	0.07	0.42

Figure 4.19: Accumulated long-term settlement and metrics for its variation from the 2^{4-1}_{IV} factorial with the Block configuration

In Figure 4.22 the estimated main effects and two-factor interactions from the 2^{4-1}_{IV} fractional factorial design are presented for each evaluated variation metric in the Block configuration. Although θ_y was initially assumed to have a small influence, it exhibited the strongest main effect throughout all responses. Fortunately, as a result of changing magnitude of stiffness in the soil and not the variability in stiffness, the main effect of ctc_z (C) was either low or negligible in all responses. De-aliasing of some two-factor interactions is therefore possible following Derivation 4.1 since all interactions consisting of D can be considered negligible.

$$\begin{aligned} \mathrm{AB} &= \mathrm{CD} \rightarrow \mathrm{AB} \\ \mathrm{AC} &= \mathrm{BD} \rightarrow \mathrm{BD} \\ \mathrm{AD} &= \mathrm{BC} \rightarrow \mathrm{AD} \end{aligned} \tag{4.1}$$

In Figure 4.20a, the CV of the accumulated settlement along the track is primarily governed by θ_y (D). A shift in θ_y from 1.5 m to 2.5 causes a large average reduction in CV which is coherent with the findings within the same range in Section 4.3.2 for substructure stiffness (see Figure 4.18a). However, it is not consistent with the results reported in Section 4.2.1 where larger θ_y was synonymous with higher variation in settlement. In contrast, a shift in low level to high level $\theta_{x,z}$ (A) inflicts an increase in the CV which is consistent with the observations in previous sections. The second largest main effect, CV_{LCC} (B), in Figure 4.20a is positive since it expands the range of elasticity moduli in the soil, thus increasing the variation in settlements.

The effects of each factor on the estimated wavelength in accumulated settlement along the track are presented in Figure 4.20b. CV_{LCC} (B) and ctc_z (C) exhibit no influence on the estimated wavelength, while a level change in $\theta_{x,z}$ (A) over the range studied extends the wavelength by 7 m, secondary to a level change in θ_y (D) which shortens the wavelength by about 23 m. Given the estimated wavelengths of each run displayed in the table of Figure 4.19, changes in θ_y are associated with a shift in periodicity where wavelengths generally occur either below 15 m or above 35 m. A similar response for θ_y was observed in Section 4.3.2, Figure 4.18b, where wavelengths in substructure stiffness clustered around either 15 m or 35 m. In contrast, changes in $\theta_{x,z}$ within the studied parameter range instead induce a smaller shift in settlement wavelength, with estimates remaining clustered above 35 m. In Section 4.3.2, Figure 4.16b, $\theta_{x,z}$ exhibits a similar response where wavelengths of substructure stiffness are clustered around lengths of 35 m.

The normalised mean squared successive difference in Figure 4.20c measures how much each consecutive pair of sleepers differs in permanent settlements compared to the total variation. The main effect exhibited by θ_y (D) is most likely due to a large change in variance implicated by the large effect it has on CV. The difference between the effects of $\theta_{x,z}$ (A) and CV_{LCC} (B) on MSSD/s^2 compared to CV is also in the same order of magnitude, indicating that the effects on MSSD/s^2 are primarily a measurement of the effects on the variance. In fact, ctc_z (C) had the highest main effect when when calculating the effects on non-normalised mean squared successive difference by the parameters investigated.

In Figures 4.20a–4.20c the two-factor interaction effects are presented for each response metric and investigated parameter. Overall, the interaction effects are considerably lower than the corresponding main effects, indicating that two-factor interactions are negligible within the studied parameter ranges.

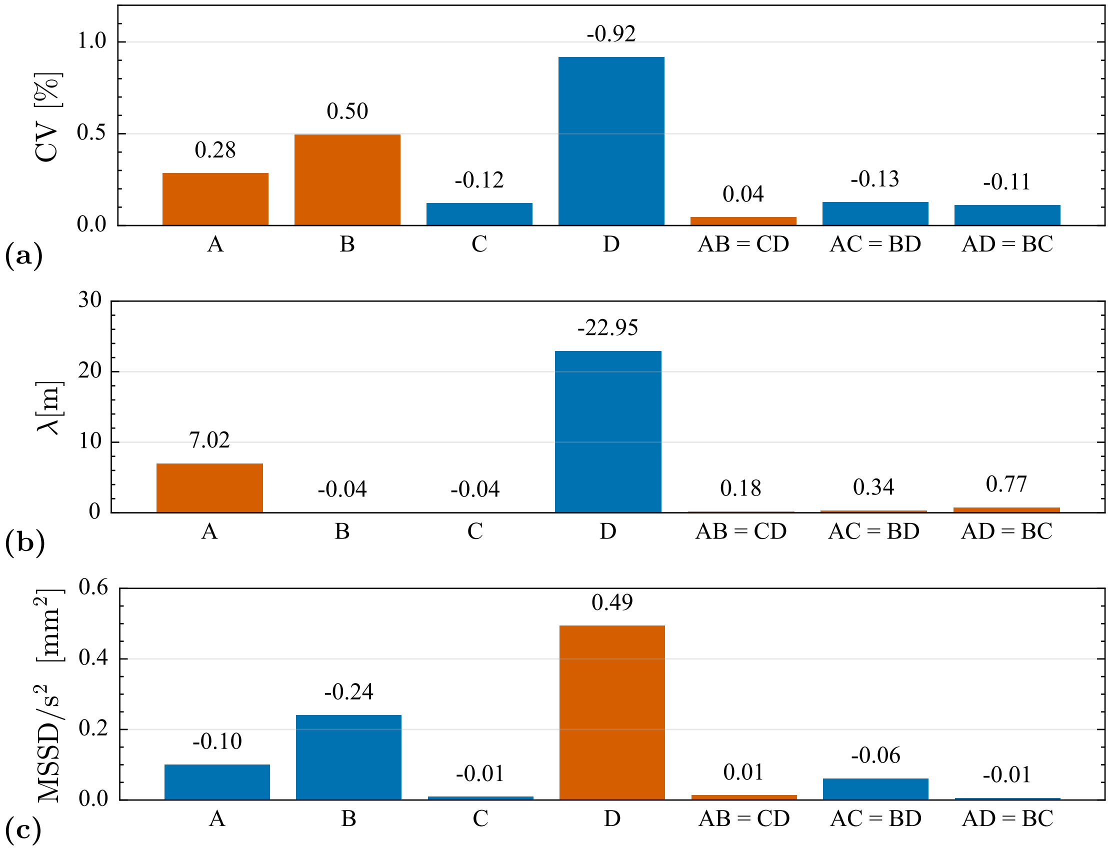

Figure 4.20: Estimated effects on variation metrics for accumulated long-term settlement by LC-parameters in the Block configuration **(a)** Effects on CV **(b)** Effects on λ **(c)** Effects on MSSD/s^2

The accumulated long-term settlement of each sleeper and run configuration with the Wall configuration is shown in Figure 4.21 together with a summary table of the variation metrics obtained for each run. The fitted curve semivariograms used to estimate the wavelengths of the settlement distributions are located in Appendix D.2. For run 2 and run 8 it was not possible to determine a wavelength of settlements due to high dispersion in semivariance between sequential lag distances. The wavelength of these two runs was assigned as 0.6 m, equivalent to the adopted sleeper spacing.

In Figure 4.21, the graph show some resemblance to Figure 4.19 where there is clear distinction between runs employing the high and low level of ctc_z. In the Wall configuration it is not just a clear difference in settlement magnitude but also in the variation along the track. With the larger ctc_z assigned in every even run number, the permanent settlement fluctuates a considerable amount locally while with the low value of ctc_z assigned in every odd run number, the settlement fluctuates less rapidly.

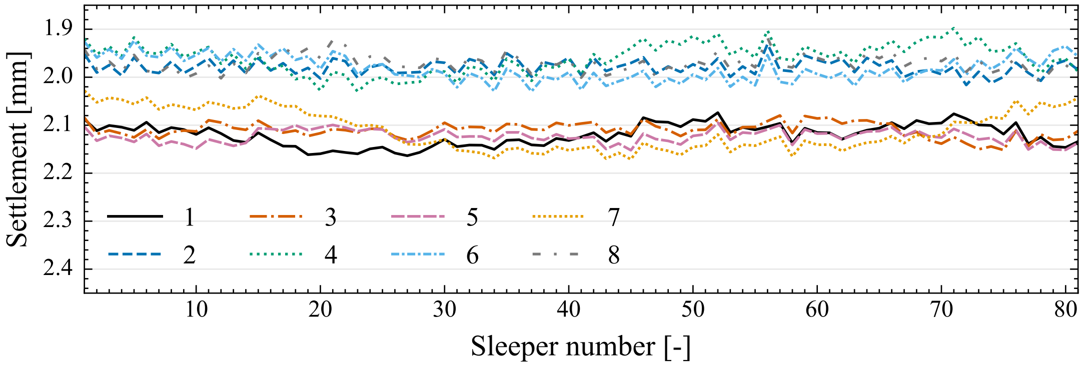

	1	2	3	4	5	6	7	8
CV [%]	1.07	0.81	0.75	1.60	0.66	1.36	2.00	0.96
λ [m]	36.43	0.6*	13.76	36.90	20.89	42.29	42.45	0.6*
MSSD/s^2 [mm^2]	0.44	2.40	0.91	0.64	1.20	0.85	0.13	1.75

Figure 4.21: Accumulated long-term settlement and metrics for its variation from the 2^{4-1}_{IV} factorial with the Wall configuration. *Not possible to determine wavelength through with semivariance.

In Figure 4.22 the estimated main effects and two-factor interactions from the 2^{4-1}_{IV} fractional factorial design are presented for each evaluated variation metric in the Wall configuration. At least one main effect in every response is negligible. For CV, ctc$_z$ (C) is negligible, while CV$_{LCC}$ (B) and $\theta_{x,z}$ (A) are negligible for λ and MSSD/s^2 respectively. De-aliasing is therefore possible following Derivation 4.2.

$$\begin{array}{c|c|c}
\text{CV} & \lambda & \text{MSSD/s}^2 \\
\text{AB} = \text{CD} \rightarrow \text{AB} & \text{AB} = \text{CD} \rightarrow \text{CD} & \text{AB} = \text{CD} \rightarrow \text{CD} \\
\text{AC} = \text{BD} \rightarrow \text{BD} & \text{AC} = \text{BD} \rightarrow \text{AC} & \text{AC} = \text{BD} \rightarrow \text{BD} \\
\text{AD} = \text{BC} \rightarrow \text{AD} & \text{AD} = \text{BC} \rightarrow \text{AD} & \text{AD} = \text{BC} \rightarrow \text{BC}
\end{array} \tag{4.2}$$

Each main effect of each investigated parameter on the CV of permanent settlement along the track with the Wall configuration is presented in Figure 4.22a. The order and significance of effects are approximately identical to the corresponding estimated effects with the Block configuration (see Figure 4.20a). Interestingly, the low effect ctc$_z$ (C) suggests that a geometrical change in the longitudinal spacing between homogenised reinforcement volumes does not affect relative variability in settlements along the track. It does however affect how much the settlements varies with each successive sleeper supported by the main effect of ctc$_z$ on MSSD/s^2, presented in Figure 4.22c. Unlike the other main effects on MSSD/s^2, the effect of ctc$_z$ is not governed by the variance and can therefore be interpreted as having a large effect on how much settlements varies from sleeper to sleeper compared to the total variation. This is coherent with the previous interpretation of Figure 4.21 where runs with a longitudinal reinforcement volume spacing of 2.04 exhibits more local fluctuations in permanent settlement compared to runs where the spacing was 1.36 m. The main effects of the other parameters on CV and MSSD/s^2 follow similar tendencies as in the analyses with the Block configuration.

In Figure 4.22b, the estimated main effects of each parameter on approximated permanent settlement wavelengths are presented. The estimated wavelengths were similar in size compared to the Block configuration with exception of run 2 and run 8 (see table in Figure 4.21). Comparable to the Block configuration, CV_{LCC} (B) exhibit no influence on the estimated wavelength. A level change in θ_y (D) over its investigated range shortens the wavelength by about 31 m following the behaviour comparable to the Block configuration where a level change from 1.5 m to 2.5 m for θ_y is affiliated with a clear reduction in the estimated wavelength of the permanent settlements. The second largest effect on the estimated wavelengths was by ctc_z (C) indicating that the spacing between reinforcement volumes in the applied range is of importance. Compared to the Block configuration, a change in $\theta_{x,z}$ (A) in the Wall configuration results in a smaller extension in settlement wavelength. The interpretation of the influence on the wavelength these three parameters have is of some ambiguity since they are highly circumstantial. All analyses are performed with the same random field seed which dictates what value of elasticity modulus gets assigned to what global coordinates. To properly ascertain the behaviour of the influence every parameter has on the estimated wavelength would require replicating the factorial design with multiple random field realisations.

In Figures 4.22a–4.22c the two-factor interaction effects are also presented for each response metric and investigated parameter. Except for AB = CD in Figure 4.22b, the two-factor interaction effects are in general substantially lower than the corresponding non-negligible main effects within the parameter scope investigated. According to Derivation 4.2, the alias pair AB = CD is more likely to be the interaction between ctc_z (C) and θ_y (D). The negative effect of this interaction suggests that the combined effect of assigning the high level of ctc_z and θ_y simultaneously amplifies the reduction in wavelength. Indeed, the runs where these two factors where assigned their high level was run 2 and run 8 where it was not possible to determine a wavelength in the permanent settlement. Within the estimated parameter ranges, ctc_z and θ_y can in combination introduce a lack of spatial correlation along the track.

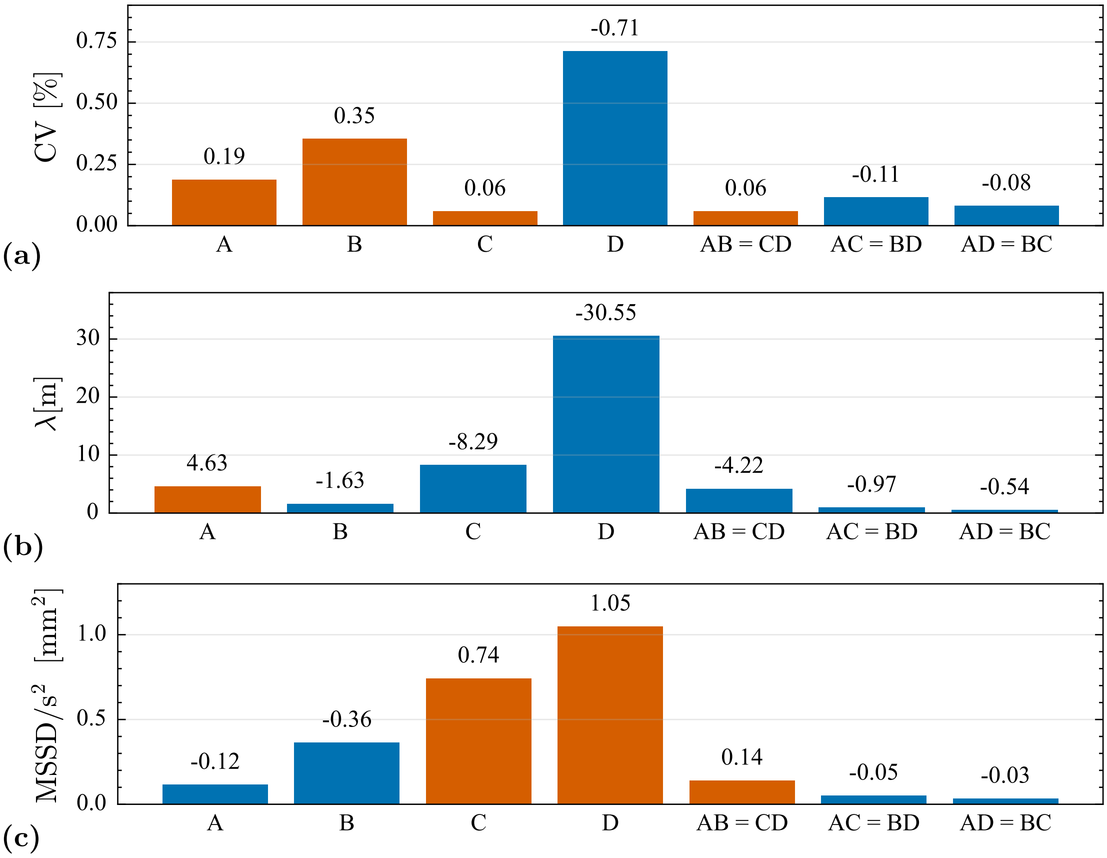

Figure 4.22: Estimated effects on variation metrics for accumulated long-term settlement by LC-parameters in the Wall configuration **(a)** Effects on CV **(b)** Effects on λ **(c)** Effects on MSSD/s^2

5 Summary and conclusion

The dynamic vehicle-track-soil interaction and long-term settlement behaviour of ballasted railway tracks constructed on stabilised soft clay was investigated. The focus was on characterising the influence of the heterogeneity in lime-cement columns (LCCs) via spatial variability in stiffness. The modelling approach coupled a substructure 3D finite-element model used for short-term simulation with a 2D model integrated with two empirical settlement models for the long-term settlement calculations. The first empirical settlement model was a visco-plastic threshold model for the ballast/sub-ballast settlement contribution, and the other was for the settlement in the subgrade. A stochastic random field modelling approach was combined with a sensitivity analysis to assess the influence of spatial variability in the stiffness and geometry of lime-cement columns on the track stiffness and accumulated settlements.

A 3D substructure model including an embankment and a 15 m thick soft clay layer is modelled using the Finite-Element Method in the STEM open source code. The 3D model is coupled with a multi-body dynamics simulation in which a bogie travels from one side of the domain to the other. The stress and strain in different layers are calculated and compared for various cases with and without reinforcement. Furthermore, the equivalent stiffness at the interface between the sleeper and the ballast layer is calculated and used as input to the 2D model to compute the long-term track alignment. The LCCs are modelled using different averaging approaches: individual columns, referred to as Columns; a large block, referred to as Block; and walls transverse to the track and discretised along the track, referred to as Wall.

Results from the reinforced configurations demonstrate greater equivalent substructure stiffness compared to the unreinforced configuration, generating significantly less short-term and long-term permanent deformation. Compared to the reference case without ground improvement, the short-term deformations reduced ca. 2 mm, whereas in the long-term, after 1 year, the reduction was around 1 mm. The reinforced configurations also exhibit a shift in the frequency and magnitude of the peak track receptance. Although the ground improvement reduces the deformations, they simultaneously generate larger sleeper-ballast contact forces during vehicle passages compared to the reference case. Stiffer support conditions result in a narrower load transfer to the ballast layer, hence the load is distributed over fewer sleepers resulting in larger contact forces. Larger contact forces mean that within each analysis, sleepers supported by a stiffer substructure exhibit larger permanent settlements from cyclic loading compared to those with softer substructure support.

The short-term responses of the reinforcement scenarios Block and Wall indicate that homogenised modelling approaches are capable of reproducing the overall behaviour of individually modelled square columns (that represent cylindrical columns in a more computationally efficient manner). The short-term displacement of sleepers in the Block and Wall configurations deviate from the Columns configuration within tenths of millimeters, with the Wall configuration more closely adhering to the response of individual columns. This behaviour is also prevalent in the vertical strain distribution where Block and Wall produced magnitudes of strain comparable to that of individual columns. However, the strain distribution with depth of the Columns configuration is better replicated by the Wall configuration. Overall, the Block and Wall configuration produces similar magnitudes and distributions of deformation, stress and strain while reducing the computational cost due to larger element sizes. This suggests that representing LCC reinforcement as volumes with homogenised material is a viable option in simulations where computational efficiency is important. Long-term simulations employing the Columns configuration was not performed, but the Wall and Block configuration exhibited similar permanent deformation contributions from the ballast/sub-ballast but differed moderately in the subgrade deformation. This is attributed to the Li-Selig model used for the subgrade contribution, which in this study due to the input parameters employed, did not entirely emulate the intricacies of the Wall configuration geometry.

Spatial variability in LCC stiffness causes significant variations in equivalent track stiffness, consequently contributing to variations in permanent settlements along the track under repeated train loading. Variations in substructure stiffness and settlements along the track are proportional in the Block and Wall configurations. Within the investigated parameter ranges, larger horizontal scales of fluctuation ($\theta_{x,z}$) in the stiffness of lime cement columns produces greater spatial variations in substructure stiffness and accumulated settlements with some spatial correlation. $\theta_{x,z}$ in general extends the estimated wavelength of the track irregularity but with clustering of wavelengths approximately 35 m in length. $\theta_{x,z}$ also increases the coefficient of variation (CV) of substructure stiffness and settlements along the track. The vertical scale of fluctuation (θ_y) in LCC stiffness on the other hand induces more complex and less predictable behaviour in the metrics used for variation. In the analyses of different assigned θ_y, variation and spatial correlation in substructure stiffness along the track fluctuates, in contrast to the corresponding analyses investigating $\theta_{x,z}$. A level change in the investigated range of θ_y in the fractional factorial design causes a great reduction in the CV of settlements as well as impacts the estimated wavelength dramatically by clustering wavelengths around 15 m or 35 m in length. The longitudinal centre-to-centre spacing of LCCs (ctc_z)in the Wall configuration also influences the variation of permanent settlements along the track. A larger spacing caused greater local settlement fluctuations with higher dispersion in semivariance but with no impact on the coefficient of variance. Furthermore, longitudinal LCC spacing in combination with θ_y in the Wall configuration, eliminates any spatial correlation in settlements along the track.

Overall, ground improvement with lime-cement columns improves the performance of the railway system by reducing settlements from cyclic loading and increasing the stiffness of the substructure. However, the results demonstrate the importance of accounting for spatial variability in the properties of the ground improvement when evaluating both short- and long-term performance of railway embankments constructed on soft ground.

6 Discussion and future work

The long-term settlement predictions in this study are based on two empirical settlement formulations for cyclic loading, the visco-plastic threshold model and the Li-Selig model. Both models have important limitations and do not incorporate settlements in the soft soils from the dissipation of excess pore water pressures. Although the accumulated settlements reduced when ground improvement was incorporated, the sleeper-ballast contact forces also increased in magnitude. The latter may cause additional ballast degradation from particle breakage and and irreversible deformation in the grain assembly of the ballast. These mechanisms are not explicitly captured in the visco-plastic threshold model. Future work to capture these effects could therefore include more detailed models that include the effects of ballast degradation, e.g. using a DEM-FEM coupled approach. In addition to the ballast deformations, the Li-Selig model is a simplified formulation based on empirical relationships and sleeper-ballast contact forces. The empirical values were assumed for each layer and constitutes an important limitation as no specific values could be validated. Furthermore, the contact forces are heavily influenced by the accumulation and compaction of the ballast layer, which is not fully captured with the Li-Selig model, as the evolution of stresses and stiffness are not continuously updated. Calibration against field measurements or laboratory experiments is therefore necessary to improve the reliability of long-term settlement predictions, and future research should focus on the development of more advanced settlement frameworks.

Linear elastic material models and single phase were exclusively considered to reduce computational complexity while at the same time providing reasonable estimations of the dynamic track response. However, these modelling assumptions limit the ability to capture the rate-dependent and hydromechanically coupled response of natural soils. Consequently, implementation of constitutive models that can capture these behaviours is recommended for future studies to improve the understanding of the response of natural and stabilised soft clays under repeated train loading.

The stochastic modelling approach adopted utilised random field realisations using the same random field seed. Although this enabled direct comparisons between the analysed scenarios, the use of a single seed limits the statistical representativeness of the obtained results. To improve the reliability of the analyses, future studies should extend the simulations to include random field realisations using multiple random seeds. The track length of the model could also be increased to make the statistical analyses more rigorous. Similarly, the ranges chosen for the fractional factorial design limit the statistical representation to that particular interval. Consequently, the results may exhibit different behaviour, would larger ranges be applied. It is recommended to further study this by implementing ranges based on measured or experimental data.

In this study, the stabilised clay was modelled using columns with a fixed length of 10 m with constant geometry and grid pattern. However, modelling columns with different lengths or grid patterns could provide useful information on load redistribution, stiffness responses, and the effects of local variation. Additionally, only floating column configurations were considered. Therefore, future research could investigate how different resistance mechanisms affect the response from dynamic train loads.

Bibliography

Abadi, T., Le Pen, L., Zervos, A., & Powrie, W. (2016). A Review and Evaluation of Ballast Settlement Models using Results from the Southampton Railway Testing Facility (SRTF). *Procedia Engineering*, *143*, 999–1006. https://doi.org/10.1016/J.PROENG.2016.06.089

Abetong AB. (2023). *Slipers A28 (Environmental Product Declaration #NEPD-4139-3376-SE)* (tech. rep.). https://www.epd-global.com/getfile.php/13171932-1741643100/EPDer/Byggevarer/Betongvarer/NEPD-4139-3376_Slipers-A28.pdf

Aggestam, E., & Nielsen, J. C. (2019). Multi-objective optimisation of transition zones between slab track and ballasted track using a genetic algorithm. *Journal of Sound and Vibration*, *446*, 91–112. https://doi.org/10.1016/J.JSV.2019.01.027

Ahmadi, A., Nasrollahi, K., Nielsen, J. C., & Dijkstra, J. (2026). Dynamic vehicle–track interaction and differential settlement in a transition zone on railway ballast—An integrated 3D discrete–continuum model. *Computers and Geotechnics*, *190*, 107737. https://doi.org/10.1016/J.COMPGEO.2025.107737

Bachmaier, M., & Backes, M. (2011). Variogram or Semivariogram? Variance or Semivariance? Allan Variance or Introducing a New Term? *Mathematical Geosciences*, *43*(6), 735–740. https://doi.org/10.1007/s11004-011-9348-3

Bergström, U., Pile, O., Curtis, P., & Eliasson, T. (2022, February). *Göteborgsområdets berggrund, jordarter och geologiska utveckling* (tech. rep.). Sveriges Geologiska Undersökning.

Box, G. E. P., Hunter, J. S., & Hunter, W. G. (2005). *Statistics for experimenters : design, innovation, and discovery* (2nd ed.). Wiley-Interscience.

Bozkurt, S., Abed, A., & Karstunen, M. (2023). Finite element analysis for a deep excavation in soft clay supported by lime-cement columns. *Computers and Geotechnics*, *162*, 105687. https://doi.org/10.1016/J.COMPGEO.2023.105687

Bozkurt, S., Dijkstra, J., & Karstunen, M. (2025). Influential factors on the performance of embankments stabilised on deep-mixed columns. *Transportation Geotechnics*, *55*. https://doi.org/10.1016/J.TRGEO.2025.101643

Esveld, C. (2014). *Modern Railway Track* (3.4). MRT-Productions.

European Committee for Standardization. (2005, April). *Execution of special geotechnical works - Deep mixing (SS-EN 14679:2005)* (tech. rep.). Swedish Standards Institute (SIS). Stockholm.

European Committee for Standardization (CEN). (2017, June). *Railway applications-Track-Rail-Part 1: Vignole railway rails 46 kg/m and above (SS-EN 13674-1:2011+A1:2017)* (tech. rep.). Swedish Standards Institute (SIS). Stockholm.

Fenton, G. A., & Griffiths, D. V. (2008, August). *Risk Assessment in Geotechnical Engineering*. Wiley. https://doi.org/10.1002/9780470284704

Gatti, P. L. (2014, February). *Applied Structural and Mechanical Vibrations* (2nd ed.). CRC Press. https://doi.org/10.1201/b16697

Griffiths, D. V., & Fenton, G. A. (2007). *Probabilistic methods in geotechnical engineering*. Springer.

Hofres. (2008, April). X 2000-tåg vid Lunds centralstation. https://commons.wikimedia.org/wiki/File:X2000,_Lund_C.JPG

Holm, G., Andréasson, B., Bengtsson, P.-E., Bodare, A., & Eriksson, H. (2002, August). *Mitigation of Track and Ground Vibrations by High Speed Trains at Ledsgård, Sweden* (tech. rep.). Swedish Deep Stabilization Research Centre. Linköping.

Hristopulos, D. T. (2020). *Random fields for spatial data modeling : a primer for scientists and engineers*. Springer. https://doi.org/10.1007/978-94-024-1918-4

Iwnick, S. (1998). Manchester Benchmarks for Rail Vehicle Simulation. *Vehicle System Dynamics*, *30*(3-4), 295–313. https://doi.org/10.1080/00423119808969454

Jonefjäll, A., & Sabattini, M. (2022, December). *Transversalbelastning av pålar i postglacial lera* (tech. rep.). Göteborg.

Karlsson, M., & Moritz, L. (2016, February). *Trafikverkets tekniska krav för geokonstruktioner - TK Geo 13* (tech. rep.).

Knappert, J., & Craig, R. (2012). *Craig's Soil Mechanics* (8th ed.). Spoon Press.

Lamprea-Pineda, A. C., Connolly, D. P., & Hussein, M. F. (2022). Beams on elastic foundations – A review of railway applications and solutions. *Transportation Geotechnics*, *33*. https://doi.org/10.1016/j.trgeo.2021.100696

Larsson, R. (2006). *Djupstabilisering med bindemedels- stabiliserade pelare och masstabilisering – En vägledning* (tech. rep.). Svensk Djupstabilisering. Linköping.

Larsson, S., & Nilsson, L. (2005). Findings of the work on influencing factors on the installation process for lime-cement columns. *Proceedings of the international conference on deep mixing - best practice and recent advances: Deep mixing'05*, 561–570.

Larsson, S., Stille, H., & Olsson, L. (2005). On horizontal variability in lime-cement columns in deep mixing. *Géotechnique*, *55*(1), 33–44. https://doi.org/10.1680/geot.2005.55.1.33

Li, D., & Selig, E. T. (1996). Cumulative Plastic Deformation for Fine-Grained Subgrade Soils. *Journal of Geotechnical Engineering*, *122*(12), 1006–1013. https://doi.org/10.1061/(ASCE)0733-9410(1996)122:12(1006)

Montgomery, D. C. (2013). *Design and analysis of experiments*. John Wiley & Sons, Inc.

Nasrollahi, K., & Nielsen, J. C. O. (2024). Influence of sleeper base area and spacing on long-term differential settlement in a railway track transition zone. *Proceedings of the Sixth International Conference on Railway Technology: Research, Development and Maintenance*, *7*, 1–12.

Nasrollahi, K. (2025). *Transition zone design for reduced track settlements – field measurements and numerical simulations* [PhD thesis]. Chalmers University of Technology.

Nasrollahi, K., Dijkstra, J., & Nielsen, J. C. (2024). Towards real-time condition monitoring of a transition zone in a railway structure using fibre Bragg grating sensors. *Transportation Geotechnics*, *44*. https://doi.org/10.1016/J.TRGEO.2023.101166

Nasrollahi, K., Nielsen, J. C., Aggestam, E., Dijkstra, J., & Ekh, M. (2023). Prediction of long-term differential track settlement in a transition zone using an iterative approach. *Engineering Structures*, *283*, 115830. https://doi.org/10.1016/J.ENGSTRUCT.2023.115830

Nasrollahi, K., Nielsen, J. C., & Dijkstra, J. (2026). An enhanced three-dimensional reduced-order track model for predicting differential settlement in railway transition zones on stratified soils. *Transportation Geotechnics*, *61*, 102040. https://doi.org/https://doi.org/10.1016/j.trgeo.2026.102040

Nasrollahi, K., Ramos, A., Nielsen, J. C., Dijkstra, J., & Ekh, M. (2024). Benchmark of calibrated 2D and 3D track models for simulation of differential settlement in a transition zone using field measurement data. *Engineering Structures*, *316*(June), 118555. https://doi.org/10.1016/j.engstruct.2024.118555

Nielsen, J. C., & Li, X. (2018). Railway track geometry degradation due to differential settlement of ballast/subgrade – Numerical prediction by an iterative procedure. *Journal of Sound and Vibration*, *412*, 441–456. https://doi.org/10.1016/j.jsv.2017.10.005

Nishiura, D., Sakai, H., Aikawa, A., Tsuzuki, S., & Sakaguchi, H. (2018). Novel discrete element modeling coupled with finite element method for investigating ballasted railway track dynamics. *Computers and Geotechnics*, *96*, 40–54. https://doi.org/10.1016/j.compgeo.2017.10.011

Ouakka, S., Verlinden, O., & Kouroussis, G. (2022). Railway ground vibration and mitigation measures: benchmarking of best practices. *Railway Engineering Science*, *30*(1), 1–22. https://doi.org/10.1007/s40534-021-00264-9

Paixão, A., Varandas, J. N., Fortunato, E., & Calçada, R. (2016). Non-Linear Behaviour of Geomaterials in Railway Tracks under Different Loading Conditions. *Procedia Engineering*, *143*, 1128–1135. https://doi.org/10.1016/j.proeng.2016.06.147

Pyrcz, M. J., & Deutsch, C. V. (2003). The whole story on the hole effect. *Geostatistical Association of Australasia Newsletter*, *18*.

Setiawan, D. M., & Kim, Y.-R. (2025). A review on structural configuration and constitutive material behavior of rail tracks in finite element modeling. *KSCE Journal of Civil Engineering*, *29*(2). https://doi.org/10.1016/j.kscej.2025.100160

Shan, Y., Zhou, S., Wang, B., & Ho, C. L. (2020). Differential Settlement Prediction of Ballasted Tracks in Bridge–Embankment Transition Zones. *Journal of Geotechnical and Geoenvironmental Engineering*, *146*(9). https://doi.org/10.1061/(ASCE)GT.1943-5606.0002307

STEM team. (2026). STEM-Vibrations documentation (Version 1.3). https://stemvibrations.readthedocs.io/v1.3/

StemVibrations. (2026, March). STEM: Numerical model to simulate railway induced vibrations. https://github.com/stemVibrations/STEM

Svensk Byggtjänst. (2020). *RA Anläggning 20*.

Svenska Geotekniska Föreningen. (2000, November). *Kalk- och kalkcementpelare - Vägledning för projektering, utförande och kontroll (Rapport 2:2000)* (tech. rep.). Linköping.

Thompson, D. J., Jiang, J., Toward, M. G., Hussein, M. F., Dijckmans, A., Coulier, P., Degrande, G., & Lombaert, G. (2015). Mitigation of railway-induced vibration by using subgrade stiffening. *Soil Dynamics and Earthquake Engineering*, *79*, 89–103. https://doi.org/10.1016/J.SOILDYN.2015.09.005

Tornborg, J., Karlsson, M., Kullingsjö, A., & Karstunen, M. (2021). Modelling the construction and long-term response of Göta Tunnel. *Computers and Geotechnics*, *134*, 104027. https://doi.org/10.1016/j.compgeo.2021.104027

Trafikanalys. (2024). Bruttotonkilometer av vagnar, miljoner efter år och trafikslag. [Data set]. https://www.trafa.se/bantrafik/bantrafik/?cw=1&q=t06013%7Car%7Cbruttton%7Ctrafik~barchart

Trafikverket. (2012, June). *Betongsliper - Teknisk specifikation rörande Trafikverkets linjesliprar i betong med e-clip befästning, produktgrupp 1. (TRV 2011/60376)* (tech. rep.). TRV Koncern. https://bransch.trafikverket.se/contentassets/c86948a9ace04b32b352c781849d7dc8/a13.pdf

Trafikverket. (2015). *BVS 1585.005 - Typsektioner för banan (TDOK2015:0198)* (tech. rep.).

Trafikverket. (2026, January). Vad är järnvägen gjord av? - www.trafikverksskolan.se. https://www.trafikverksskolan.se/utbildningsomraden/bana/vad-ar-jarnvagen-gjort-av/

Varandas, J. N., Paixão, A., Fortunato, E., Zuada Coelho, B., & Hölscher, P. (2020). Long-term deformation of railway tracks considering train-track interaction and non-linear resilient behaviour of aggregates – a 3D FEM implementation. *Computers and Geotechnics*, *126*. https://doi.org/10.1016/J.COMPGEO.2020.103712

Verruijt, A. (2018). *An introduction to soil mechanics*. Springer. https://doi.org/10.1007/978-3-319-61185-3

Wong, D. Y. C., Sadasivan, V., Isaksson, J., Karlsson, A., & Dijkstra, J. (2024). Trans-scale spatial variability of lime-cement mixed columns. *Construction and Building Materials*, *417*. https://doi.org/10.1016/J.CONBUILDMAT.2024.135394

Wood, T., & Karstunen, M. (2022). Modelling the creep of deep foundations in soft Gothenburg clays. *European Journal of Environmental and Civil Engineering*, *26*(7), 2581–2599. https://doi.org/10.1080/19648189.2017.1344146

Wu, C.-F., & Hamada, M. (2021). *Experiments : planning, analysis, and optimization* (3rd ed.). John Wiley & Sons, Inc.

Zuada Coelho, B., Nuttall, J., Noordam, A., & Dijkstra, J. (2023). The impact of soil variability on uncertainty in predictions of induced vibrations. *Soil Dynamics and Earthquake Engineering*, *169*. https://doi.org/10.1016/J.SOILDYN.2023.107855

Zuada Coelho, B., Varandas, J. N., Hijma, M. P., & Zoeteman, A. (2021). Towards network assessment of permanent railway track deformation. *Transportation Geotechnics*, *29*. https://doi.org/10.1016/J.TRGEO.2021.100578

Appendix A

Random field realisations

A.1 Block configuration — random field realisations

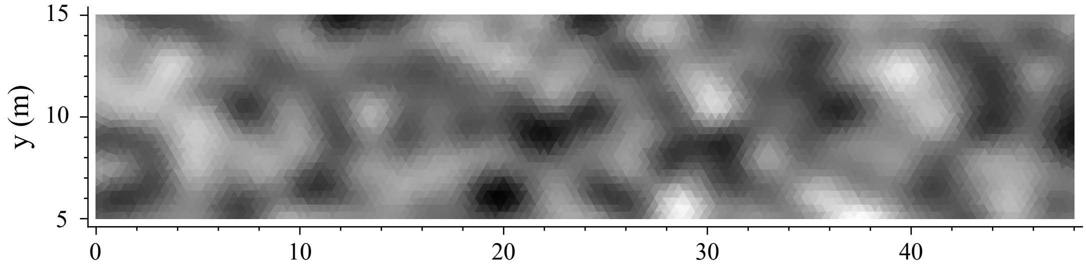

(a) Random field I, average

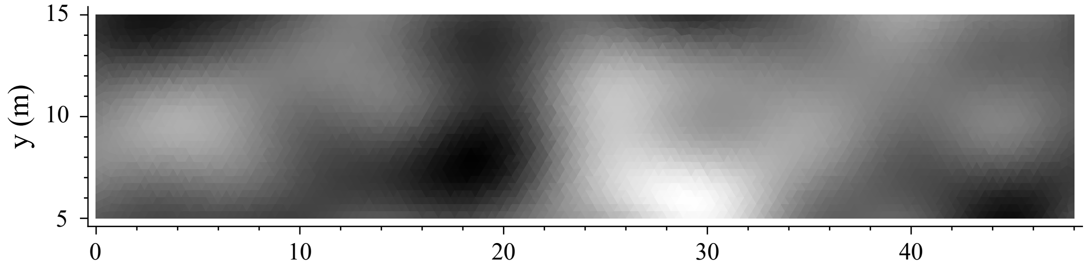

(b) Random field II, max

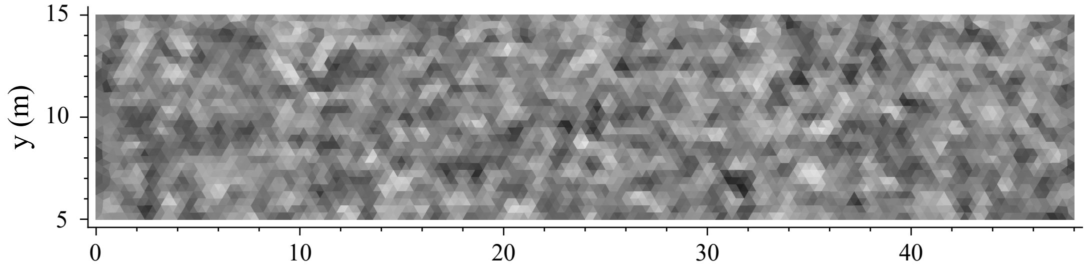

(c) Random field III, min

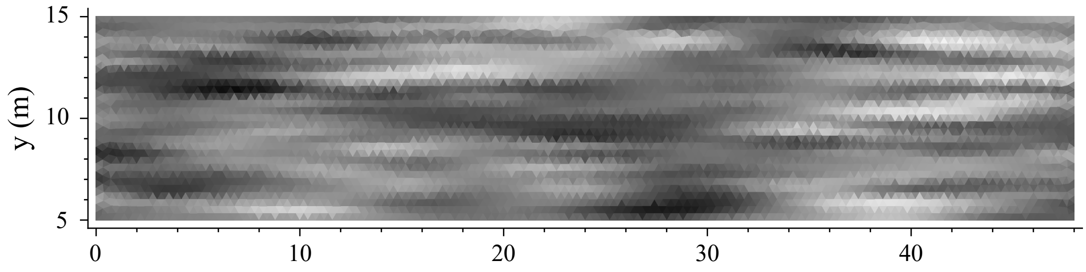

(d) Random field IV, min/max

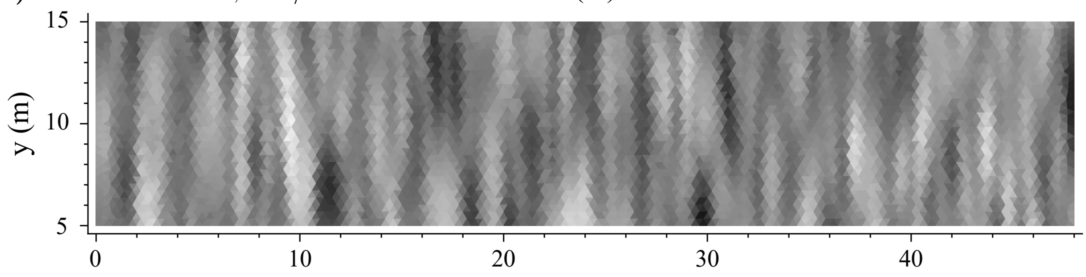

(e) Random field V, max/min

A.2 Wall configuration — random field realisations

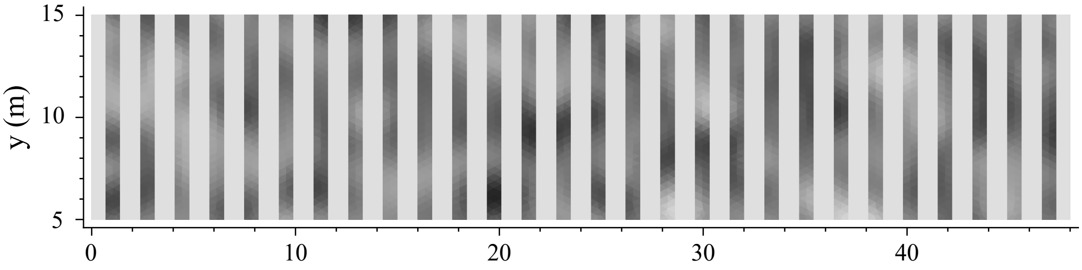

(a) Random field I, average

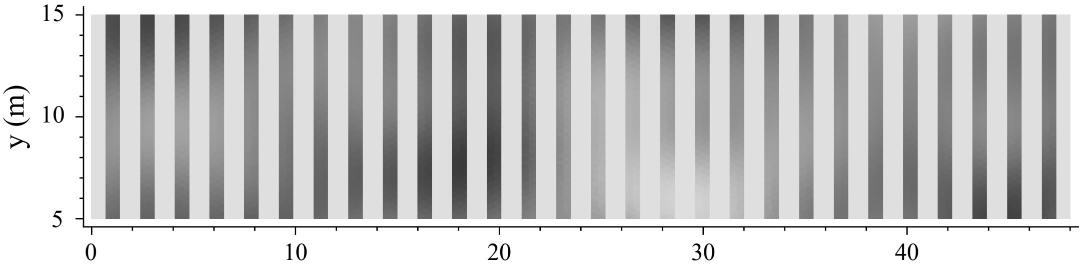

(b) Random field II, max

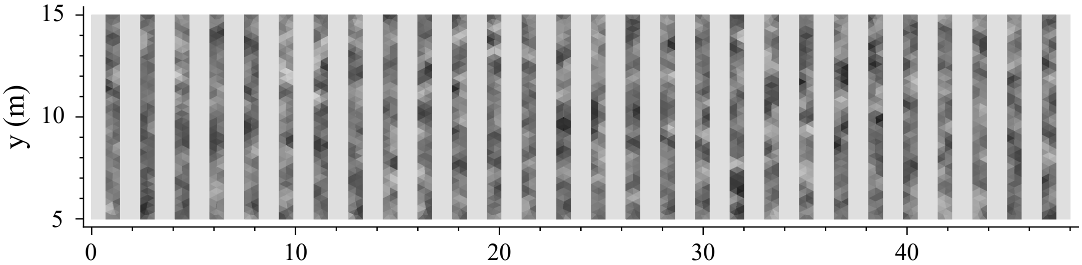

(c) Random field III, min

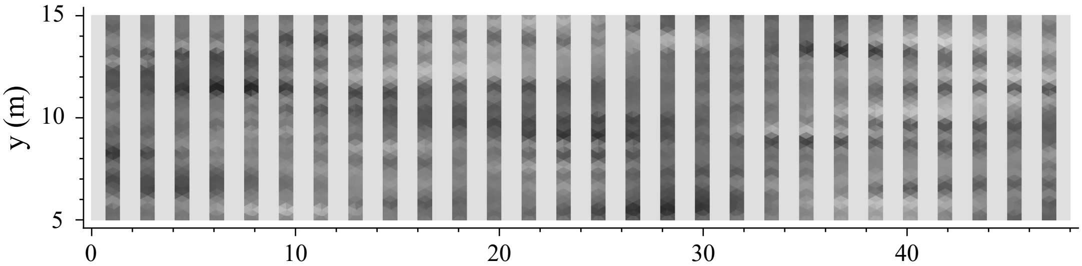

(d) Random field IV, min/max

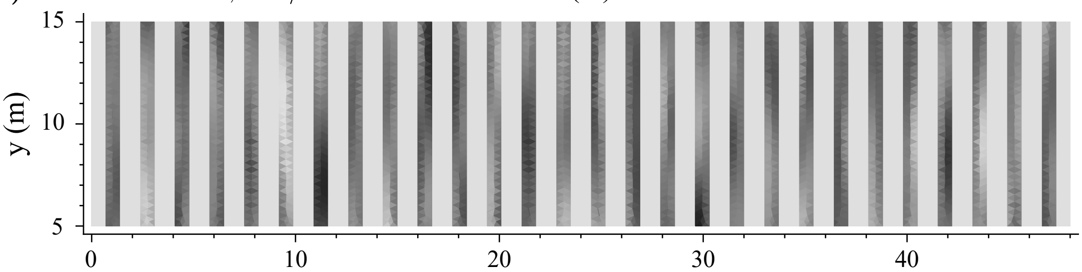

(e) Random field V, max/min

Appendix B

Mesh geometry

B.1 Final mesh design — xy-plane at z = 0

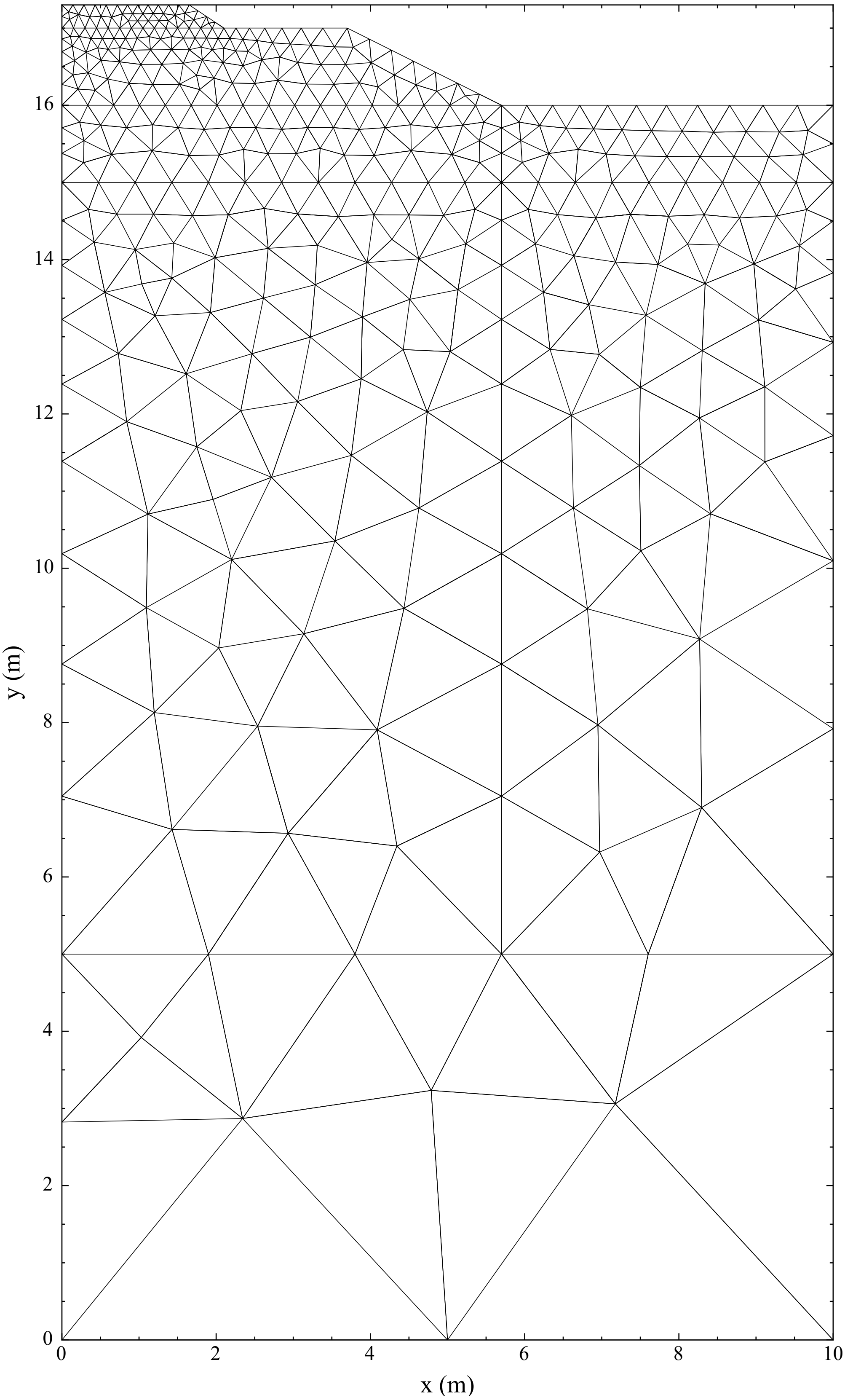

Appendix C

Semivariograms of substructure stiffness — different scales of fluctuation

C.1 Substructure stiffness semi-variograms for different θ_{xz}

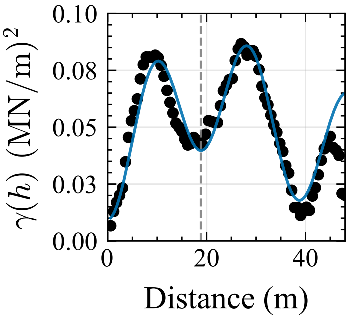

(a) $\theta_{xz} = 0.5$ m

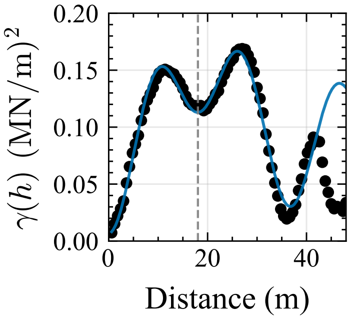

(b) $\theta_{xz} = 1.0$ m

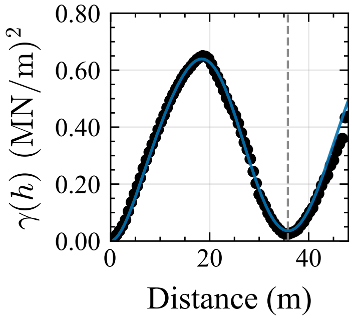

(c) $\theta_{xz} = 1.5$ m

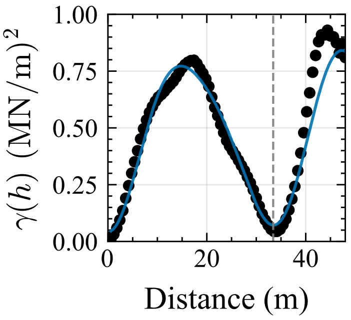

(d) $\theta_{xz} = 2.0$ m

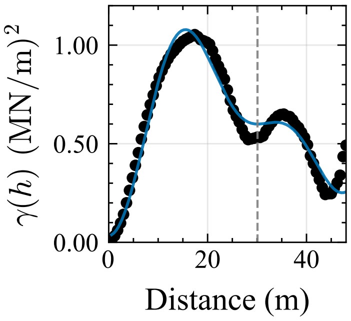

(e) $\theta_{xz} = 2.5$ m

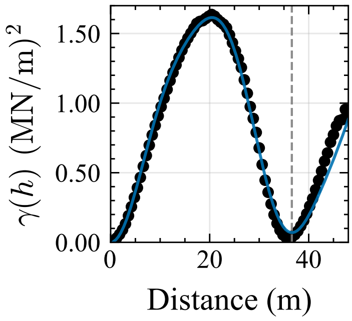

(f) $\theta_{xz} = 3.0$ m

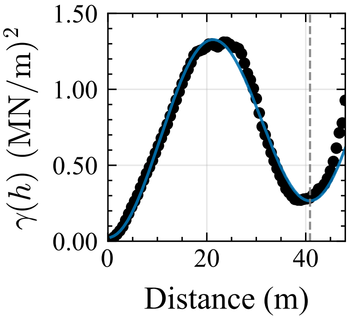

(g) $\theta_{xz} = 4.0$ m

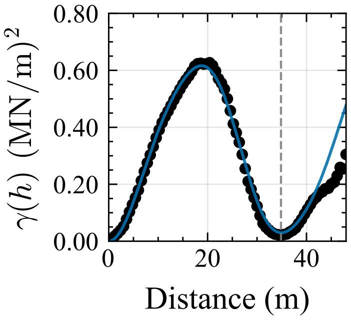

(h) $\theta_{xz} = 5.0$ m

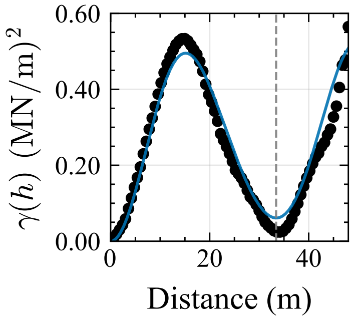

(i) $\theta_{xz} = 6.0$ m

C.2 Substructure stiffness semi-variograms for different θ_y

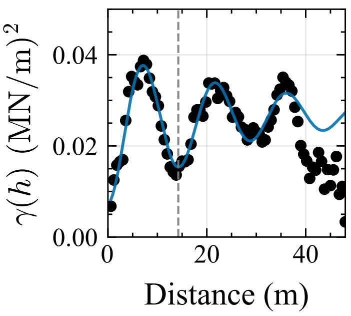

(a) $\theta_y = 0.5$ m

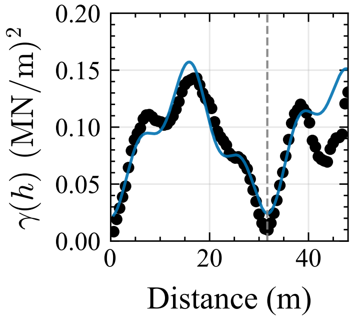

(b) $\theta_y = 1.0$ m

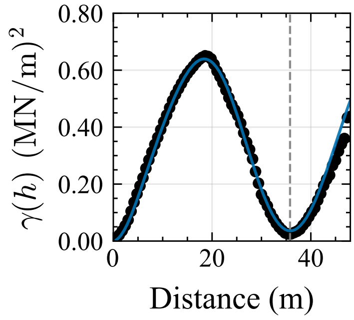

(c) $\theta_y = 1.5$ m

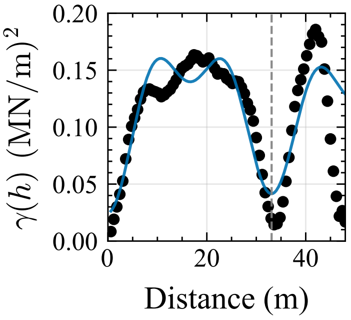

(d) $\theta_y = 2.0$ m

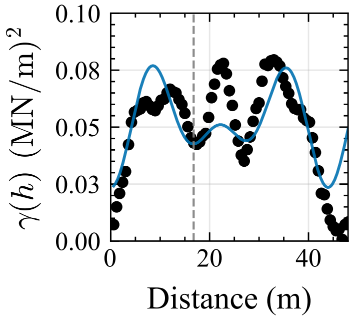

(e) $\theta_y = 2.5$ m

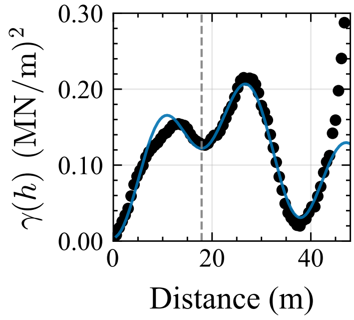

(f) $\theta_y = 3.0$ m

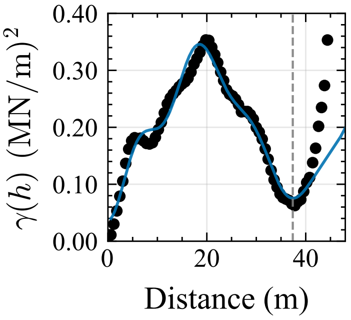

(g) $\theta_y = 4.0$ m

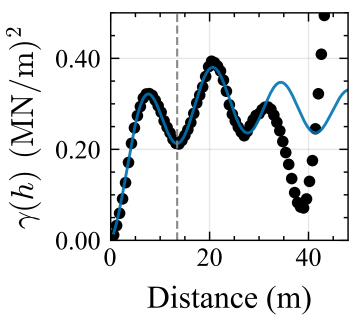

(h) $\theta_y = 5.0$ m

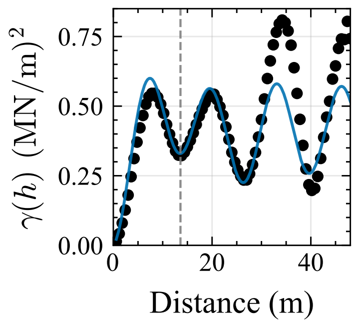

(i) $\theta_y = 6.0$ m

Appendix D

Semivariograms from $2^{4-1}_{\mathbf{IV}}$ factorial

D.1 Block configuration — settlement semivariograms

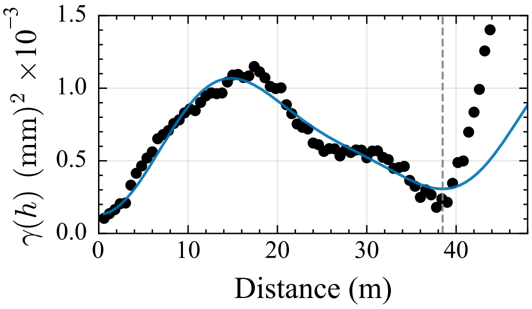

(a) Block, run 1

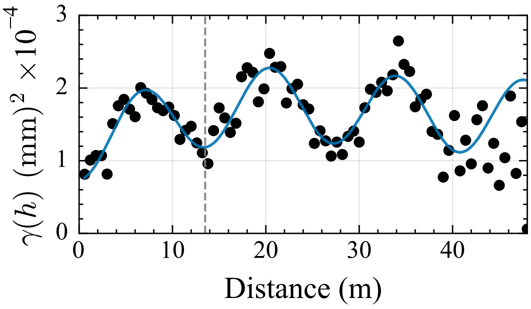

(b) Block, run 2

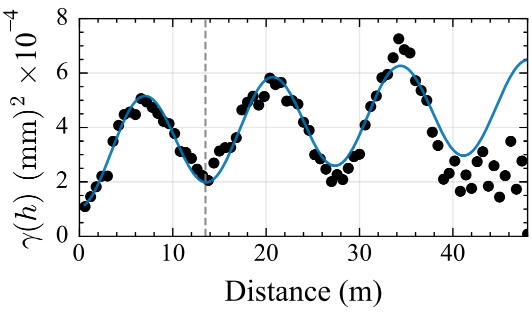

(c) Block, run 3

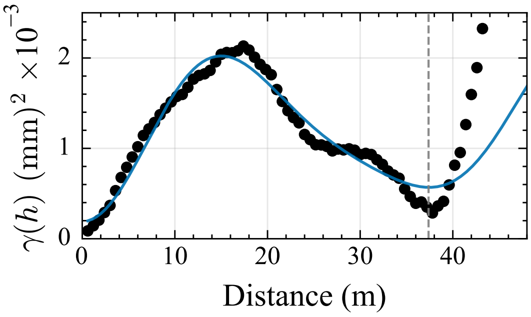

(d) Block, run 4

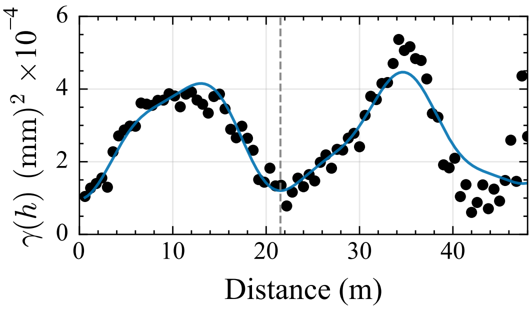

(e) Block, run 5

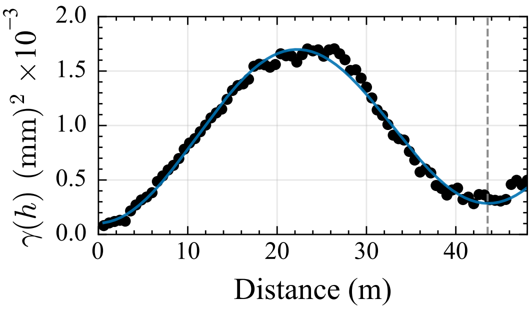

(f) Block, run 6

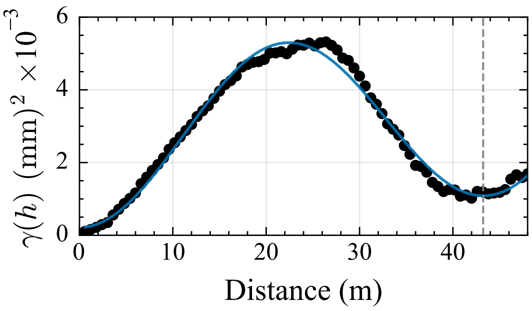

(g) Block, run 7

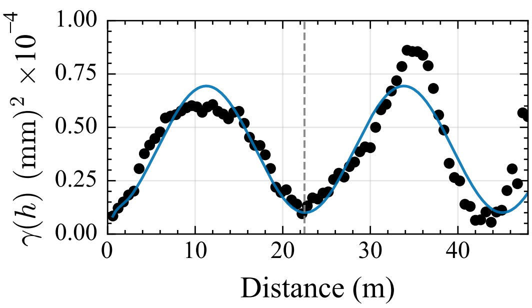

(h) Block, run 8

D.2 Wall configuration — settlement semivariograms

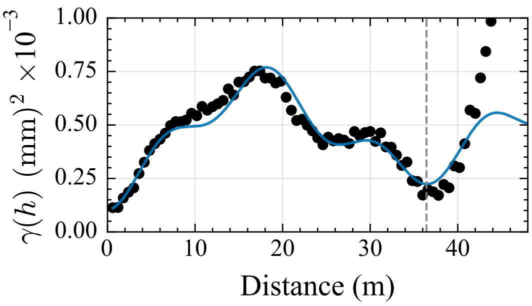

(a) Wall, run 1

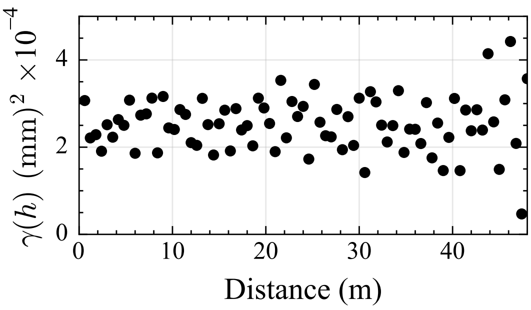

(b) Wall, run 2

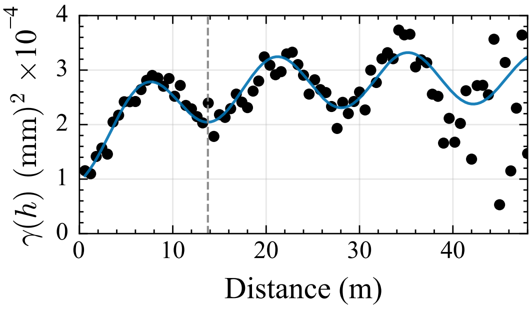

(c) Wall, run 3

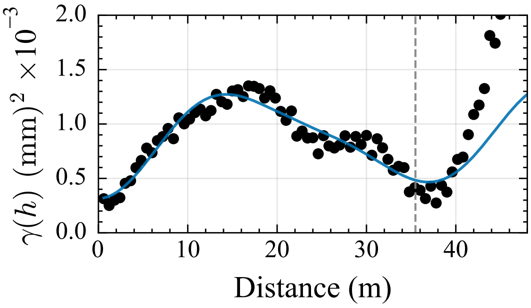

(d) Wall, run 4

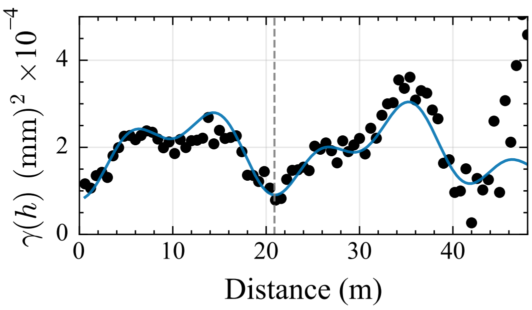

(e) Wall, run 5

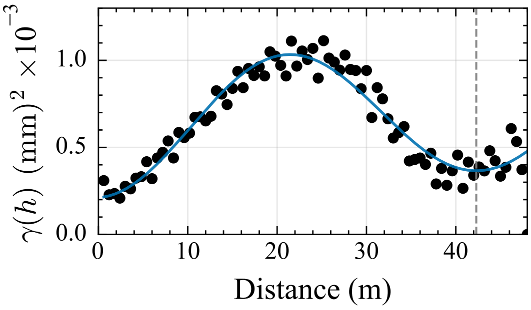

(f) Wall, run 6

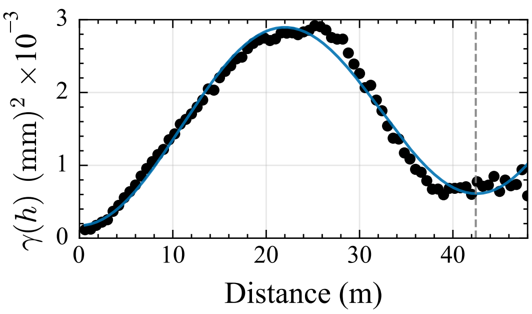

(g) Wall, run 7

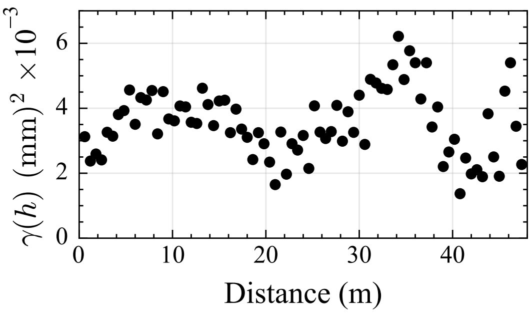

(h) Wall, run 8

DEPARTMENT OF ARCHITECTURE AND CIVIL ENGINEERING
CHALMERS UNIVERSITY OF TECHNOLOGY
Gothenburg, Sweden
www.chalmers.se

CHALMERS
UNIVERSITY OF TECHNOLOGY